MULTIMODAL OPTICAL SPECTROSCOPY AND IMAGING FOR IMPROVING CANCER DETECTION IN THE HEAD AND NECK AT ENDOSCOPY

LIN KAN

NATIONAL UNIVERSITY OF SINGAPORE

2012

MULTIMODAL OPTICAL SPECTROSCOPY AND IMAGING FOR IMPROVING CANCER DETECTION IN THE HEAD AND NECK AT ENDOSCOPY **LIN KAN** **2012**

MULTIMODAL OPTICAL SPECTROSCOPY AND IMAGING FOR IMPROVING CANCER DETECTION IN THE HEAD AND NECK AT ENDOSCOPY

LIN KAN

A THESIS SUBMITTED

FOR THE DEGREE OF DOCTOR OF PHILOSOPHY

DEPARTMENT OF BIOENGINEERING

NATIONAL UNIVERSITY OF SINGAPORE

2012

To my family and friends for their love, support and encouragement

Acknowledgements

The research work presented in this thesis was primarily conducted in Optical Bioimaging Laboratory in the Department of Bioengineering of National University of Singapore during the period from January 2007 to January 2012. In the past 5 years, I met many nice friends in this lab who gave me great encouragement and kind help. Here I would like to thank them sincerely.

First and foremost, I would like to express my sincere appreciation to my supervisor Professor Huang Zhiwei, who offered me the opportunity in the very beginning to pursue the PhD degree in his group. I am indebted to Prof Huang for his technical advice, professional guidance and patience throughout my PhD study. I believe and appreciate that Prof Huang with his insightful view and high standard requirements to the research has an extraordinary impact on my future research career.

I would also express my gratitude to Dr. David Lau from the Department of Otolaryngology, Singapore General Hospital, who offered me invaluable support and great patience in conducting the clinical trials. I would also like to acknowledge my coworkers and team members in Optical Bioimaging Laboratory: Dr Zheng Wei, Dr Yuen Clement, Dr Liu Linbo, Dr Kou Shanshan, Dr Lu Fake, Mo Jianhua, Teh Seng Knoon, Dr Shao Xiaozhuo, Lin Jian, Mads Bergholt**,** Shiyamala Duraipandian, Dr Zhang Qiang and Chen Ling for their kind discussions, suggestions and help on my research work. I also wish to thank my dear parents and all my lovely friends in Singapore, with whom I kept walking through these hard working days.

Last but not least, I also would like to acknowledge the financial support from the Ministry of Education of Singapore, Biomedical Research Council, the National Medical Research Council and the Faculty Research Fund from the National

University of Singapore (NUS) for this research.

LIN Kan

NUS, Singapore 2012

Table of Contents

Abstract

Early diagnosis and localization of head and neck cancers with effective treatment is critical to decreasing the mortality rates. But identification of early cancer can be difficult by using the conventional white-light reflectance (WLR) imaging which heavily relies on visualization of tissue gross morphological changes associated with neoplastic transformation. Optical spectroscopic techniques, such as autofluorescence (AF) spectroscopy and diffuse reflectance (DR) spectroscopy, which provide the information about tissue optical properties, morphologic structures, endogenous fluorophore distribution, blood content and oxygenation, have been comprehensively investigated for *in vitro* or *in vivo* precancer and cancer diagnosis with high diagnostic sensitivity. Raman spectroscopy is an optical vibrational technique capable of providing specific information about biochemical compositions and structures of tissue, which has excelled in the early cancer detection with high diagnostic specificity. This thesis work aims to develop a multimodal optical spectroscopy and imaging technique to complement the WLR imaging for improving cancer diagnosis and characterization at endoscopy.

We have developed an endoscope-based AF/DR spectroscopy and AF/WLR imaging system for cancer detection in the head and neck. The point-wise AF/DR spectra can be acquired in real-time from any specific area of the imaged tissue of interest under the AF/WLR imaging guidance. Spectroscopic measurements of normal (n = 207) and cancerous (n = 239) laryngeal tissue samples from 30 patients were performed to evaluate the diagnostic utility of the combined AF/DR spectroscopy for improving laryngeal cancer diagnosis. The composite AF and DR spectra in the range of 500–660 nm were analyzed using principal component analysis (PCA) and linear

discriminant analysis (LDA), which yielded a diagnostic accuracy of 94.8% (sensitivity of 91.6% and specificity of 98.6%) for cancer detection.

We have also developed a miniaturized fiber-optic Raman endoscopy technique for *in vivo* tissue Raman measurements in the head and neck. We carried out the transnasal image-guided Raman endoscopy for the first time to directly assess distinctive Raman spectral properties of nasopharyngeal and laryngeal tissues *in vivo* during endoscopic examinations. A total of 874 high-quality *in vivo* Raman spectra were successfully acquired from different anatomic locations of the nasopharynx and larynx (i.e., posterior nasopharynx (PN) (n=521), the fossa of Rosenmüller (FOR) (n=157), and true laryngeal vocal chords (LVC) (n=196)) in 23 normal subjects at transnasal endoscopy. The PCA-LDA modeling provides a sensitivity of 77.0% and specificity of 89.2% for differentiation between PN vs. FOR, and sensitivity of 67.3% and specificity of 76.0% for distinguishing LVC vs. PN using leave-one subject out, cross validation. We demonstrated that transnasal image-guided Raman endoscopy can be used to acquire *in vivo* Raman spectra from the nasopharynx and larynx in real-time. Significant Raman spectral differences ($p<0.05$) identified reflecting the distinct composition and morphology in the nasopharynx and larynx should be considered as an important parameter in the interpretation and rendering of diagnostic decision algorithms for *in vivo* tissue diagnosis and characterization in the head and neck.

Further, we also explored the utility of transnasal image-guided high wavenumber (HW) Raman spectroscopy to differentiate tumor from normal laryngeal tissue at endoscopy. A total of 94 HW Raman spectra (22 normal sites, 72 tumor sites) were acquired from 39 patients who underwent laryngoscopic screening. Significant differences in Raman intensities of prominent Raman bands at 2845, 2880 and 2920

cm^{-1} (CH_2 stretching of lipids), and 2940 cm^{-1} (CH_3 stretching of proteins) were observed between normal and cancer laryngeal tissue. PCA-LDA modeling on HW Raman spectra yields a diagnostic sensitivity of 90.3% and specificity of 90.9% for laryngeal cancer identification.

The results of this thesis work suggest that the unique image-guided multimodal (AF/DR/Raman) spectroscopy technique developed has great potential for improving *in vivo* diagnosis and detection of cancer in the head and neck during clinical endoscopic examination.

List of Figures

List of Tables

List of Abbreviations

AF	Autofluorescence
AFI	Autofluorescence imaging
AFS	Autofluorescence spectroscopy
AJCC	American Joint Committee on Cancer
ANN	Artificial neural network
ANOVA	Analysis of variance
AOI	Area of interest
CARS	Coherent anti-stokes Raman scattering
CCD	Charge coupled device
cLSM	Confocal laser scanning microscopy
CT	Computed tomography
DR	Diffuse reflectance
DRS	Diffuse reflectance spectroscopy
DST	Dorsal side of the tongue
FAD	Flavin adenine dinucleotide
FMN	Flavin mononucleotide
FOR	Fossa of Rosenmüller
FWHM	Full width of half maximum
GI	Gastrointestinal
HNC	Head and neck cancer
HNSCC	head and neck squamous cell carcinoma
HPV	Human papillomavirus
HW	High wavenumber
IR	Infrared
IRB	Institutional Review Board
LDA	Linear discriminate analysis
LIFS	Laser-induced fluorescence spectroscopy
LP	Long-pass
LVs	Latent variables
LVC	Laryngeal vocal cords
MC	Monte Carlo
MRI	Magnetic resonance imaging

NADH	Nicotinamide adenine dinucleotide
NB	Narrow band
NBI	Narrow band imaging
NHG	National Healthcare Group
NLO	Non-linear optical
NIR	Near infrared
OCT	Optical coherent tomography
OPSCC	Oropharyngeal squamous cell cancer
OS	Optical spectroscopy
PCs	Principal components
PCA	Principal components analysis
PET	Positron emission tomography
PLS-DA	Partial least square – discriminant analysis
RF	Radio frequency
PN	Posterior nasopharynx
RGB	Red-green-blue
ROC	Receiver operating characteristic
RS	Raman spectroscopy
SCC	Squamous cell carcinomas
SD	Standard deviation
SE	Standard error
SHG	Second harmonic generation
SNR	Signal-to-noise ratio
SRS	Stimulated Raman scattering
SVM	Support vector machine
THG	Third harmonic generation
TNM	Tumor-nodes-metastasis
UV	Ultraviolet
VB	Vermilion border
VIS	Visible
VR	Vibrational relaxation
WLE	White light endoscopy
WLR	White-light reflectance

Chapter 1 Introduction

1.1 Background

Cancer continues to be a major health threat to human beings in both developed and developing countries over the world. One of most remarkable features is the proliferative ability which makes the cancerous cells spread and invade distant sites of human body after a certain stage of development. The tumor cells can invade and destroy the adjacent tissues, even spread to other locations in the body through lymph or blood. Compared to the malignant tumors, benign tumors do not invade or metastasize in the tissue and they are more manageable with a higher rate of success. Hence, early cancer detection and diagnosis with effective treatments is crucial to reducing mortality rates of patients at a high risk of cancer. According to the cancer statistics 2010, more than 562,875 cancer deaths were reported in United States in 2007, and more than 1.5 million new cancer cases are expected to be diagnosed [1].

Figure 1.1 depicts the long-term trends in cancer incidence and death rates for all cancers by sex. Death rates for all cancer sites combined decreased by 2.0% per year in men from 2001 to 2006 and by 1.5% per year in women from 2002 to 2006 [1]. The statistic evidence shows that mortality rates of cancer have continued to decrease substantially, but cancer still accounts for about 23% of all deaths, ranking second only to heart disease that is the leading cause of death among men and women ages 40 to 79 years [1]. In Singapore, a total number of 51,657 (48.6% males, 51.4% females) incident cancer cases were diagnosed among the resident populations during the period 2006-2010 [2]. The annual incidence rates for total male and female cancer patients for the period 2006-2010 were 277.8 and 288.0 per 100,000 resident populations, respectively. Cancer as a cause of death continued to increase in

importance over the last three decades [2].

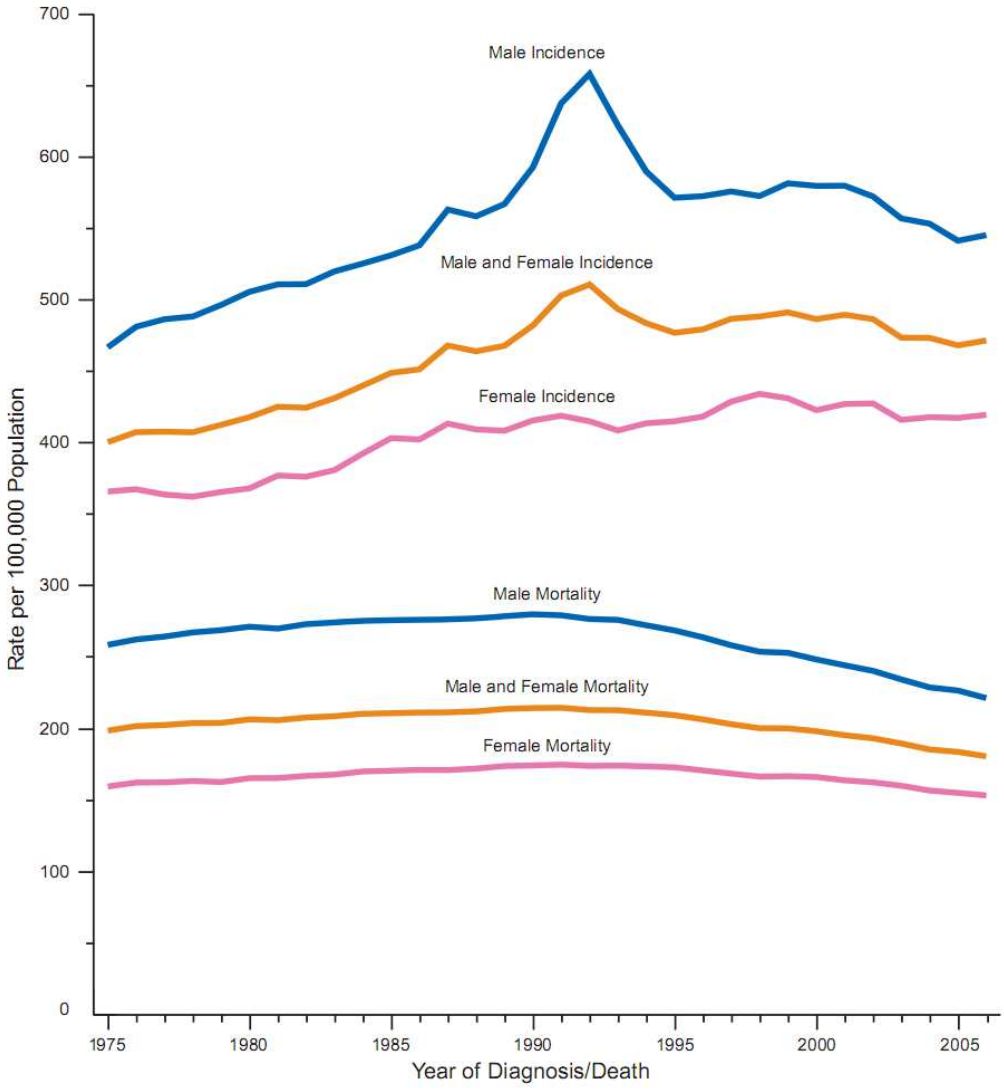

Fig. 1.1 Long term trends in cancer incidence and death rates (1975-2006) [1].

1.1.1 Head and neck cancers

Head and neck cancers (HNCs) refer to a diverse group of biologically similar malignancies and include upper aerodigestive tract (i.e., lip, mouth, tongue, throat, larynx, etc.), salivary glands, nasal cavity, nasopharynx and lymph nodes in the neck [3]. Other cancers occur in the brain, eye, esophagus and thyroid as well as those in muscles and bones are usually not classified as HNCs. The figure 1.2 shows the overview of the head and neck cancer (HNC) regions. Some common symptoms of

HNCs include a non-healing lump, a sore throat, trouble swallowing and a change or hoarseness in the voice.

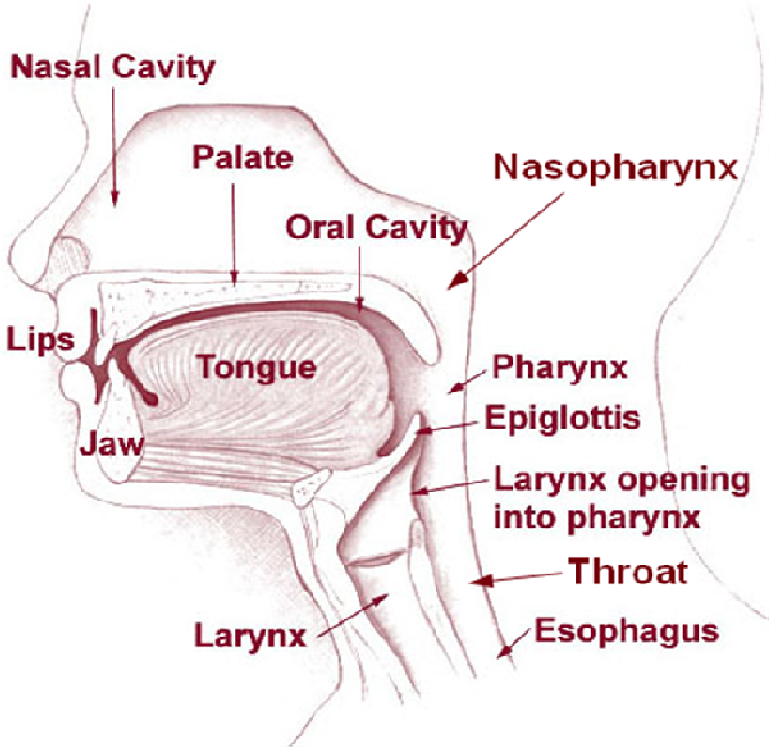

Fig. 1.2 Overview of Head and neck cancer (HNC) regions [4].

Around 40% cases of HNCs occur in the oral cavity which is a major sub-group of HNCs, 25% in larynx, 15% in pharynx and the rest in the remaining sites (e.g., salivary glands, thyroid) [5]. Histologically, more than 90% of all malignant neoplasm of HNCs are squamous cell carcinomas (SCC) which originate from the mucosal lining (epithelium) of these regions [3]. It usually spreads to the lymph nodes of the neck, and this is often the first (and sometimes only) sign of the disease at the time of diagnosis. HNCs are highly associated with certain environmental and lifestyle risk factors, including tobacco smoking, alcohol consumption, ultraviolet (UV) light irradiation, particular chemicals used in certain workplaces and certain strains of viruses, such as human papillomavirus (HPV) [6, 7].

Approximately 500,000 new cancerous cases were confirmed as the head and

neck squamous cell carcinoma (HNSCC) per year, making HNSCC the 6th most common cancer worldwide [6]. Particularly, HNSCC such as laryngeal and nasopharyngeal cancers are diseases with high mortality rates [8]. In East Asia and Africa, the rates of incidence and mortality due to nasopharyngeal carcinomas (NPC) and laryngeal cancer are significantly higher than other parts of the world [9]. The 5-year survival rate decreases significantly due to delayed diagnosis and NPC symptoms generally present at late tumor-node-metastasis. Early identification and adequate preoperative assessment of both nasopharyngeal carcinomas (NPC) and laryngeal cancers allow functional preserving therapy (e.g., radiation therapy, chemotherapy, surgery, etc.) and are also critical measures to reducing the mortality rates of the patients. Yet, early diagnosis of nasopharyngeal and laryngeal precancer and early cancer is clinically challenging even for experienced clinicians with the aid of conventional white-light reflectance (WLR) endoscopy (e.g., microlaryngoscopy, transnasal esophagoscopy) [10]. Moreover, positive identification of these lesions highly relies on visualization of gross morphological manifestations that can be very subjective. Therefore, it would be of imperative clinical value to develop a real-time biomolecular sensitive optical diagnostic technology (‘optical biopsy’) that can assist in the early detection of nasopharyngeal and laryngeal dysplasia and neoplasia during transnasal endoscopic inspections.

1.1.2 Conventional cancer screening methods

Cancer diagnostic techniques developed for generating visual information (e.g., pictures, electrical curves and spectral curves) from the specific organ or tissue have become an important element of early cancer detection. Screening techniques are not only simply used for cancer detection but also important for determining the cancer stage (e.g., Tumor-node-metastasis (TNM) stages) which determines how advanced

the cancer is. The precise location of the cancer is also determined as a reference for the consequent surgery and further treatments. What is more, cancer screening methods also can be used to follow up the therapeutic efficacy and the possible recurrences after the treatments. In the following sections, the conventional biomedical imaging methods and advanced optical diagnostic techniques will be briefly introduced, which include X-ray computed tomography (CT) scan, positron emission tomography (PET), magnetic resonance imaging (MRI) and optical endoscopic imaging techniques.

X-ray Computed Tomography (CT)

X-ray Computed Tomography (CT), one of the biomedical imaging techniques, has been widely practiced in clinic for *in vivo* diagnosis of disease in humans via employing x-ray and tomography together with computer processing. Briefly, the basic components of CT scanners include an X-ray source, a detector and rotation system. X-ray CT imaging consists of directing X-rays through an object from multiple orientations and measuring the decrease in intensity along a series of linear paths. The x-ray transmission intensity is characterized by a single exponential decay function, which describes intensity reduction as a function of initial X-ray intensity, path length, and tissue linear attenuation coefficient. The Three-dimensional (3D) CT image of the inside of an object is generated from a large series of two-dimensional X-ray images taken around a single axis of rotation [11].

Since the first successful application was introduced into clinical practice in 1972 [12], CT scan has been considered as the standard imaging modality for monitoring diseases in the head and neck in the past decades. However, the diagnostic accuracy of CT scan heavily relies on the certain criteria, such as contract-enhancement patterns, which are not very specific [13]. One study for detection of

nodal metastases has reported the diagnostic specificity of ~39% only using CT scan with standard protocols in patients with known carcinoma of oral cavity, oropharynx, hypopharynx or larynx [14]. In addition, there are some other challenges such as financial affordability, radiation dosimetry concerns [15] and time-consuming procedures for the utilization of CT techniques for rapid HNCs detection. For instance, full skull scanning is not necessary as the whole CT scanning procedure is very time-consuming.

Positron Emission Tomography (PET)

The Positron Emission Tomography (PET) is a powerful non-invasive technique to observe the functional difference between healthy and diseased tissue. The principle of PET is based on the detection of very small quantities (picomolar) of biological substances such as carbon-11, oxygen-15, nitrogen-13, and fluorine-18 which are labelled with a positron emitter [16]. After the emission from the parent nucleus, the energetic positron traverses a few millimeters through the tissue until it becomes thermalized by electrostatic interaction between the electrons and the atomic nuclei of the media and combines with a free electron to form a positronium [16]. The positronium decays by annihilation, generating a pair of gamma rays which travel in nearly opposite directions with an energy of 511 keV each, and the opposed photons from positron decay can be detected by using pairs of collinearly aligned detectors in coincidence [16].

Since the initial development of PET around 30 years ago, PET has become an established nuclear imaging modality which has been proved useful in oncology. PET technique was invented at the Mallinkrodt Institute of Radiology at Washington University and the first applications of PC-I in tomographic mode as distinguished from the computed tomographic mode were reported in 1970 [17, 18]. James

Robertson and Z.H. Cho proposed for the first time a ring system that has become the prototype of the current shape of PET[19, 20]. The PET/CT scanner, attributed to Dr David Townsend and Dr Nutt was named by TIME Magazine as the medical invention of the year in 2000 [21].

Many types of tracers have been developed for PET imaging, but the most majority of clinical oncologic PET studies performed at present utilize an analog of glucose, Fluorodeoxyglucose (18F) (FDG) [17]. The use of the radioactive tracers to explore the possibility of cancer metastasis (i.e., spreading to other sites) results in the functional imaging of tissue for medical care (90% of current scans). Currently, FDG is the one of the agents approved by the Food and Drug Administration (FDA) for PET scan in oncology studies. So far thousands of PET scanners are used worldwide, providing substantial advantages over anatomic imaging modalities in oncologic imaging due to its ability of imaging biochemical or physiologic phenomena [17]. Note that PET is a relatively expensive modality, requiring not only a million-dollar-plus PET scanner but also sophisticated and highly trained personnel to generate the radiopharmaceuticals used for PET imaging [17].

Magnetic Resonance Imaging (MRI)

It is well known that human body tissue contains lots of water (each water molecule has two hydrogen nuclei or protons) which gets aligned under a large magnetic field applied. When a person is inside a powerful magnetic field of the scanner, the average magnetic moment of many protons becomes aligned with the direction of the field. A radio frequency (RF) field is briefly turned on, producing a varying electromagnetic field, known as the resonance frequency which flip the spin of the protons in the magnetic field, and after the electromagnetic field is turned off, the spins of the protons return to thermodynamic equilibrium and the bulk

magnetization becomes re-aligned with the static magnetic field [22]. During this relaxation, a RF signal is generated, which can be measured with receiver coils. Hence, such magnetic properties of hydrogen and its interaction with both a large external magnetic field and radio-frequency field can be used to produce highly detailed images of the human body, which can be examined on a computer monitor. Different from ionizing radiation (x-rays) CT imaging, MRI is a non-ionizing imaging technique that can be applied for imaging the whole body of the patients but provide structural information at a high spatial resolution as well as CT scan and it therefore is also routinely used in the initial staging of tumors in patients [13]. Detailed MR images allow clinicians to better evaluate various parts of the body and determine the presence of certain diseases that may not be assessed adequately with other imaging methods such as CT or ultrasound [23].

Currently, MRI is one of the most sensitive imaging modalities for scanning the head (particularly in the brain) and other organs in routine clinical practice. Nevertheless, MRI technique also has relatively poor specificity in the assessment of residual or recurrent disease following radical therapy [24]. The mainly reason is after radiation and/or chemotherapy, changes in tumor metabolism precede morphologic changes. Similarly, after radical surgery or radiation therapy for head and neck malignancies, normal tissue planes are altered substantially, leading to relatively poor specificity in the assessment of residual or recurrent disease following radical therapy [13]. The disadvantages of MRI also include the long operation time with increased risk of motion artifacts and higher cost. Besides, contraindications to MRI include the presence of pacemakers, metal foreign bodies and claustrophobia [25].

Endoscopic imaging techniques

Medical Endoscopy is a diagnostic procedure which allows a clinician to

examine inside human bodies using endoscopes. Usually, an endoscope consists of a rigid or flexible tube, a light source for illumination during the inspection, which is typically guided via an optical fiber, a optical imaging system displaying the picture to the clinician via the eye-piece lens or monitor to the examiner and an additional channel to allow entry of medical instruments to perform necessary operations (e.g., biopsy and resection). Note that there are two types of endoscopes: fiber-optic endoscopes which use a fibre-optic bundle to transfer the image of an internal tissue surface and an eye-piece lens which allows the image to be viewed directly or through a video camera mounted on the endoscope, and videoscopes which install a video chip at the distal end of endoscope instead of the eye-piece to directly transfer images inside of the body to a monitor with a clear view of the area of interest (AOI). The effectiveness of flexible endoscopes relies on the possibility to access areas deep inside the body (e.g., oral cavity, respiratory tract, gastrointestinal tract (GI tract), colon and cervix) with minimal invasiveness than surgical approaches.

In biomedical diagnostic applications, the white-light endoscopy (WLE) is so far well-established and widely used for screening cancer in the head and neck, providing white-light images of the tissue surface with intuitionistic morphology information so that it could be used for quantifying the pathological changes in abnormal tissue. However, it inevitably suffers from the great limitation of low specificity in clinical use which may lead to high false negative rate [26]. Recently, advances in bioengineering have spawned various imaging modalities which have revolutionized endoscopy. Some of these technologies which provide real-time, high-resolution, subcellular imaging such as various spectroscopic techniques, autofluorescence imaging (AFI), narrow band imaging (NBI), optical coherence tomography (OCT) and confocal endomicroscopy are going to be introduced in the

following sections.

1.1.3 Gold standard

Effective cancer diagnosis is used to confirm the presence of disease, to monitor the disease process, and to decide and evaluate the effectiveness of further treatment. Sometimes, it is necessary to repeat the diagnosis when a patient's condition has changed. Diagnostic procedures for cancer may include imaging, laboratory tests (including tests for tumor markers), tumor biopsy, endoscopic examination, surgery, genetic testing, etc. Usually, the definitive diagnosis of most malignancies is confirmed by histological examination of the cancerous cells in tissues. Suspicious tissues of patients can be obtained from a biopsy or surgery during the endoscopic inspection. Tissues biopsied were fixed and then delivered to the pathologists and cut into thin sections, placed on slides and stained with dyes before it can be examined under microscopy. It is the so-called "gold standard" of assessing pathological changes in tissue. Histopathology is the medical specialty that deals with the examination of tissues and cells under the microscope in order to arrive at a diagnosis. When cancer occurs, a pathological diagnosis is the gold standard that indicates the presence or absence of cancer, the type of cancer and its classification. Unfortunately, medical studies over the last two decades have demonstrated that this gold standard is not that consistently reliable for specific tumors such as sarcoma [27]. In fact, multiple studies in various cancers have demonstrated discrepancy rates of up to 30% with an average of approximately 10% [27]. What is more, the long processing time of biopsy and the interpretation of the results may leads to diagnostic delay and the added possibility of taking an unrepresentative sample [28].

1.1.4 Optical techniques for cancer diagnosis

Applying different screening methods is effective for cancer detection and diagnosis and helpful for further treatment to reduce cancer-related mortality, but the limitations for these conventional screening methods which have been discussed above render a demand for new cancer detection and diagnosis techniques. Recently, optical diagnosis techniques have been introduced to cancer detection in biological and medical fields. The optical spectroscopic techniques are to gain both high sensitivity and specificity which show potential to replace the conventional biopsy technique. Compared to conventional biomedical imaging modalities (e.g., ultrasonography, X-ray computed tomography (CT) and magnetic resonance imaging (MRI)) optical spectroscopy and imaging techniques with high biochemical and biomolecular sensitivity and specificity of tissue without labeling possess unique advantages that make them particularly attractive in clinical cancer management in different organ sites such as the breast, cervix, oral cavity, brain and prostate [29-36]. More details on the background of optical spectroscopy (e.g., diffuse reflection, autofluorescence and Raman) and the contribution of these light-tissue interactions for optical signal measurements will be elaborated in more detail in Chapter 2. In the following, some optical screening methods are briefly outlined to show the potential of optical diagnostic techniques for the early cancer diagnosis in the head and neck.

Autofluorescence endoscopy (AFE)

AFE is based on the detection of native tissue fluorescence emitted by endogenous molecules (fluorophores) such as collagen, nicotinamide, adenine dinucleotide, flavins and porphyrins [37]. The endogenous fluorophores emit light (autofluorescence (AF)) of longer wavelengths under excitation at certain wavelength range (e.g., UV, visible (VIS) and near infrared (NIR)). The metabolites may be

responsible for the observed differences in the AF spectra of normal and diseased tissues and normal tissue and vessels respectively appear green and bright green in AFI images [37].

Kulapaditharom et al. (1998) compared the diagnostic ability of using a lung imaging fluorescence endoscopy (LIFE) system and WLE in exploiting the differences in tissue AF properties between normal and cancerous tissues from 25 patients with HNCs [38]. The result showed all 16 cancerous lesions were identified (100%) by LIFE, while WLE achieved only an 87.5% detection rate. LIFE (specificity 87.5%) was more helpful to WLE (specificity 50%) in differentiating inflammation from malignancy, suggesting potential roles of LIFE in early detection, correct staging, and treatment evaluation of HNCs. Zari et al. (2000) used Xillix Technologies (Richmond, Canada) to perform AFI to detect and localize early laryngeal carcinoma [39]. The preliminary study showed that AFI can be a useful complementary method to microlaryngoscopy for detecting and delineating laryngeal malignancies. Paczona et al. (2003) reported tumor presented as darker areas under AF inspection in their study of using autofluorescence videoendoscopy for HNSCC diagnosis [40]. AFI technique has shown better sensitivity than the conventional white light imaging endoscopy. However, it still has some limitations of its low specificity with a high rate of false positive findings. Recently, autofluorescence endoscopy, especially combined with the NBI technique, offers great promise for enhancing endoscopic surveillance performance.

Narrow-band imaging (NBI) endoscopy

In recent year, NBI technique has been shown to visualize capillary patterns in early cancer and is complementary to magnification endoscopy and become a novel blue light endoscopic technique that enhances the diagnostic capability of endoscopes

in characterizing tissues by using narrow band-width filters in a sequential red-green-blue (RGB) illumination system. In contrast to standard white-light endoscopy which employs light in the full visible wavelength range (400–700 nm), NBI uses two discrete bands of light of which central wavelength of each band is 415 nm and 540 nm, respectively, highlighting the superficial vasculature [41]. NBI images on the monitor show that capillaries on the surface are displayed in brown and veins in the sub surface are displayed in cyan. Therefore, NBI can identify superficial mucosal lesions that may be missed by standard white-light imaging (WLI) at endoscopy and further guide biopsy, providing a novel approach to improve the pathologic detection rate and early diagnostic rate of the lesions.

Gono et al. first applied NBI technique to implement a successful detection of superficial, precancerous mucosal lesions over the esophagus [42]. NBI system was therefore believed to be superior to conventional WLE for the detection of superficial mucosal lesions. Watanabe et al. used NBI-assisted rhinolaryngoscopy to detect cancerous lesions in the head and neck of patients with esophageal cancer and prove that the NBI system might cause an improvement in the sensitivity of the detection of HNSCC in patients with esophageal cancer [43]. After that, studies showed that the effectiveness of NBI in the early cancer detection of HNSCC over the mouth floor, nasopharynx, larynx, oropharynx and hypopharynx [44-48]. For now, it has been accepted that NBI has the great capability of detecting superficial mucosal lesions in HNSCC. However, the NBI technique also has some limitation of spectrum analysis on pathological changes due to the application of narrow-bandwidth filters in the imaging system.

Optical coherence tomography (OCT)

OCT technique is a relatively new diagnostic tool which operates in a manner

similar to ultrasound, but uses NIR light instead of sound to discriminate intrinsic differences in tissue structures [49]. It works by projecting a signal of low coherence light on tissue, which is then reflected and measures the magnitude and phase of light from tissues of different depths. Briefly, the infrared light used in the OCT technique is transmitted through a beam splitter (BS) and divided into a reference beam (RB) and a sample beam (SB). The RB is reflected unchanged through a mirror and the SB is dispersed by the different layers of tissue. These beams are then united again in the BS and emitted to a photo detector [50]. The majority of current OCT devices used in clinical trials have an axial resolution of 10 μm and a penetration of up to 2 mm in most tissues [51].

In the head and neck cancer studies, OCT technique has been used to mainly focus on the examination of laryngeal cancer. Sergeev et al. first acquired OCT images of the laryngeal mucosa *in vivo* by passing a fiber-optic interferometer through the biopsy channel of a conventional flexible endoscope [52]. Usually, the basement membrane could be easily identified in normal mucosa tissue layer, which is at the junction of the bright lamina propria and the darker epithelium, but the layered structures are lost associated with neoplastic transformation in HNCs [53]. More recently, OCT has also been comprehensively studied for cancer diagnosis in oral cavity and related work is reviewed elsewhere [54-57].

Confocal endomicroscopy

Confocal endomicroscopy (also called confocal laser scanning microscopy (cLSM)) is another new endoscopic modality developed to obtain very high-resolution images of the mucosal layer. It is based on tissue illumination with a low-power laser with subsequent detection of the light reflected or fluorescence from the tissue through a pinhole. The term confocal refers to the alignment of both

illumination and collection systems in the same focal plane [58-60]. The laser could focus on a selected depth of interest in the tissue and reflected light or fluorescence from the tissue dyed is then refocused back to the detector by the same lens. Only returning light refocused through the pinhole is detected. The light reflected or stained fluorescence at other geometric angles from the illuminated object or refocused out of plane with the pinhole is excluded from detection. This dramatically increases the spatial resolution of confocal endomicroscopy and provide sectioning capabilities [61, 62].

Confocal endomicroscopy is well studied in the digestive tract (e.g., esophagus, stomach and the colon) [58, 63-68]. In contrast, limited work was investigated in HNCs. Just et al. (2006) reported the first application of confocal endomicroscopy for laryngeal endoscopy [69]. By using confocal endomicroscopy with a rigid probe, Patricia et al. (2007) obtained good structural images of tongue using ALA and fluorescein and was able to distinguish morphological differences between normal and lesion tissue [70]. Boris et al. (2010) have investigated the feasibility of using the flexible endoscope in different regions in the head and neck such as oral cavity and the oropharynx after intravenous application of fluorescein sodium [29]. These successful applications of confocal endomicroscopy have demonstrated the potential for a non-destructive optical biopsy to perform microscopic analysis with imaging of live cells. It could be a powerful diagnostic tool before or during therapeutic treatment as more prospective studies have elucidated the clinical value of this technology. However, further technical advances are still required to explore the full potential for cancer detection and diagnosis in the head and neck, such as sectioning at greater depth and reducing scanning time.

1.2 Motivations and Research Objectives

Currently, the endoscopic examination combined with positive biopsy is regarded as the gold standard for cancer detection and diagnosis. Conventional white light endoscopy depends on the outstanding tissue morphological changes, and thus, it suffers from low sensitivity of detection for subtle changes in the mucosa epithelium (e.g., flat lesions, dysplasia, carcinoma in situ (CIS)). Moreover, biopsy is invasive and has the risk with medical complications. For example, it is highly impractical for multiple biopsies of high-risk patients with laryngeal caner, which might affect the quality of the voice. Optical spectroscopic techniques, such as AF spectroscopy and DR spectroscopy, which provide the information about tissue optical properties (e.g., absorption and scattering coefficients), morphologic structures, endogenous fluorophore distribution, blood content (e.g., hemoglobin) and oxygenation associated with neoplastic transformation, have been comprehensively investigated for *in vitro* or *in vivo* precancer and cancer diagnosis in various organs with high diagnostic specificity. Raman spectroscopy provides very specific biochemical and biomolecular information by probing molecular vibrations of tissue. Since all these complementary information are associated with tissue neoplastic transformation and functional changes, the combination of the multimodal spectroscopy and imaging techniques proposed in this study is expected to improve accuracy of cancer detection and diagnosis. It is clinically significant to develop different advanced optical spectroscopic diagnostic techniques systematically to complement conventional endoscopy for improving the diagnosis of cancer non-invasively. Besides, it is also important to compare them individually and in combination for cancer diagnosis and detection in the head and neck.

Therefore, the primary aims of this work are to develop multimodal optical

point-wise spectroscopy (AF/DR/Raman) and imaging technique associated with multivariate statistical technique (e.g., PCA-LDA) and to evaluate its clinical potential for improving cancer diagnosis in human tissues. More specifically, (i) we evaluate the feasibility of using point-wise DR/AF spectroscopy system integrated with AFI system developed for *in vivo* tissue measurements and characterization of optical properties of human tissues in the larynx; (ii) we examine the clinical utility of a rapid fiber-optic NIR Raman spectroscopy system developed for real-time, *in vivo* characterizing the tissue Raman properties of internal organ tissues (e.g., nasopharynx and larynx); (iii) we further investigate the potential of using the endoscope-based high-wavenumber Raman spectroscopy for differentiation from laryngeal cancerous tissue and normal tissues.

1.3 Thesis Organization

This thesis is organized as follows:

Chapter 2 reviews the spectroscopy and imaging techniques and their applications in biomedical diagnosis, as well as multivariate statistical techniques for cancer diagnosis and classification.

Chapter 3 reports the development of the novel integrated simultaneous point-wise AF/DR spectroscopy and endoscopic imaging system, and gives preliminary results on tissue measurement *in vivo* and laryngeal tissue characterization of tumor and cancer using this developed AF/DR spectroscopy technique.

Chapter 4 reports the development of a fiber-optic Raman endoscopic technique and assesses the diagnostic utility of the Raman endoscopic technique in conjunction with multivariate statistical techniques for *in vivo* tissue diagnosis and characterization in the head and neck.

Chapter 5 presents the diagnostic performance of the high-wavenumber (HW)

Raman spectroscopy for cancer tissue diagnosis in the larynx.

The final Chapter 6 concludes the work and proposes future directions in this research.

Chapter 2 Overview of Spectroscopy and Endoscopic Imaging Techniques for Cancer Diagnosis

This Chapter presents the overview of the optical spectroscopy techniques and multivariate analytical techniques as well as their applications in biomedical diagnosis for cancer classification. The necessary principal knowledge and concepts of light-tissue interactions for developing optical spectroscopy technique for precancer and cancer detection are presented first. The related works of using different spectroscopy techniques for cancers diagnosis in the head and neck are also reviewed. In the end, we introduce the principle of multivariate analytical techniques (e.g., PCA, LDA and PLS, etc.) for cancer classification which are mainly employed in this thesis.

2.1 Principles of Optical Spectroscopy and Imaging

Biological tissues are generally optically turbid with the probability of light scattering and absorption exceeding that of conversion to fluorescence. As shown below in Figure 2.1, when the light reaches the tissue, part of the incident light is directly reflected by the surface while the rest part propagates into the tissue. It can be either absorbed or diffusely reflected by the tissue. When the part of the light keeps penetrating into the deeper layer of tissue, some of them will go out after the multiple scattering in tissue and finally come through the tissue into the air while some will be absorbed by the tissue. The former part is called diffused reflection which is determined by the scattering and absorption properties of the tissue. The absorbed light can be converted to fluorescence emission. This fluorescent light scatters in the tissue, where it can either be reabsorbed or remitted from the front tissue surface. The remitted fluorescence detected from the tissue surface thus contains contributions not

only from tissue fluorophores, but also from absorbers and scatters.

When photons are scattered from a molecule, most photons are elastically scattered (also called Rayleigh scattering named after Lord Rayleigh), the scattered photons have the same energy (frequency) as the incident photons. A very small fraction of the scattered photons (approximately 1 in 10 million) is scattered by an excitation, with the scattered photons having a frequency different from, and usually lower than, that of the incident photons, which is called Raman scattering. Typically, Raman scattering (inelastic scattering) is inherently as weak as around 10^{-9} to 10^{-6} of the intensity of the Rayleigh background (elastic scattering), intense monochromatic excitation and a sensitive detector are critical towards obtaining observable Raman signals [71].

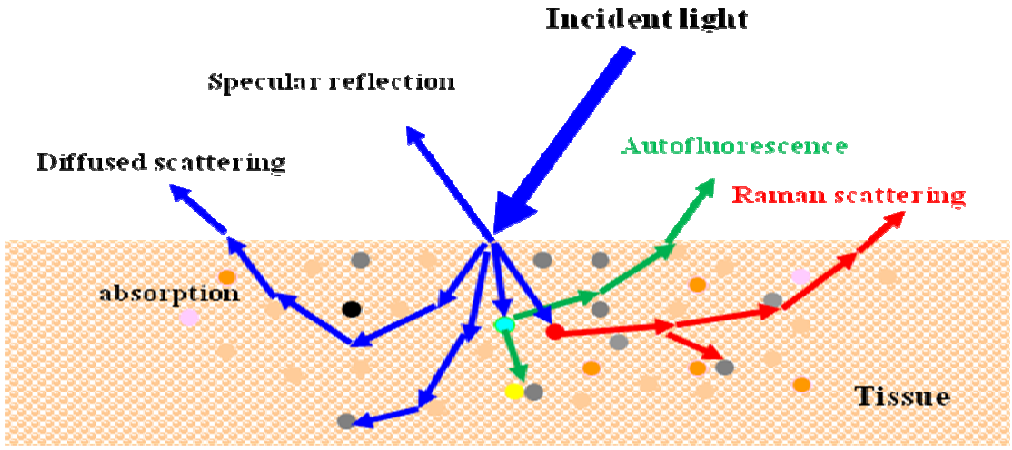

Fig. 2.1 Interactions between tissue and light

2.1.1 Diffuse reflectance

Diffuse reflection is the reflection of light from a surface such that an incident ray is reflected at many angles rather than at just one angle as in the case of specular reflection [72]. An illuminated ideal diffuse reflecting surface will have equal luminance from all directions in the hemisphere surrounding the surface (Lambertian

reflectance) [72]. When the photons enter the tissue, some of the light is absorbed due to absorbers (chromophores), some is reflected (scattered), and some passes through the tissue unperturbed (transmitted) [73]. Since only a portion of the scattered photons are returned to the tissue surface and emerge for detection, and the intensity of the emerging light is reduced (attenuated). Therefore, the relative changes of specific structures within the tissue can be determined based on the measurement of changes in the intensity of reflected light over a spectral range.

Absorbers

There are many biochemical compounds in biological tissue which absorb light radiation, collectively known as tissue chromophores (e.g., hemoglobin, water, melanin, lipid, etc.). Each of tissue chromophores has its own particular absorption spectrum, which describes the level of absorption at each wavelength. Hemoglobin is one of important tissue chromophores which varies in concentration and directly reflects the absorption of blood flows. Hemoglobin is carried by red blood cells and is responsible for transporting oxygen to our tissues. Since hemoglobin can exist in both an oxygenated state (HbO2) and a deoxygenated state (Hb), and since each form of the molecule has its own characteristic absorption spectrum (shown in Figure. 2.2), the identification of tissue oxygenation (HbO2) and blood volume (as total hemoglobin, thb=HbO2+Hb) is possible [73]. In Fig. 2.2, both the oxy- and deoxy- hemoglobin absorb strongly in the visible (VIS) range, but the absorption of deoxyhemoglobin is slightly stronger beyond about 590 nm. Hence, venous blood appears in a darker red than the arterial blood. Note that the absorption of HbO2 drops off very sharply and remains low. However, the absorption of Hb does not drop sharply and stays relatively high. The two absorption spectra cross at around 800 nm (the isosbestic point) [74]. Since oxygen (and therefore a healthy blood

supply) is vital to tissue survival, the ability to detect its presence is of highly clinical significance. By measuring the spectral changes of tissue chromophores (e.g., hemoglobin), tissue blood and oxygenation status can be determined before they are visually apparent. The ability of the technique to make an early assessment of tissue health means that interventions aimed at saving the tissue can be applied before tissue cancerization occurs.

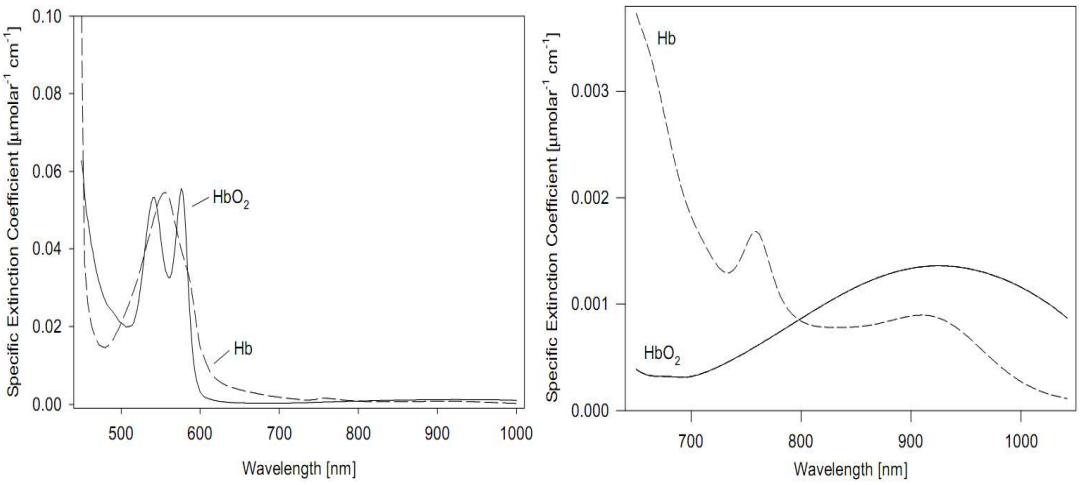

Fig. 2.2 Absorption spectra of oxy- and deoxyhemoglobin in the ranges 450-1000 nm (left), and 650-1050 nm (right) [74].

Water is the most abundant chemical substance in the human body, accounting for 60 to 80 % of total body mass [75]. Water is also considered to be one of the most important chromophores in tissue spectroscopy measurements due to its high concentration in most biological tissue. Figure 2.3 shows the absorption spectrum of water in the range of 200-1000 nm (left) and an expended scale from 650-1050nm (right) [76]. Obviously, absorption rises sharply after 900 nm with increasing wavelength, with a spectral peak being visible at 970 nm. The region of low absorption (wavelength<900nm) acts as a “water transmission window’, allowing NIR spectroscopic measurements through several centimeters of tissue to be made.

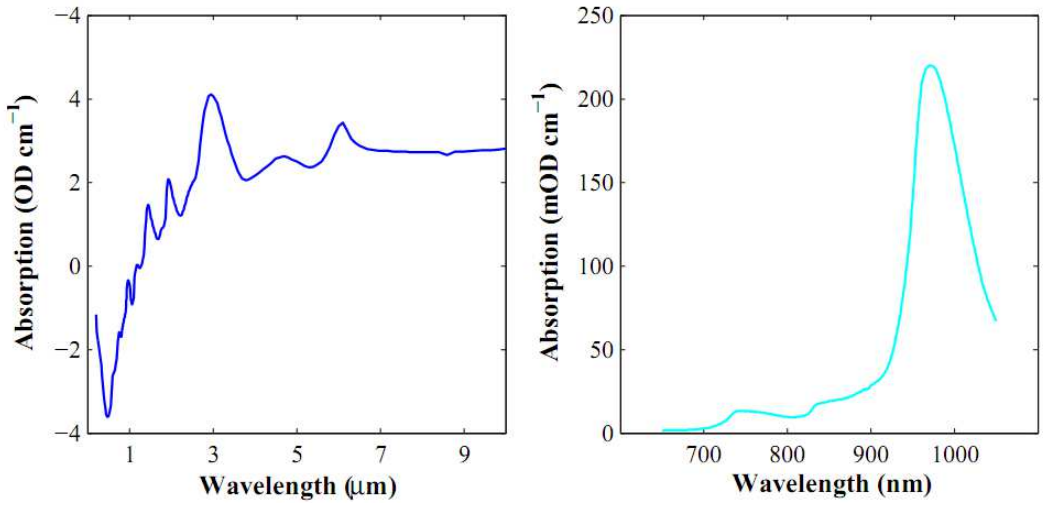

Fig 2.3 Absorption spectrum of water in the ranges 200-1000 nm (left) and an expended scale from 650-1050nm (right) [76].

There are two other tissue chromophores that are worth mentioning: melanin and lipid. Melanin, the pigment found in the epidermal layer of human skin, has a large scattering coefficient in the UV region, which protects the skin from damaging UV radiation from the sun, and a significant absorption coefficient in the NIR region. For lipid, the absorption coefficient is of the same order of magnitude as for water, is low at shorter wavelengths (down to about 600 nm), with a strong peak at about 930 nm.

2.1.2 Fluorescence [77, 78]

Fluorescence phenomenon arises upon light absorption and is related to an electronic transition from the excite state to the ground state of a molecule. In the case of thin (a few micrometer thickness) samples, fluorescence intensity is proportional to the concentration c and the fluorescence quantum yield η of the absorbing molecules [79]. In scattering media, the path lengths of scattered and un-scattered photons within the sample are different, and should be accounted for [80]. Fluorescence is defined as the radioactive transition between two electronic states of the same spin multiplicity

[81]. It is a luminescence in which the molecular absorption of a photon triggers the emission of another photon with a longer wavelength [78].The processes between absorbance and emission of light (fluorescence) are usually illustrated by using simple potential energy diagrams, known as Jablonski diagram, which is used in a variety of forms to illustrate various molecular processes that can occur in excited states. Figure 2.4 depicts the absorption and emission transitions between vibrational sublevels in ground and electronically excited states.

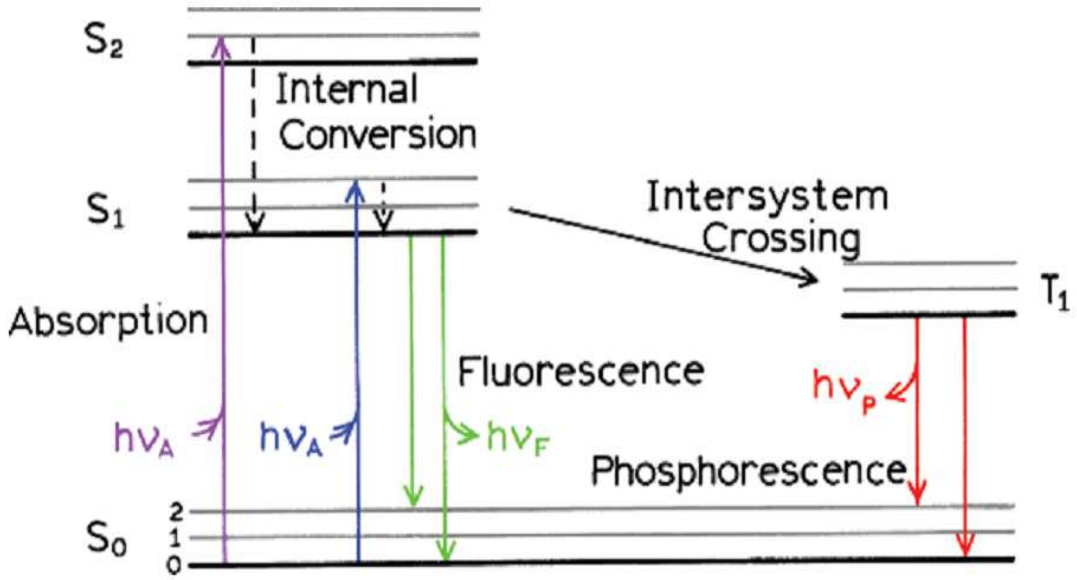

Fig. 2.4 Energy diagram showing absorption and emission transitions between vibrational sublevels in ground and electronically excited states [78].

When a molecule absorbs a photon of incident light and the energy of the incident radiation exactly matches one of the available energy-level transitions, the molecule would move from ground singlet electronic state into successively higher energy excited singlet states and the lowest excited triplet state. After excitation, the molecule is quickly relaxed to the lowest vibrational level of the excited electronic state with emission of a photon. This rapid vibrational relaxation (VR) process occurs on the time scale of femtoseconds to picoseconds. This relaxation process is responsible for the Stoke shift, which describes the observation that fluorescence

photons are longer in wavelengths than the excitation radiation.

Therefore, fluorescence can be expressed as Excitation: $S_0 + hv \rightarrow S_1$, Fluorescence (emission): $S_1 \rightarrow S_0 + hv$, here hv is a generic term for photon energy where: h = Planck's constant and v = frequency of light. State S_0 is called the ground state of the fluorophore (fluorescent molecule) and S_1 is its first (electronically) excited state. A molecule in its excited state, S_1 can relax by various competing pathways besides fluorescence. It can also undergo "non-radiative relaxation" in which the excitation energy is dissipated as heat (vibrations) to the solvent [82]. Excited organic molecules can also relax via conversion to a triplet state which may subsequently relax via phosphorescence or by a secondary non-radiative relaxation step [82].

Autofluorescence [83-85]

Tissue autofluorescence is intrinsic fluorescence emission from endogenous fluorophores in tissue. Generally, the biochemical species in tissue are structural or metabolic, so they can provide a significant amount of information about differences in tissues. When cells in various disease states often undergo different rates of metabolism or have different structures, there are often distinct differences in their fluorescent emission spectra. These differences in fluorescence emission generally depend on at least one of the following parameters: fluorophore concentration or spatial distribution throughout the tissue; local microenvironment surrounding the fluorophores; the particular tissue architecture. Since the biological sources of this fluorescence are endogenous to the tissue, this type of tissue fluorescence is called "autofluorescence". The molecules responsible for this are called fluorophores and include such biological substances as connective matrix (collagen, elastin), cellular

metabolic coenzymes (reduced nicotinamide adenine dinucleotide (NADH), flavin adenine dinucleotide (FAD) and flavin mononucleotide (FMN)), aromatic amino acids (tryptophan, tyrosine, and phenylalanine), byproducts of the heme biosynthetic pathway (porphyrins) and lipopigments (lipofuscin, ceroids, etc.). Each group of fluorophores is characterized by distinct excitation and emission wavelength ranges.

The most important endogenous fluorophores which are molecules widely distributed in cells and tissue is shown in Figure 2.5 as below. Nicotinamide adenine dinucleotide NAD(P) is a major electron acceptor in the energy metabolism pathways. The reduced form, NAD(P)H, is fluorescent and has an excitation maximum at 340 nm and emission maximum at approximately 450 nm. In the case of flavins, the excitation maxima are at 360 and 450 nm, while the emission maximum is approximately 520 nm. Autofluorescence of proteins is associated with amino acids such as tryptophan, tyrosin, and phenylalanine with absorption maxima at 280, 275 and 257 nm, respectively, and emission maxima between 280nm (phenylalanine) and 350nm (tryptophan, which usually dominated the protein emission AF spectrum) [85]. Fluorescence from collagen or elastin using excitation between 300 and 400 nm shows broad emission bands between 400 and 600 nm with maxima around 400, 430 and 460 nm [85]. In particular, fluorescence of collagen and elastin can be used to distinguish various types of tissues, e.g., epithelial and connective tissues [86, 87]. Lipopigments are pigments associated with lipid oxidation products which are generally distinguished in ceroids and lipofuscins [83]. Lipopigments show excitation maxima ranging from 340–395 nm and the emission spectrum has a minor peak at approximately 450 nm and a broad major peak centered at approximately 600 nm, which is responsible for the intense orange autofluorescence that characterize these chromophores [88]. For Endogenous porphyrins, the excitation maximum is at around

400 nm and emission maxima are approximately 630 and 680 nm.

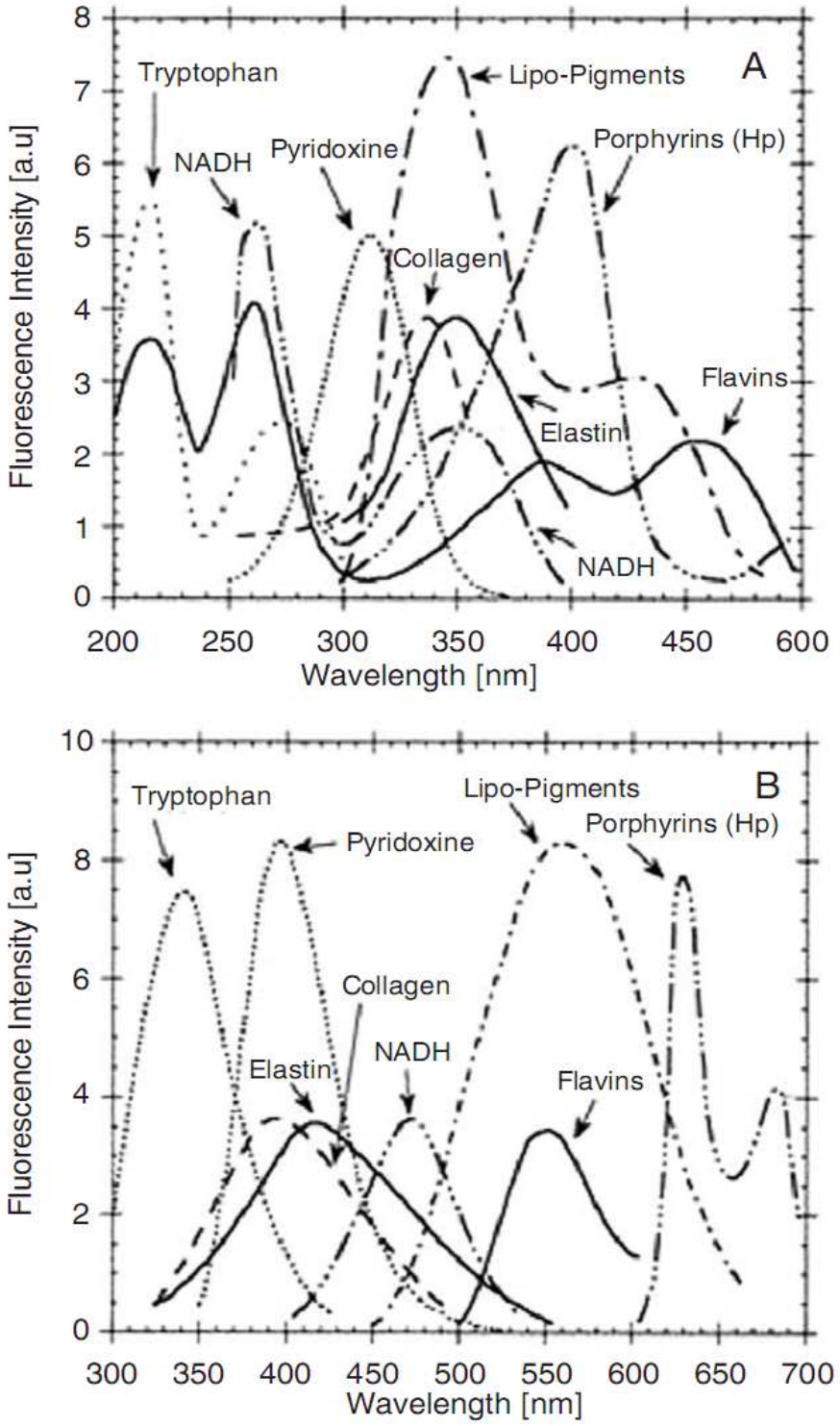

Fig. 2.5 Excitation (A) and emission spectra (B) of the principal endogenous fluorophores [84].

Changes occurring in the cell and tissue during physiological and/or pathological processes result in modifications of the amount and distribution of

endogenous fluorophores in tissues as well as chemical-physical properties of their microenvironments [89]. Therefore, tissue autofluorescence is sensitive to alterations in tissue morphology, neovascularity and biochemistry resulting from malignant transformation. Analytical techniques based on AF monitoring can be utilized to obtain information about morphological and physiological states of cells and tissues. Besides, AF analysis can be performed in real time because it does not require any treatment of fixing or staining of the specimens.

2.1.3 Raman scattering

The Raman scattering process is defined as inelastic scattering of a photon and is also termed Raman Effect. It was discovered by Sir Chandrasekhara Venkata Raman and Kariamanickam Srinivasa Krishnan in liquids and [79] by Grigory Landsberg and Leonid Mandelstam in crystals [78, 81]. Raman received the Nobel Prize in 1930 for his work on the scattering of light. When light is scattered from an atom or molecule, most photons are elastically scattered (Rayleigh scattering), such that the scattered photons have the same energy (frequency) and wavelength as the incident photons. However, a small fraction of the scattered light (approximately 1 in 10 million photons) is scattered by an excitation, with the scattered photons having a frequency different from, and usually lower than, the frequency of the incident photons. In theory, the light interaction with a molecule leads to a polarization of the molecule and then the polarized molecule exhibits an induced dipole moment caused by the external field. The induced dipole moment P is proportional to the electric field E and to a property of the molecule called the polarizability α as shown in the following equation [90]:

$$P = \alpha E; \qquad E = E_0 \cos 2\pi v_0 t\,; \qquad P = \alpha E_0 \cos 2\pi v_0 t$$

In the equations, E_0 and ν_0 are the vibrational amplitude and frequency of the incident light, respectively. The polarizability α is dependent upon the position of the nuclei in the molecule. For a molecule containing N atoms, there are 3N degrees of freedom available to the nuclei. Of there, 3N-6 (3N-5 for a linear molecule) results in the vibrations of the molecule. Considering a diatomic molecule with the single normal coordinate Q_1, the induced dipole moment is as below [90]:

$$P = \alpha_0 E_0 \cos 2\pi\nu_0 t + \frac{1}{2} E_0 Q_1^0 \left(\frac{\partial\alpha}{\partial Q_1}\right)_0 \times \left[\cos 2\pi t(\nu_0 + \nu_1) + \cos 2\pi t(\nu_0 - \nu_1)\right]$$

In the equations, α_0 is the inherent polarizability of the molecule, Q_1^0 and ν_1 are the vibrational amplitude and frequency of the molecule, respectively. The first term represents Rayleigh scattering, and if $\partial\alpha/\partial Q_1$ is nonzero, Raman scattering occurs. The second and third terms represent anti-stokes and stokes Raman scattering, respectively, as shown in Figure 2.6.

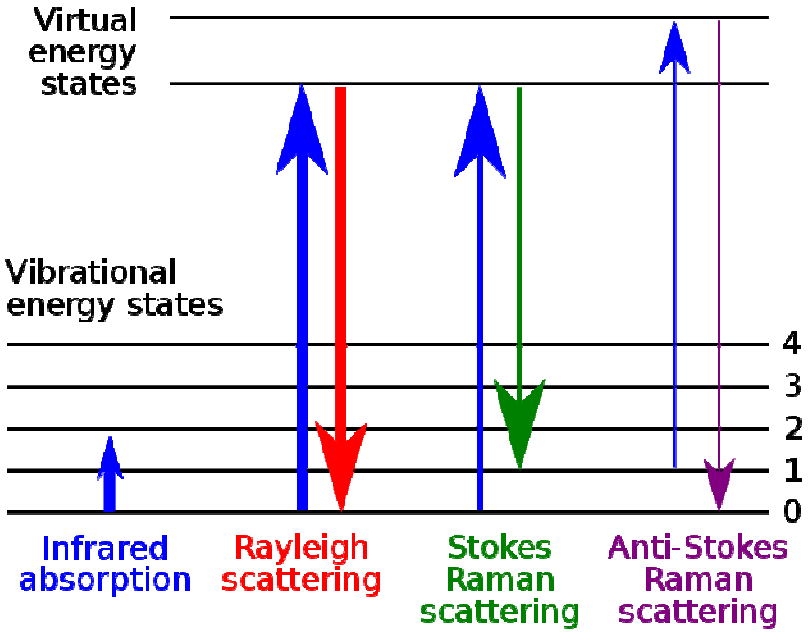

Fig. 2.6 Energy level diagram showing the states involved in Raman signal. The line thickness is roughly proportional to the signal strength from the different transitions [91].

Conventional Raman spectroscopy is based on stokes Raman scattering. A Raman

spectrum is created by determining the Raman intensity as a function of frequency shift ($1/\lambda_{excitation}$-$1/\lambda_{Raman}$), so called Raman shift which is quantified in wavenumber (cm^{-1}). Most commonly, the units chosen for expressing wavenumber in Raman spectra is inverse centimeters (cm^{-1}). Thus, Raman spectrum is characterized by a few distinct bands attributed to specific group of vibrational bonds in the molecules of the sample. In addition, Figure 2.6 also implies that the frequency shift for certain vibration band of the same molecule remains the same for Raman scattering and IR absorption. However, the selection rule of Raman scattering differs from that of infrared (IR) absorption. A molecule absorbs IR light only when the dipole moment changes during the molecular vibration. Whereas, the Raman Effect is caused by an oscillation-induced dipole moment, which means that the molecular interaction with light is through the polarizability of the molecule. Therefore, not all the molecules are both Raman-active and IR-active, which makes Raman spectroscopy and IR spectroscopy complementary to each other.

2.2 Reviews of Optical Spectroscopy Techniques in Cancer Diagnosis

The light interaction between human tissue and radiated energy has been used for disease recognization since the mid-1800s. Optical spectroscopy (OS) is the study of light interaction with tissue and it involves ultraviolet (UV), visible (VIS), near infrared (NIR) or infrared (IR) light, alone or in combination, and is part of a larger group of spectroscopic techniques called electromagnetic spectroscopy. Meanwhile, the great developments of light sources, detectors and fiber optic probes provide opportunities to quantitatively measure these interactions, which yield information for diagnosis at the biochemical, structural or physiological level within intact tissues. In

the past two decades, optical spectroscopic techniques have been a very hot research area, playing an important role in cancer diagnosis. In this section, we will review current advances of several popular optical spectroscopy techniques specifically focusing on diffuse reflectance spectroscopy (DRS), autofluorescence spectroscopy (AFS) and Raman spectroscopy (RS) which are based on characterizing endogenous optical contrasts in tissues.

2.2.1 Diffuse reflectance spectroscopy

Diffuse reflection spectroscopy (DRS) is a non-invasive technique that can be used to quantitatively determine the optical absorption and scattering properties of a turbid medium, which in turn can provide important functional and/or structural parameters relevant to the interrogated target. DRS are usually implemented by coupling a broadband light source (VIS or NIR range) to a medium of interest using a fiber-optical conduit and detecting the remitted signal from the surface using another optical fiber that is fed into a spectrometer [92].The detected signal is sensitive to the distribution of the optical properties of the medium that lie enclosed in a volume between the source and detection fibers. The intensity of board-band diffused reflected light was measured after the incident light undergoes the absorption and scattering interactions with tissue, and the intensity of reflected light after being scattered as function of the wavelength defines the reflectance spectrum. It has been shown previously that the overall depth sampled by the detected signal depends both on the source–detector fiber-probe geometry and on the optical properties of the medium itself [92]. Considered the nondestructive nature of this technique along with its ability to quantify optical absorption, which in turn can directly be related to the concentration and the oxygen carrying status of blood, this method has been widely used in several applications related to diagnosis, prognosis and assessing treatment

response of cancers [92]. However, relatively fewer *in vivo* studies have been conducted on the head and neck such (e.g., cavity, throat, nasopharynx and larynx). Emelink et al. used a specific type of DRS named after differential path-length spectroscopy (DPS) to determine the superficial optical properties of oral mucosa *in vivo* from 31 patients, demonstrating that the mucosa of oral squamous cell carcinoma (SCC) is characterized by a significant decrease in microvascular oxygenation and increase in mucosal blood content compared to normal oral mucosa as well as a significant decrease in scattering amplitude and increase in scattering slope [93]. Mallia et al. presented their results of clinical trials conducted in 29 patients to detect oral precancer using the DR spectral ratio (R545/R575) of oxygenated hemoglobin bands at 545 and 575 nm for grading malignancy and obtained a sensitivity of 100% and specificity of 86% for discriminating precancer (dysplasia) from hyperplasia, and a sensitivity of 97% and specificity of 86% for discriminating hyperplasia from normal [94]. Subsequently, De et al. (2003) compared DRS and fluorescence spectroscopy (FS) to investigate normal and premalignant oral tissue with a non-invasive system *in vivo*. The results of classification between normal and premalignant tissues can reach sensitivity of ~80% and specificity of ~85% with DRS but with FS they obtained better sensitivity (~90%) and poor specificity (~70%) [95]. Besides, some studies also have reported the application of DRS to perform non-invasive optical diagnoses in many different organ sites including the breast, esophagus, GI tract and cervix and to characterize pre-cancers and cancers [96-102].

2.2.2 Autofluorescence spectroscopy

In 1984, Alfano et al. first studied the laser-induced fluorescence spectroscopy (LIFS) to distinguish cancerous tissues from normal and results shown its potential of detecting microscopic lesions during endoscopic examinations [103]. To date,

fluorescence spectroscopy becomes a new diagnostic modality with the potential to bridge the gap between clinical examination and invasive biopsy [104]. Ingrams et al. compared fluorescence spectra from a total of 12 normal (healthy mucosa or benign lesions) and 10 abnormal (dysplastic or malignant) tissue samples to determine whether fluorescence spectroscopy can effectively differentiate dysplasia from normal tissues *in vitro* [105]. Significant spectral differences were observed between two groups and most differences were marked at the excitation wavelength of 410 nm. Using this wavelength, fluorescence correctly diagnosed 20 of 22 samples studied. Betz et al. investigated 49 patients for autofluorescence and spectroscopic measurements under the excitation of 375-440 nm range [106]. The results showed that tumors were obviously distinguished from their surroundings normal through a reduction of green autofluorescence than by ordinary inspection and tumor detection abilities varied for different locations and morphologies. Spectral analysis showed contrasts in autofluorescence intensities between tumor and normal tissues (94.4%). Besides, autofluorescence spectra of normal mucosa varied both inter- and intra-individually. Majumder et al. studied oral cavity caners from 25 patients and applied Principle Components Analysis (PCA), yielding a sensitivity of 86% and a specificity of 63% using [107]. They compared PCA and non-linear classification algorithms to distinguish cancerous and normal tissues from 16 patients as well as 13 healthy volunteers. The non-linear algorithm provided a sensitivity of 93% and a specificity of 96% for the training set, and 95% and 96% for the validation set, which is significant improved performance as compared to the PCA method [108]. De et al. (2003) studied the fluorescence spectra (455–867 nm) of different oral sites (cheek mucosa, tongue, floor of mouth, buccal fold, gingival, lip mucosa ,palate and vermilion border, etc.) were recorded from 97 healthy volunteers using seven excitation wavelengths

(350–450 nm) [109]. Spectral intensity was further studied and applied PCA with classification algorithms. Normalized spectra looked similar for locations, except for the dorsal side of the tongue (DST) and the vermilion border (VB). Porphyrin like fluorescence was observed frequently, especially at DST. PCA and classification confirmed VB and DST to be spectrally distinct. The remaining locations showed large class overlaps. It also revealed that no relevant systematic spectral differences have been observed between most locations, allowing the use of one large reference database. Muller et al. measured 91 oral tissue sites from 15 patients using an upgraded version of the FastEEM instrument, which can provide 11 laser excitation wavelengths from 337–610 nm and broadband white light (350–700 nm), which showed the similar results [110].

One AF spectroscopy study of nasopharyngeal carcinoma and normal tissue from 27 subjects was conducted by Qu's group [111]. Two algorithms (two-wavelength and three-wavelength) for discrimination of cancer and normal tissues were compared. For the two-wavelength algorithm, carcinoma can be differentiated from normal tissue with a sensitivity and specificity of 93% and 92%, respectively. For the three-wavelength algorithm with compensation of variation of blood content in tissue, a sensitivity of 98% and specificity of 95% were achieved. In later study, they investigated larger data set (85 carcinoma, 131 normal) from 59 patients and compared two diagnostic algorithms based on PCA and the ratio of the spectral signals between multiple-wavelength bands [112]. The PCA based algorithm can differentiate carcinoma lesions from normal tissue with 95% sensitivity and 93% specificity. With 94% sensitivity, the specificity of the multiple-wavelength ratio algorithm is about 83%.

Eker et al. performed an *in vivo* spectroscopic measurement in laryngeal

carcinoma using laser light at 337 and 405 nm for excitation [113]. They were able to differentiate between benign and malignant tissue in 85% of the cases. In a prospective study by Arens et al., 42 patients with suspected one-sided precancerous or cancerous lesions of the vocal folds were investigated during microlaryngoscopy [114]. Normal mucosa presented a bright green fluorescence under blue light excitation (375-440 nm) and the intensity increased from the ventricular folds to the subglottic area. Precancerous as well as cancerous lesions showed a significant decrease in autofluorescence intensity. They achieved a sensitivity of 97% and a specificity of 82%.

In recent times, times-resolved (time-domain and frequency-domain) autofluorescence spectroscopy techniques, which are different from the steady-state (spectral-resolved or intensity measurements) autofluorescence spectroscopy that measures the overall intensity, peak wavelength and spectral shape from tissue, become a new tool for cancer diagnosis in the head and neck. Some pilot studies on oral buccal model were conduct by Farwell et al. and Meier et al. [115, 116]. The results revealed the significance of the shorter lifetime between 440-470 nm in malignant tissues. This addition of time-resolved fluorescence derived parameter average lifetimes as well as the Laguerre coefficients, LEC-2 significantly improved the capability of fluorescence spectroscopy–based diagnostics in the head and neck, suggesting the potential of time-resolved fluorescence spectroscopy as a non-invasive diagnostic technique for HNSCC.

2.2.3 Raman spectroscopy

In recent years, Raman spectroscopy, especially near-infrared Raman spectroscopy, has been investigated for two decades and considered a complementary or even as an alternative technique for biopsy and shown promising results for the

point-wise diagnosis and characterization of disease progression in various organs (e.g., gastrointestinal tracts, oral cavity, nasopharynx, larynx, lung, cervix, bladder, skin and the breast) with high biomolecular specificity [117-140]. However, the applications of Raman spectroscopy in the clinical medicine are still in the early stages of development. In particular, clinical studies in head and neck area are still scant [141]. Malini et al. studied the ability of Raman spectroscopy to discriminate 216 spectra (10 pre-malignant, 90 malignant, 37 inflammatory and 79 normal) of tissue samples from the oral cavity [142]. Spectral profiles of different conditions showed pronounced differences between one another. Spectra of normal tissues were attributed mainly to lipids whereas pathological tissue spectra are dominated by proteins. It was shown that by the method of PCA combined with multiparameter limit tests all the four tissue types could be differentiated and diagnosed correctly. In the study of Oliveira et al., a total of 123 spectra were obtained and divided in normal and malignant tissue groups and analyzed statistically through PCA and classified using Mahalanobis distance [143]. Major differences between normal and malignant spectra seemed to arise from the composition, conformational, and structural changes of proteins, and possible increase of its content in malignant epithelia. The algorithm based on PCA was able to separate the samples into two groups (i.e., normal and carcinoma). For the algorithm training group, 91% sensitivity and 69% specificity were observed, while the prospective group had 100% sensitivity and 55% specificity.

For nasopharyngeal cancers, Lau et al. (2003) used Raman spectroscopy to classify tissue obtained from the post-nasal space in cancer and normal patients [129]. The importance of utilizing Raman spectroscopy in the nasopharynx is the ability to detect sub-mucosal tumors associated with this cancer in this region, preventing the need for random biopsy. Noted that NIR Raman spectroscopic studies on the

nasopharynx and larynx have been limited to *in vitro* tissue Raman measurements due to the lengthy data acquisition times as well as technical challenges in making miniaturized flexible fiber-optic Raman probes with high collection efficiencies while effective elimination of interferences from fluorescence and silica Raman signals [144]. Stone et al. (2000) performed a feasibility study of the use of Raman spectroscopy for early diagnosis of laryngeal malignancy. The diagnostic sensitivities and specificities of ~70-95% have been achieved for differentiation between different laryngeal pathologic types (e.g., normal, dysplasia and carcinoma) *in vitro* using NIR Raman spectroscopy, revealing that Raman spectroscopy may become a useful adjunct to pathological diagnosis allowing directed or guided biopsies and assessment of adequacy of resection margins [133]. Lau et al. confirmed the feasibility of nasopharyngeal and laryngeal cancer diagnosis *in vitro* [129, 130]. Teh et al. reported the diagnostic sensitivity of 88.0% and specificity of 91.4% for detecting laryngeal carcinoma *in vitro* when coupled with random recursive partitioning ensemble techniques [132]. This study showed that NIR Raman spectroscopy in conjunction with random forests algorithm has a great potential for the rapid diagnosis and detection of malignant tumors in the larynx.

In addition, Harris et al. (2009) evaluated the possibility of using Raman spectroscopy to discriminate between cancer and normal patients through a peripheral blood sample [145]. 40 blood samples were obtained from patients with HNCs and patients with respiratory illnesses to act as a positive control. The Raman spectra acquired from samples were further analyzed through building a classifier for differentiation between the cancer and respiratory patients' spectra, yielding a sensitivity of 75% with a specificity of 75% with a “trained” evolutionary algorithm. This preliminary study showed the feasibility of using Raman spectroscopy in cancer

screening and diagnostics of solid tumors through a peripheral blood sample,

Note that NIR Raman spectroscopy exhibits advantages for the detection of HNCs, such as non-invasive, real-time and higher accuracy, as compared to conventional screening/diagnosis methods, however, most work in literature above was studied on *in vitro* tissue samples.

2.3 Multivariate Statistical Analysis Techniques for Tissue Classification

Optical spectroscopy techniques may be facilitated to provide biomolecular information from biological tissues and present the intensity information on a spectrum to significantly improve medical diagnosis. Whereas, the spectral dataset usually are multivariate function of wavelengths and consist of results of observation of many variables (e.g., wavelength and Ramsn shift) for different classes (e.g., normal, benign, dysplasia, neoplasia and carcinoma). On the other hand, biochemical information from each individual spectrum generally covers many overlapping bands. As such, it is not easy to differentiate normal tissue from pre-cancer or cancer by directly visual inspection for subtle change in tissue pathology. Therefore, mathematical statistical techniques are required to be implemented as effective classification algorithms to reduce this massive dimensional space to an interpretable dimensional space for tissue characterization.

Multivariate statistical analysis is concerned with data that consists of sets of measurements on a number of individuals or objects [146]. In general, There are many different models including principle components analysis (PCA), linear discriminant analysis (LDA), partial least squares regression (PLS regression), analysis of variance (ANOVA), artificial neural network (ANN) and support vector machines (SVM),

which have been extensively applied as diagnostic models for classification of different cancers in tissue spectroscopy [147-157]. However, different techniques could not sufficiently satisfy the requirements in clinical applications. Therefore, we make a brief introduce of the popular statistical analysis techniques (e.g., PCA, LDA, PLS, etc.) in tissue spectroscopy in the following sections.

2.3.1 Principle component analysis (PCA)

Principal component analysis (PCA) is a variable reduction procedure that uses an orthogonal transformation to convert a set of observations of possibly correlated variables into a set of values of uncorrelated variables (called principal components (PCs)) which account for most of the variance in observed variables and may then be used as predictor or criterion variables in subsequent analysis. The number of PCs is less than or equal to the number of original variables. This transformation is defined in such a way that the first principal component has the largest possible variance which accounts for as much of the variability in the data as possible, and each succeeding component in turn has the highest variance possible under the constraint that it should be orthogonal to (i.e., uncorrelated with) the preceding components [158]. As reduction of dimensionality focusing on a few PCs versus many variables is a goal of PCA, therefore, several criteria have been proposed to determine how many PCs should be investigated and how many should be ignored [159, 160]. One common criterion for ignoringi PCs at the point wehre the next PC offers increase in the total variances. Another is to include all those PCs up to a predetermined total percent variance explained, such as 90%. In addition, PCA decomposes the spectral data matrix into scores and loadings, which also can be used to provide a method to evaluate the relationships between samples measured and help to detect the potential outliers via inspecting the plots generated using scores [161,

162].

2.3.2 Linear discriminant analysis (LDA)

Linear discriminant analysis (LDA) is a statistical method used in pattern recognition and machine learning to seek a linear combination of features from measurement variables which characterizes or separates two or more classes of objects. LDA is closely related to ANOVA (analysis of variance) and regression analysis, which also attempt to express one dependent variable as a linear combination of other features or measurements. Usually, LDA is also closely related to principal component analysis (PCA) because they both look for linear combinations of variables which best explain the data, while LDA explicitly attempts to model the difference between the classes of data. PCA on the other hand does not take into account any difference in class. The aim of LDA is to find a discriminant function line that maximizes the variance in the data between groups and minimizes the variance between members of the same group. Thus, the new measurements from tissue samples can then be classified according to its position with respect to the discriminant function line [89].

2.3.3 Partial least squares (PLS)

Partial least squares (PLS) (also called Projection to Latent Structure) regression is a popular method for modeling in industrial applications, providing an alternate approach to PCA technique. PLS technique is an extension of the multiple linear regression model and a linear model specifies the (linear) relationship between a dependent (response) variable Y, and a set of predictor variables, the X's. Briefly, PLS tried to find out the linear decomposition of X and Y such that $X = TP^T + E$ and $Y = UQ^T + F$, where T = X-scores, U = Y-scores, P=X-loadings, Q=Y-loadings, E=X-

residuals and F=Y-residuals. Decomposition is finalized to maximize covariance between T and U, and PLS algorithm works in the same fashion whether Y is single response or multi-response. In the previous sections, we introduced that PCA was widely used to reduce the spectral dimension by extracting a set of PCs accounting for maximum spectral variations for tissue disease diagnostics. But the use of PLS, the regression extension of PCA, would be beneficial for spectroscopic tissue diagnostics by providing group affinities (class membership of zeros and ones) information to maximize the variations between groups of samples. It follows the principle of PCA, but further rotates the components (latent variables (LVs)) to achieve the maximum group separation [163, 164]. Hence, the LVs could explain the diagnostic relevant variations rather than the significant differences in the dataset.

2.3.4 Support vector machine (SVM)

As another powerful multivariate technique, Support Vector Machines (SVM) was based on the machine learning method and was developed by Vapnik in 1995 [165, 166]. In the past decades, it has attracted great attention due to its capability of producing models that generalized well in classifying the unseen data [167-170]. Basically, SVM classifies two separable dataset which belong to two different classes through the use of a hyperplane [166]. Intuitively, a good separation is achieved by finding the hyperplane which has the largest distance to the nearest training data point of any class (so-called functional margin), since in general the larger the margin the lower the generalization error of the classifier. Hence, there are infinitely many hyperplanes that separate the two classes, but SVM classifiers find the optimized hyperplane that maximizes the distances between the two groups by solving a quadratic optimization equation, the Lagrangian dual problem. In addition to performing linear classification, SVMs can also efficiently perform non-linear

classification using kernel trick, implicitly mapping their inputs into high-dimensional feature spaces [166].

2.3.5 Artificial neural network (ANN)

An Artificial Neural Network (ANN) (also known as neural network (NN)) is a mathematical model or computational model inspired by the structure and/or functional aspects of biological neural networks such as neurons, axons, dendrites, and synapses, which constitute the processing elements of biological neural networks investigated by neuroscience. It is an information-processing system that has certain performance characteristics in common with biological neural networks. Generally, An ANN generally consists of some interconnected processing elements, called nodes, which are connected to each other via a combination of adaptable interconnections, called weights. To date, it has become another non-linear statistical data modeling tool which can be used to develop a classification algorithm [171]. An ANN system has three layers. In the first layer (input layer), neurons act as input to send data via synapses to the second layer of neurons, and then via more synapses to the third layer of output neurons. More complex systems will have more layers of neurons with some having increased layers of input neurons and output neurons. The synapses store parameters called “weights” that manipulate the data in the calculations. In an ANN performance, there are two phases which are training phase and test phase. The former starts with assigning initial values of parameters to the ANN and presenting input patterns. The process proceeds with adaptation of weights until the ANN learns these patterns. In a test set, the patterns which are not used in training phase are presented to ANN and ANN’s outputs are used to evaluate ANN’s performance.

Chapter 3 Development of Simultaneous Point-wise AF/DR Spectroscopy and Endoscopic Imaging Technique

In this chapter, we report the development of an integrated point-wise spectroscopy and autofluorescence (AF) endoscopic imaging technique for real-time *in vivo* tissue measurements at endoscopy. A unique customized point spectrum optical design is implemented to realize real-time AF imaging and AF/or diffuse reflectance (DR) spectroscopy measurements from a small tissue area of interest (AOI) on the AF image. By applying this point-wise spectroscopy, both the AF image and the point-wise AF/DR spectra can be simultaneously acquired from the oral cavity *in vivo* within 0.1 second, suggesting the potential of the integrated spectroscopy and endoscopic imaging technique developed to facilitate *in vivo* tissue diagnosis and characterization at endoscopy.

Further, we evaluate the diagnostic utility of the combined AF and DR spectroscopy for improving cancer diagnosis in head and neck at clinical endoscopy. The above point-wise AF/DR spectroscopy with endoscopic imaging guidance was employed for spectroscopic measurements of normal (n = 207) and cancer (n = 239) tissues specimens from 30 patients. The composite AF and white light reflectance (WLR) spectra in the range of 500–660 nm were analyzed using principal component analysis (PCA) and linear discriminant (LDA) to extract diagnostic information associated with distinctive spectroscopic processes of tissue malignancies. PCA-LDA diagnostic modeling on the combined AF and WLR yielded a diagnostic accuracy of 92.2% (sensitivity of 85.5% and specificity of 94.0%) for tumor and normal tissues

classification. The integration area under the receiver operating characteristic (ROC) curve using the combined point-wise AF/DR spectroscopy was 0.982, which is superior to either the AF or DR spectroscopy alone. This study demonstrates that the complementary AF/DR spectroscopy techniques can be integrated together with endoscopic imaging system and has potential to improve the early cancer diagnosis and detection in the head and neck.

3.1 Introduction

It is well known that early diagnosis and localization of head and neck cancer with effective treatment is critical to decrease the mortality rates [172]. However, the conventional white light reflectance (WLR) endoscopy, which is accepted as the gold standard method for screening and surveillance of cancer in the head and neck, heavily relies on the observation of tissue gross morphological changes associated with neoplastic transformation. Subtle tissue changes may not be apparent, limiting its diagnostic accuracy. Positive endoscopic biopsy is the standard means for head and neck cancer diagnosis, but is invasive and impractical for screening high-risk patients who may have multiple suspicious lesions. Hence, it is highly desirable to develop advanced optical techniques to complement the WLR endoscopy for improving the early cancer diagnosis and characterization during clinical examinations.

In the past decades, despite AF imaging technique is capable of detecting the changes of endogenous fluorophores and morphological architectures of tissue and has been developed to significantly improve the diagnostic sensitivity of early neoplastic lesions at endoscopy, however, AF imaging still suffers from moderate diagnostic specificities [173]. Optical spectroscopic techniques, such as AF spectroscopy and DR spectroscopy, which provide the information about tissue optical properties (e.g., absorption and scattering coefficients), morphologic structures,

endogenous fluorophore distribution, blood content (e.g., hemoglobin) and oxygenation associated with neoplastic transformation, have been comprehensively investigated for *in vitro* or *in vivo* precancer and cancer diagnosis in various organs with high diagnostic specificity [174-177]. The combination of AF imaging with optical spectroscopic technique offers a potential of providing both high diagnostic sensitivity and specificity for cancer tissue diagnosis and detection [176-179].

Therefore, we developed an integrated point-wise spectroscopy (AF/DR) and AF imaging technique for real-time *in vivo* tissue measurements at endoscopy. Different from other previous work which also integrated imaging with spectroscopy, but limited to spectral measurements at the centroid of the endoscopic field of view [178, 179], in our embodiment, the *in vivo* point-wise AF/DR spectra can be quickly acquired from any specific areas of the imaged tissue of interest under the AF/WLR imaging guidance during endoscopic examination.

3.2 Integrated Point-wise DR/AF Spectroscopy and Imaging System

3.2.1 Novel point-wise AF/DR spectroscopy

The schematic diagram of the integrated point-wise spectroscopy and AF endoscopic imaging technique developed for *in vivo* tissue measurements at endoscopy is shown in Figure 3.1. This novel system mainly consists of a dedicated 300 W xenon short arc lamp coupled with two customized band-pass (BP) filters (BP1: 375-440 nm for AF excitation; BP2: 400-700 nm for WL illumination) for AF/DR spectroscopy and imaging, a medical endoscope (HOPKINS II 7230BP, Karl Storz, Germany), a sensitive three-chip charge-coupled device (CCD) camera (red (R) channel (600-700 nm); green (G) channel (500-580 nm), and blue (B) channel (400-

480 nm); 752x582 pixels, TRICAM® SL II, Karl Storz, Germany), a spectrograph equipped with a CCD detector (FWHM of ~1.5 nm with a 600 gr/mm holographic grating, USB2000, Ocean Optics Inc, Florida), and a specially designed point spectrum optical adaptor (inset of Fig. 3.1) for realizing simultaneous *in vivo* endoscopic imaging and point-wise AF/DR spectral measurements on the specific areas of the imaged tissue of interest. The customized optical adaptor comprises three lenses (f=50 mm), a thin quartz glass plate (30 × 30 × 1 mm^3) coated with a gold mirror (diameter of 100 μm, reflection of ~99% in 400-1000 nm) and a 2-D motorized translational stage (travel range: 13 mm; 8MT184-13, Standa Inc., Lithuania) for controlling the rapid movement of the gold mirror to realize the spectral measurements on the points of interest of the tissue imaged.

For simultaneous AF imaging and spectroscopy measurements, the filtered blue excitation light (375-440 nm) is conducted into the endoscope via a flexible fiber-optic light guide and shines onto the tissue with an incident power of 35 mW on the fiber tip of the endoscope. AF emitted from the tissue is collected by the same fiber tip of the endoscope, and then coupled into the customized optical adapter by passing through a long-pass (LP) filter (cut off at 480 nm) for removing the interference of the excitation light scattered from tissue, and then is focused onto the quartz glass plate which is positioned at the interim imaging plane of Lens 1 with an orientation of 45° with respect to the incident light direction. The tissue fluorescence light passes through the 45° oriented glass plate and is focused onto the 3-chip CCD camera through Lens 2 for fluorescence imaging measurements. Meanwhile, a very small portion of tissue fluorescence is reflected from the 100 um gold mirror coated on the quartz plate and focused onto a 100 μm fiber via Lens 3 which is connected to the spectrograph for fluorescence spectroscopic measurements.

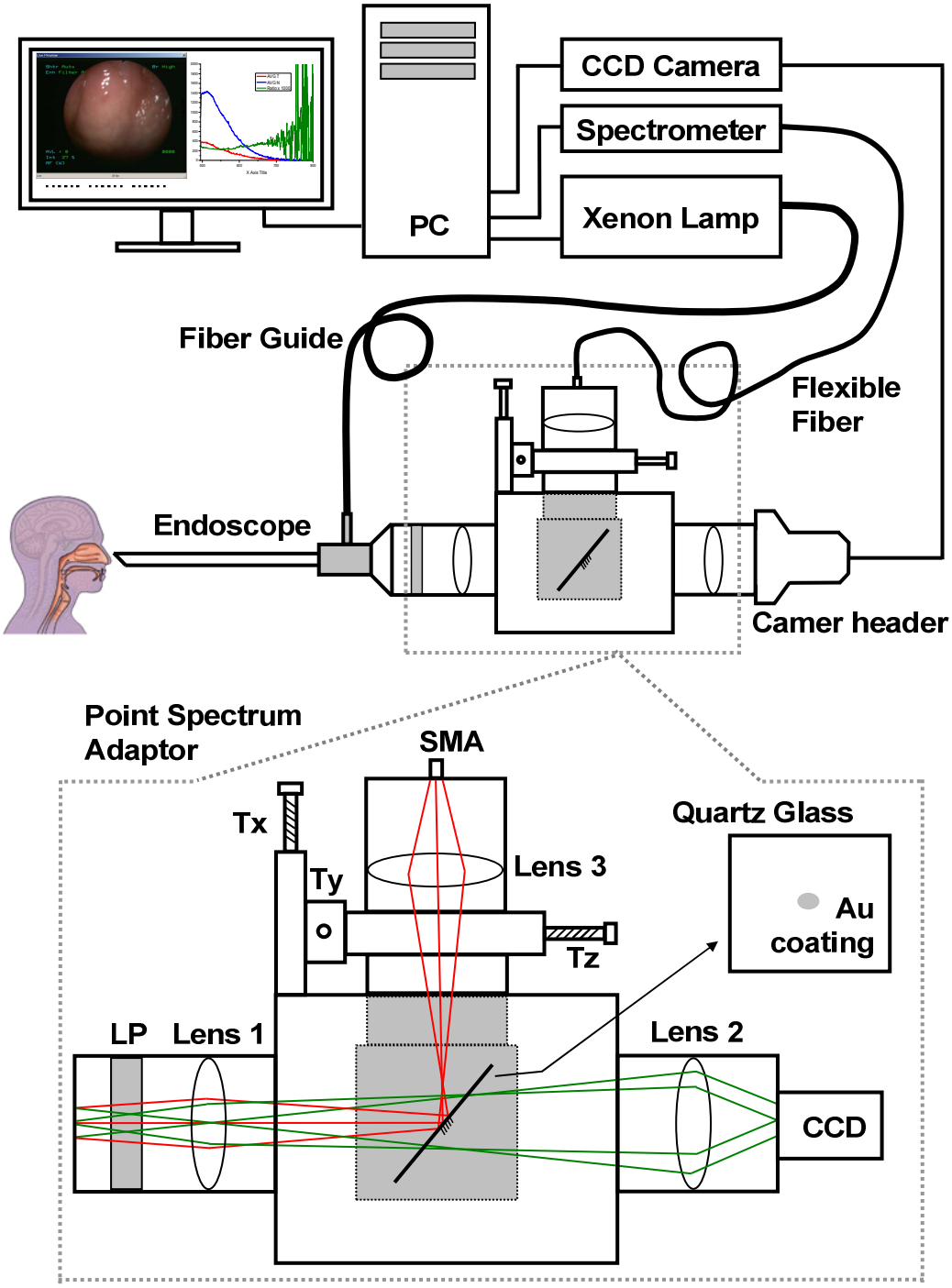

Fig. 3.1 Schematic of the integrated point-wise spectroscopy and autofluorescence (AF) imaging system for *in vivo* tissue measurements at endoscopy.

Further, an automatic motorization of the small gold mirror coated on the quartz plate together with the point-wise spectral measurement module enables a rapid movement of the dark spot (of ~ 0.5 mm in diameter due to the refection of gold mirror in the point spectrum optical adapter with 5 × magnifications) on the image to

any spot of the imaged tissue of interest (see video 3.1). Hence, the AF imaging and point-wise AF spectroscopy now can be simultaneously acquired from the same tissue imaged without introducing an optical fiber catheter into the instrument channel of an endoscope as in conventional endoscopic spectral measurements which prolong the endoscopic operation procedures. Similarly, the simultaneous WLR imaging and point-wise DR spectroscopy on the same tissue can also be realized simply by switching the excitation light filter to the white light illumination mode (BP2: 400-700 nm) and removing the 480 nm LP filter in the customized optical adaptor.

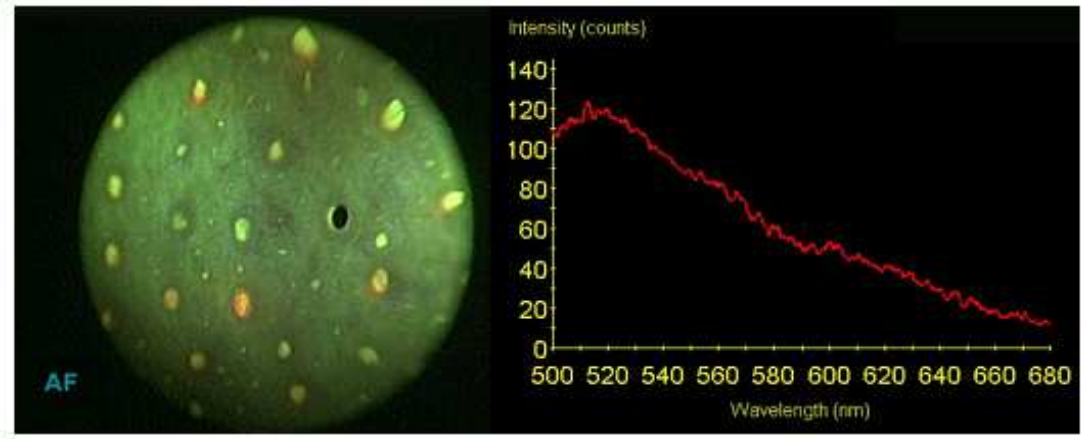

Video 3.1 Video illustrating simultaneous AF imaging and point-wise AF spectral *in vivo* measurements of the cheek in real-time during AF endoscopic imaging (QuickTime, 11 MB). [URL: http://dx.doi.org/10.1117/1.3475955.1].

By rapidly moving the reflection mirror in the optical adapter, we also demonstrate the ability of the integrated endoscopic imaging and spectroscopy technique developed for pinpointing the spectral properties of specific area of interest on the tissue imaged. Video 3.1 illustrates the *in vivo* AF image of the cheek acquired together with simultaneous AF spectral measurements on different spots of the tissue imaged during rapid scanning of the gold reflection mirror (shown as dark spot in AF image). The point-wise spectral measurements across the entire image size of ~10 mm can be quickly completed within 2 to 3 seconds, making the *in vivo* AF measurements feasible in clinical settings. *In vivo* AF spectral differences of different spots on the

same tissue imaged can also be clearly identified (Video 3.1), indicating the ability of our technique developed for revealing the inhomogeneity of endogenous fluorophore distributions in tissue. Our point-wise spectrum adapter design associated with rapid scanning and optics allows for a more convenient spectral measurement on the point-of-interest of the tissue imaged for spectral analysis, and may have a significant impact for practical clinical applications.

In this work, in order to apply this novel system into clinical practice for improving the working efficiency of measurements, we have also developed a Maltlab/C-based software with Bluetooth mini-keyboard remote control for performing real-time endoscopic image (WLR/AF) acquisition and point-wise spectral measurements and automatic data-processing (e.g., wavelength of interest selection, system spectral response calibration, CCD dark-noise subtraction, spectral curve smoothing, signal saturation detection, etc.). Both the live AF/WLR image and AF/DR spectrum can be simultaneously displayed on the computer monitor for real-time review, and stored in the computer for further diagnostic analysis.

3.2.2 *In vivo* experimental measurement in the head and neck

We have applied the integrated point-wise spectroscopy and endoscopic imaging technique developed for *in vivo* tissue measurements in the head and neck. Figure 3.2 shows an example of *in vivo* WLR images and the corresponding DR spectra of different tissue sites (i.e., chin, buccal mucosa, dorsal of the tongue, and lower lip) simultaneously acquired from a healthy volunteer under the white light illumination mode. Point-wise DR spectra from different anatomical locations (dark spots in the WLR images in Fig. 3.2a) in the oral cavity can be acquired within 10 ms, and the absorption peaks (e.g., 420, 540 and 580 nm) attributed to hemoglobin

absorptions in the vessels can be clearly identified, but with large absorption variations among different tissue locations.

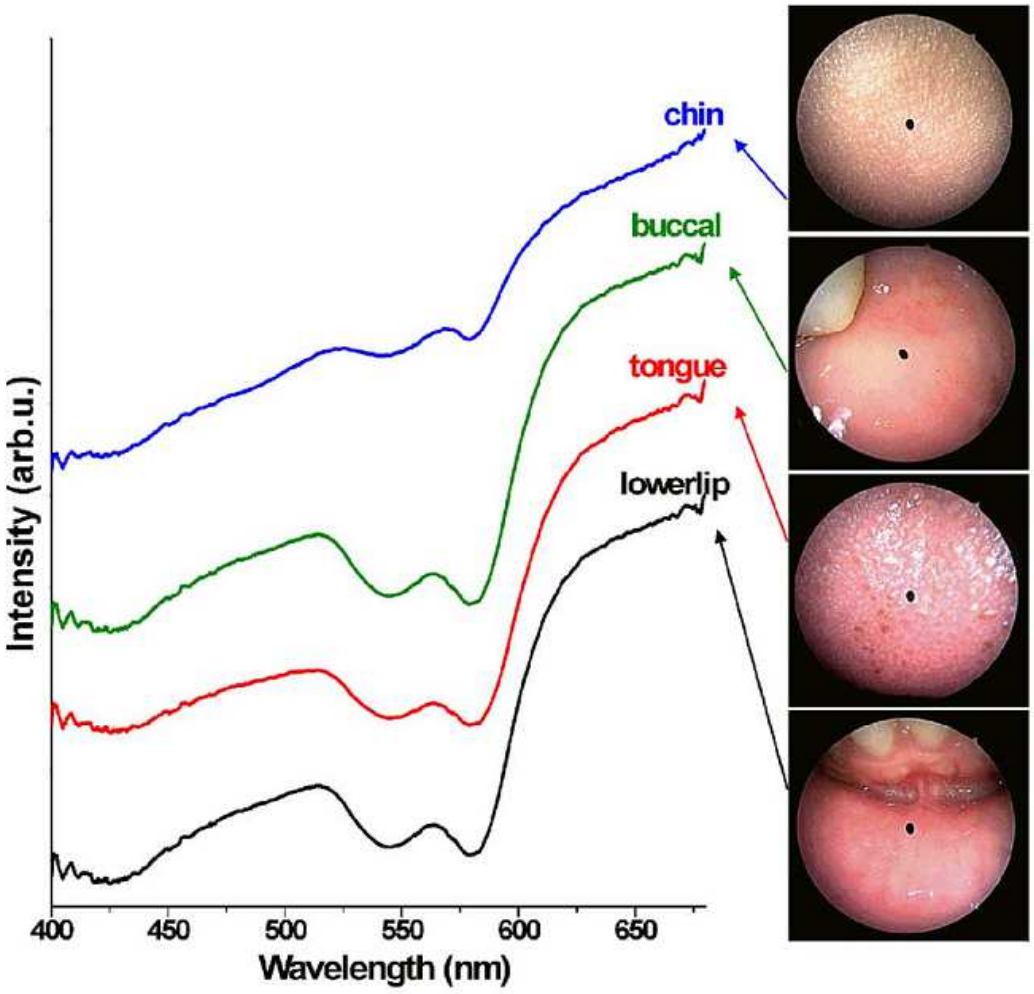

Fig. 3.2 *In vivo* white-light images and the corresponding diffuse reflectance (DR) spectra from different anatomical locations (chin, buccal mucosa, dorsal of the tongue, and lower lip) simultaneously acquired from a healthy volunteer.

By swapping the excitation filter in the xenon lamp to the blue BP filter (375-440 nm) for tissue fluorescence excitation, *in vivo* tissue AF images and point-wise AF spectra can also be simultaneously acquired from the head and neck. Figure 3.3 shows the representative *in vivo* AF images and AF spectra of different locations in the oral cavity from a healthy volunteer. Obviously, AF images (Fig. 3.3) that contain the information about endogenous fluorophores distributions in tissue provide a higher image contrast as compared to WLR images (Fig. 3.2). High quality *in vivo*

tissue AF spectra can be acquired within 0.1 s from the dark spot areas on the AF images (Fig. 3.3).

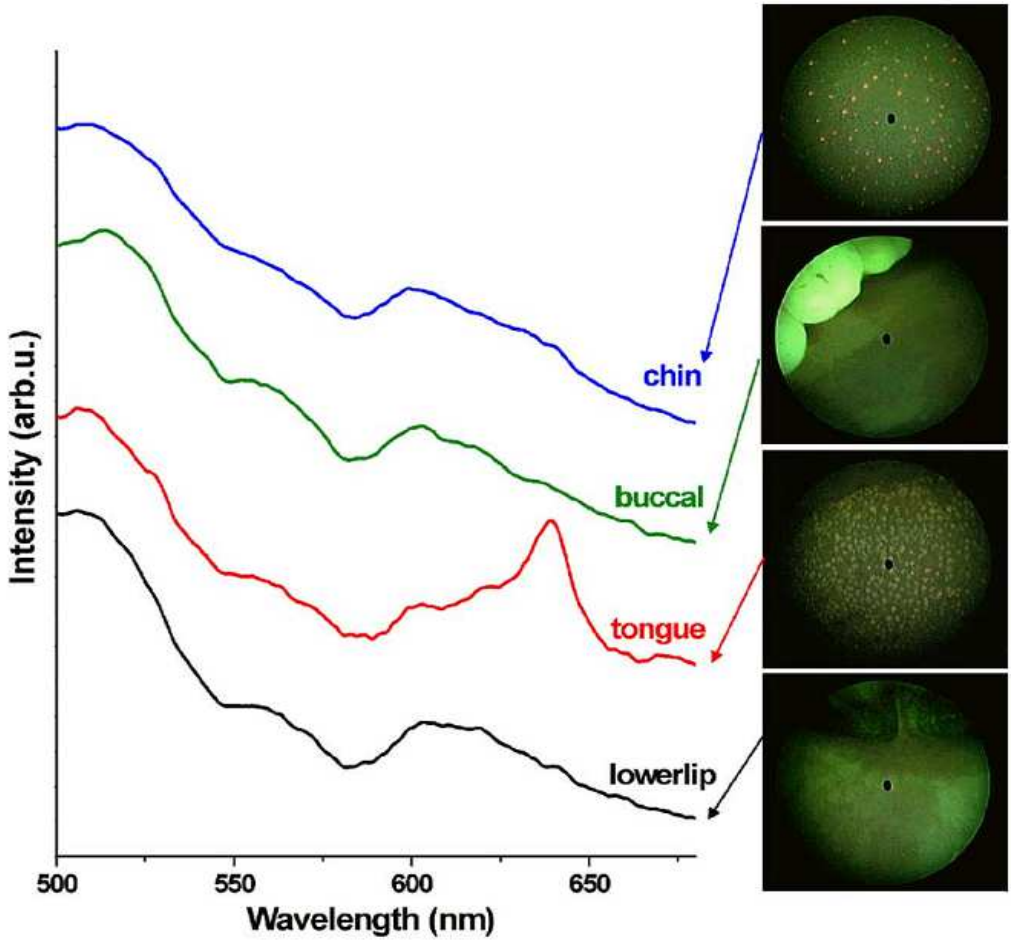

Fig. 3.3 Comparison of *in vivo* AF images and the corresponding point-wise AF spectra from different anatomical locations (chin, buccal mucosa, dorsal of the tongue, and lower lip) simultaneously acquired from a healthy volunteer. Note that each DR spectrum is acquired within 10 ms, whereas the AF spectrum is acquired within 0.1 s.

Again, AF spectra from different anatomical tissue locations also vary, revealing the differences in concentrations of endogenous fluorophores among different tissue locations. For instance, the prominent fluorescence peak at 535 nm for flavins is observed in all different tissues, but a much stronger fluorescence at 630 nm for protoporphyrins is found, particularly in the chin and the tongue.

Fig 3.4 shows that *in vivo* AF spectral differences of different spots on the same tissue imaged (cheek) can be clearly identified due to different spectral shape.

Furthermore, different fluorescent intensity distributions (e.g., fluorescence peak at 535 nm for flavins, fluorescence peak at 630 nm for protoporphyrins) across different spots along the lines on the same tissue imaged can also be observed (Fig. 3.5) within 1 s, indicating the feasibility of our technique developed for revealing the inhomogeneity of endogenous fluorophores distributions in the same tissue.

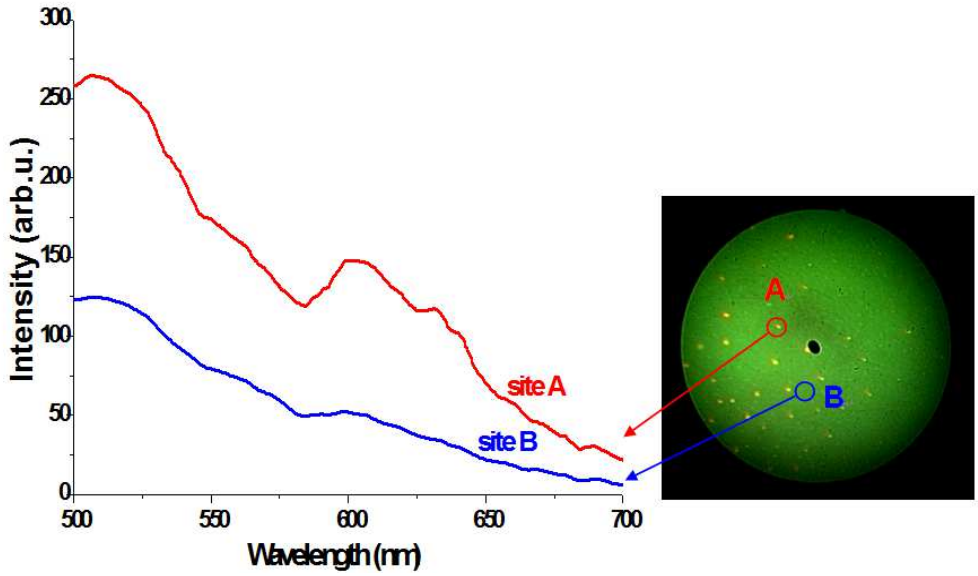

Fig. 3.4 Comparison of in vivo AF spectra of different sites of the cheek on the AF endoscopic image simultaneously acquired from a healthy volunteer.

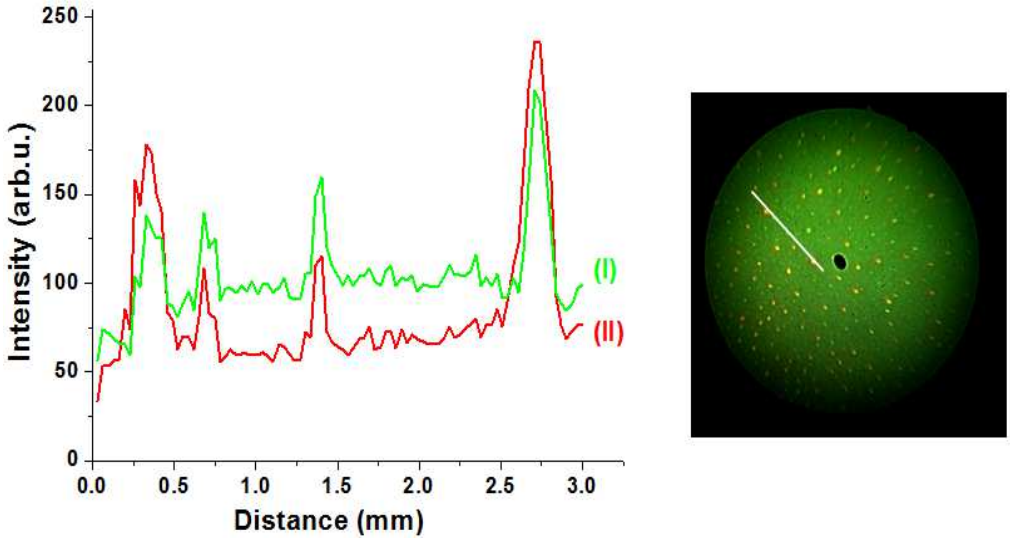

Fig. 3.5 AF intensity profiles along the line indicated on the autofluorescence image acquired from the cheek: (I) Distribution of the endogenous fluorophore-flavins (autofluorescence peaking at 535 nm). (II) Distribution of the endogenous fluorophore–protoporphyrin (autofluorescence peaking at 630 nm).

3.3 Endoscopy based AF/DR Spectroscopy for Laryngeal Cancer Diagnosis

3.3.1 Subjects and tissue preparation

All patients preoperatively signed an informed consent permitting the investigative use of the tissue and this study was approved by the Institutional Review Board (IRB) of the National Healthcare Group (NHG) of Singapore. In this work, a total of 33 pair (i.e., normal and cancer) tissue specimens were collected from 30 patients with a mean age of 65 who underwent surgical resection through laryngoscopy clinics. Immediately after surgical resections, the tissue specimens were immersed in physiological saline solution and sent to the Laboratory for AF/DR imaging measurements. The paired tissue specimens from each patient were placed on a high quality quartz glass slide (25 × 75 × 1.2 mm3) for the spectral measurements.

For each piece of tissue specimen, random sites (2-5) were selected for spectral measurements, and 3-5 measurements were performed on each site. Both AF/DR spectra were directly acquired from the suspicious lesion sites for each patient under endoscopic imaging guidance in less than 1 s. As a result, a total of 446 AF/DR pair spectra (207 normal, 239 cancers) from different tissue sites were collected. After the imaging and spectral acquisitions, the tissue specimens were fixed in 10% formalin solution and then submitted back to the hospital for histopathological examinations. For the assessment of diagnostic sensitivity and specificity of this combined AF/DR spectroscopy for normal and cancer tissue classification, the histopathological results were regarded as the gold standard. The histopathogical examinations confirmed that 33 tissue specimens were normal, and 33 tissue specimens were cancer (moderately differentiated adenocarcinoma).

3.3.2 Combine AF/DR spectra for improving cancer diagnosis

Generally, DR spectroscopy measures the properties of tissue scattering and absorption, which depict the morphological and biochemical information of the tissue epithelial layer. While AF spectroscopy provides the bio-information about endogenous fluorophores in tissue excited with illumination (e.g., UV-VIS light). However, AF spectra obtained from tissue are distorted by tissue absorption and scattering that may lead to the limited accuracy of tissue characterization. In our work, AF spectra were used in conjunction with DR spectra from the same specific anatomical locations to evaluate the capability of increasing the efficiency of cancer diagnostic via extracting the intrinsic (undistorted) fluorescence (IF), in such a way that the effect of the dips which appear around 540 and 580 nm in autofluorescence spectra will be as small as possible. Several modeling approaches have been developed to extract IF spectra of the tissue [180-184]. In our case, extracting from the paired AF and DR spectra obtained, the IF spectra were calculated based on the equation as below [95]:

$$F_i(\lambda) = \frac{F_r(\lambda)}{R_d(\lambda)^{k(\lambda)}}$$

$F_i(\lambda)$: Intrinsic Fluorescence (IF) emission spectra of endogenous fluorophores

$F_r(\lambda)$: Bulk autofluorescence spectra (measurements)

$R_d(\lambda)$: Diffuse reflectance spectra (measurements)

Note that the k(λ) is a scaling factor which denotes the ratio between the path-lengths for AF and DR light, which is independent of wavelength [95]. Several complicated methods were reported in literature [185-187], but we determine the variable power k based on the simple way that the blood absorption dips that appear around 540 and 580 nm in the corrected autofluorescence spectra were as small as

possible [95], which is 1.5 in our work. Prior to data-analysis, the raw spectra (AF/DR) were firstly smoothed using the adjacent-five-point averaging method. The background-subtracted AF, DR and IF spectra were both normalized to minimize the effect of the instrument handling variations during clinical measurements with respect to different subjects and tissue sites. All processed spectra were assembled into three matrixes, and the mean centering of the entire dataset was then performed. PCA-LDA algorithm with leave-one-subject-out cross validation method was then used to reduce the dimension of the spectral data and highlight the similarities and differences within the data set for tissue characterization. Each variable in the data set is expressed as a principal component (PC). Accordingly, loadings on the PCs represent orthogonal basis spectra of the most prominent spectral variation in the dataset accounting for progressively decreasing variance, whereas the scores on the PCs represent the projection value of the tissue spectra on the corresponding loading. Thus, PCA can efficiently be used to resolve spectral variations while reducing the dimension of the dataset to a minimum. The significant PCs chosen to retain for further discriminant analysis is based on Student's t-test ($p<0.05$). All these multivariate statistical analysis was automatically performed via developed programs in the Matlab (Mathworks Inc., Natick, MA) environment.

3.3.3 Results and discussion

Figure 3.6 shows the representative examples of AF/WRL images (lower is cancer, top is normal) of laryngeal tissue specimens under blue light (375-440 nm) and white light (400-700 nm) illumination, respectively. In the AF images (Fig. 3.6a), the normal's intensity (top bright area surrounding the dark spot) is approximately 1.2~2 times compared to the cancer (lower area in the AF/WLR images) while the intensity ratio of normal to tumor in WLR image (Fig. 3.6b) is ~1.0. Therefore, AF

image contrast between normal and cancer is much better than that WLR imaging.

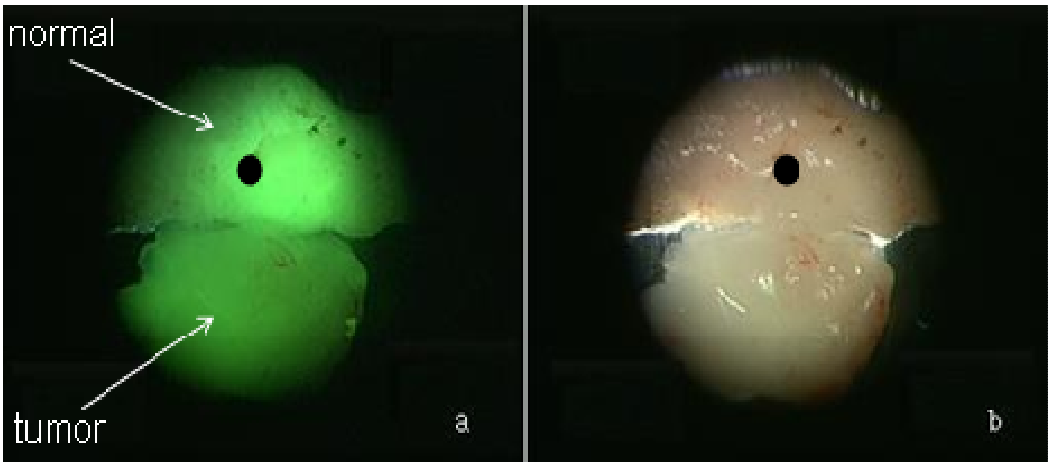

Fig. 3.6 Representative examples of (a) AF images and (b) WLR images of laryngeal tissue specimens (upper normal, lower tumor) using blue light/white light as excitation.

The comparison of mean spectra (AF/DR/IF) ±1 SD of normal (207) and tumor (239) laryngeal specimens are shown in left of Figure 3.7a, 3.7c and 3.7e, respectively. The plots in Figure 3.7b, 3.7d and 3.7f refer to the comparison of normalized mean spectra (AF/DR/IF) of normal and tumor tissues, respectively. Clearly, the normal tissue has higher intensity than the tumor in AF/IF spectra (Fig. 3.7a, 3.7b). Besides the peak intensity, another feature is that the emission peak of the tumor tissue is slightly shifted towards the red region. One more feature that needs to be highlighted is that the tumor tissues have higher emission intensity after wavelength around 560nm (Fig. 3.7b). In DR spectra (Fig. 3.7c, 3.7d), most curves showed significant dips around 540 and 580 nm due to the oxygenated hemoglobin absorption. The Figure 3.7e is the mean IF spectra of normal tissues and tumor tissues after combination. The peak shift of the tumor tissues to the red region is more apparent. Similarly, the intensity of tumor tissues IF spectra in the region more than 560 nm is higher than that of the normal tissues (Fig 3.7f) where as in the region 500-560 nm, normal is higher, and what is more, it shows more significant intensity increase than those in Fig. 3.7b.

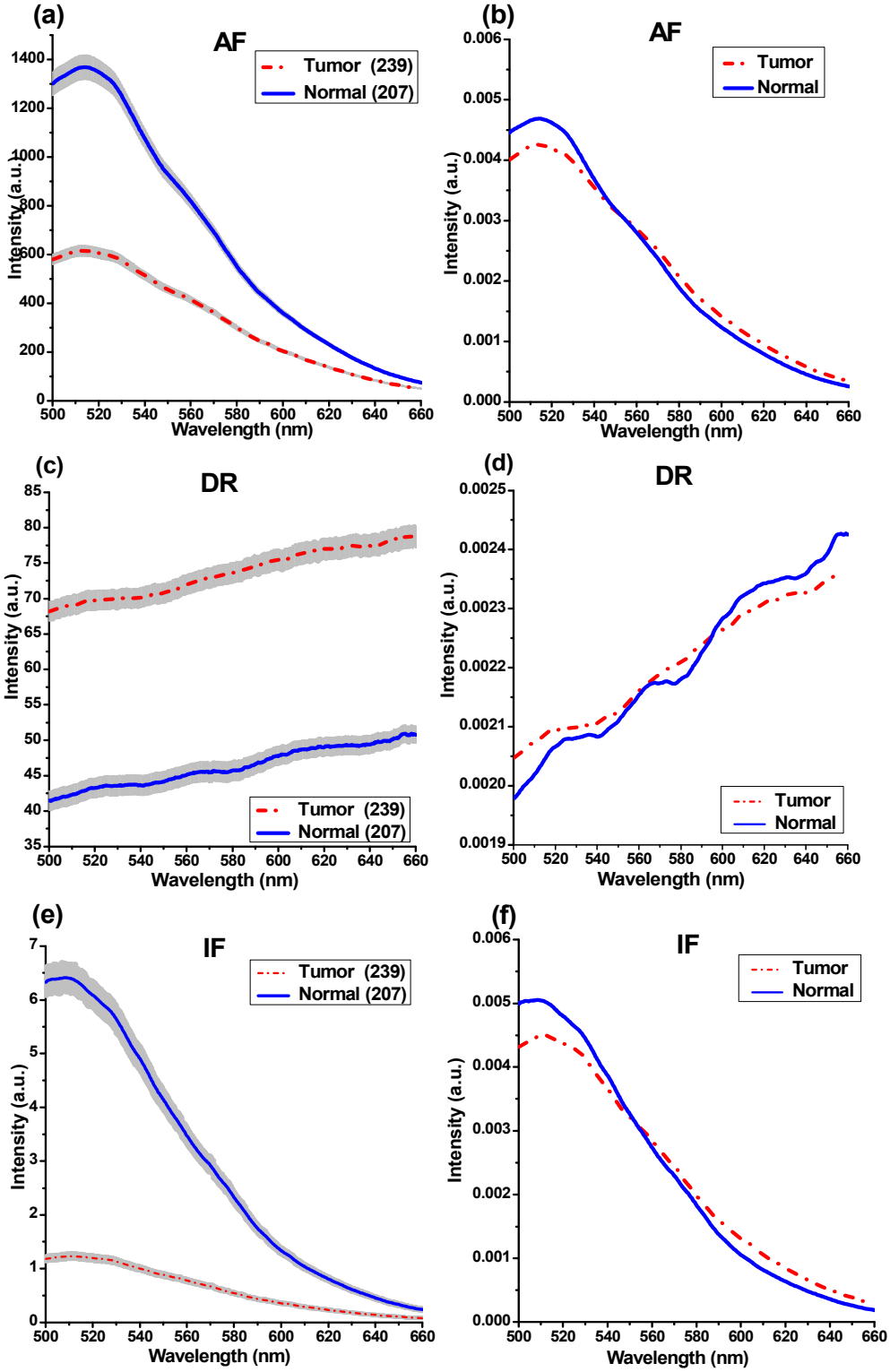

Fig. 3.7 Comparison of mean spectra ±1 standard deviations (SD) and normalized spectra of normal (n=207) and tumor (n=239) laryngeal tissues. (a) mean AF spectra ±1 SD; (b) normalized AF spectra; (c) mean DR spectra ±1 SD; (d) normalized DR spectra; (e) mean IF spectra ±1 SD; (f) normalized IF spectra; The shaded area represents the respective standard deviations.

To compare the tissue diagnostic performance of different spectroscopic techniques, PCA-LDA multivariate algorithm was applied to evaluate the elusive differences observed in the spectra of different tissue types. The normalized AF, DR and combined AF/DR (IF) spectral datasets were first mean centered to eliminate common variance and ensures the principal components (PCs) form an orthogonal basis [188, 189]. The leave-one-site-out cross-validated PCA-LDA diagnostic models were further developed for AF, DR and combined AF/DR spectral datasets using three dominant PCs which are shown in Figure 3.8, accounting for 85.1% (PC1), 1.41% (PC3) and 0.62% (PC4) of AF spectral variations, 97.4% (PC1), 0.66% (PC3) and 0.13% (PC4) of DR spectral variations as well as 92.5% (PC1) 0.60% (PC3) and 0.04% (PC7) of IF spectral variations, respectively. Noted that the features of different significant PCs are distinct, but some PC features roughly correspond to spectral characteristic, such as (e.g., oxy- and deoxy-hemoglobin absorption near 540 nm and 580 nm) similar to those of tissue AF/DR spectra. The first significant PC accounts for the largest variance within the spectral data sets (e.g., 85.1%, 97.4% and 92.5%), whereas successive PCs describe features that contribute progressively smaller variances. Paired two-sided Student's t-tests on the first several PCs of different spectral dataset (AF/DR/IF) show that only three PCs ($p<0.005$) are diagnostically significant, respectively. The diagnostically significant PCs are then fed into the LDA model together with leave-one site-out, cross-validation technique for tissue classification. Figure 3.9 shows the prediction results (posterior probabilities) between normal and cancer pathologies as calculated for (a) AF, (b) DR and (c) combined AF/DR (IF) datasets, respectively.

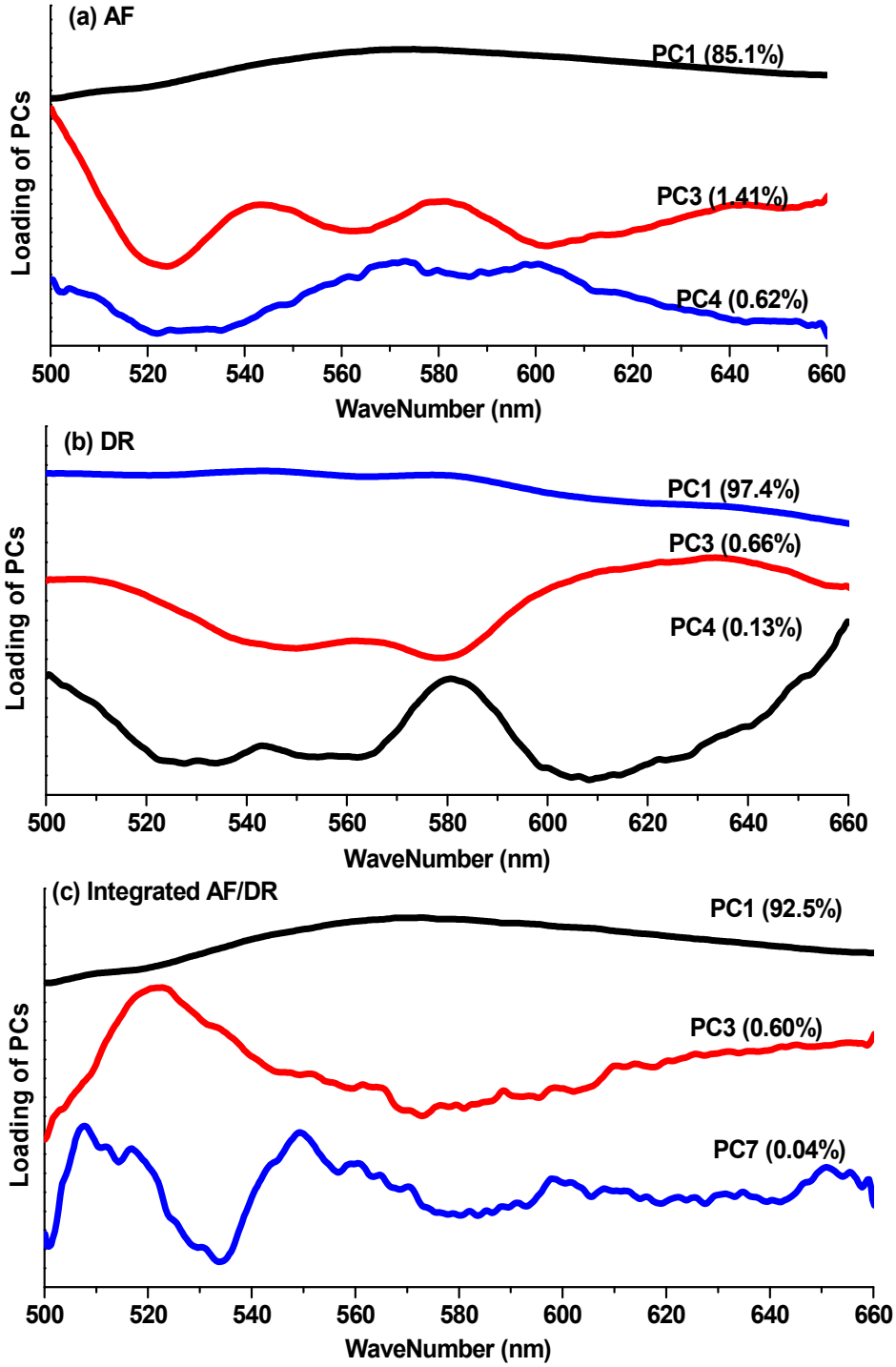

Fig. 3.8 The three significant principal components (PCs) accounting for more than 90% of the total variance calculated from AF/DR/IF spectra of laryngeal tissue. The significant PCs loadings of (a) AF spectra (PC1: 85.1%; PC3: 1.41%; PC4: 0.62%), (b) DR spectra (PC1: 97.4%; PC3: 0.66%, PC4: 0.13%) and (c) IF spectra (PC1:92.5%, PC3: 0.60%, PC7: 0.04%)) is shown respectively. Note that the PCs loading curves was shifted vertically for better visualization.

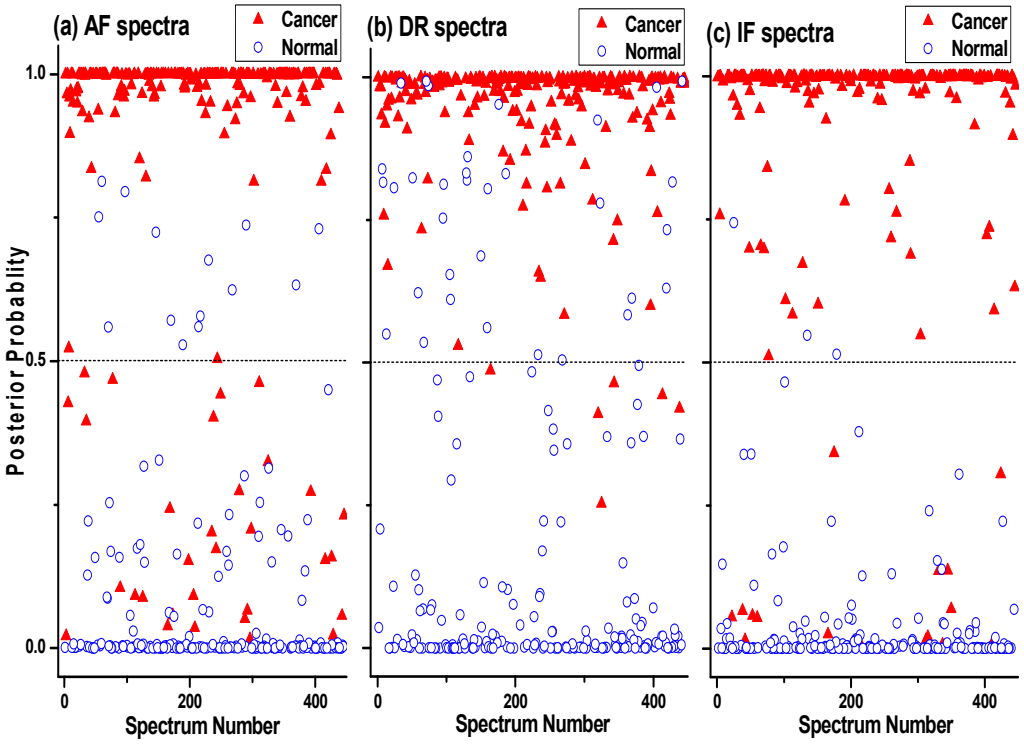

Fig. 3.9 Scatter plot of the posterior probability values belonging to the normal and cancerous tissue categories calculated from (a) AF, (b) DR and (c) combined AF/DR spectra, respectively, using the PCA-LDA technique together with leave-one-site-out, cross-validation method. The dashed line gives the sensitivities of 87.0% (208/239), 97.5% (233/239), and 91.6% (219/239); specificities of 93.2% (193/207), 84.1% (174/207), and 98.6% (204/207), respectively, for discriminating cancer from the normal laryngeal tissues.

The threshold line (0.5) in the posterior probability scatter plot (Table 3.1) yielded diagnostic accuracies of 89.9% (401/446), 91.3% (407/446) and 94.8% (423/446) (sensitivities of 87.0% (208/239), 97.5% (233/239), 91.6% (219/239) and specificities of 93.2% (193/207), 84.1% (174/207), 98.6% (204/207)) as shown in Table 3.1, respectively, suggesting that combined AF/DR spectroscopy is a more powerful tool for laryngeal cancer diagnosis.

Table 3.1 Comparison of diagnostic performance of different spectral techniques (AF, DR and the combined AF/DR) for discrimination of cancer from normal laryngeal tissue.

Spectra dataset	**Sensitivity**	**Specificity**	**Accuracy**
AF spectra	87.0% (208/239)	93.2% (193/207)	89.9% (401/446)
DR spectra	**97.5% (233/239)**	84.1% (174/207)	91.3% (407/446)
IF spectra	91.6% (219/239)	**98.6% (204/207)**	**94.8% (423/446)**

Furthermore, the ROC curves (Figure 3.10) were also generated from the posterior probability plot in Fig. 3.9 at different threshold levels to determine the probability of predictions either being cancer or normal for all tissue data. The integration areas under the curves (AUC) were 0.979, 0.978 and 0.982 for AF, DR and combined AF/DR spectroscopy, respectively, further confirming the greater efficacy of the integrated point-wise AF/DR spectroscopy coupled with PCA-LDA multivariate diagnosis algorithms for laryngeal cancer classification as compared to AF or DR spectroscopy alone.

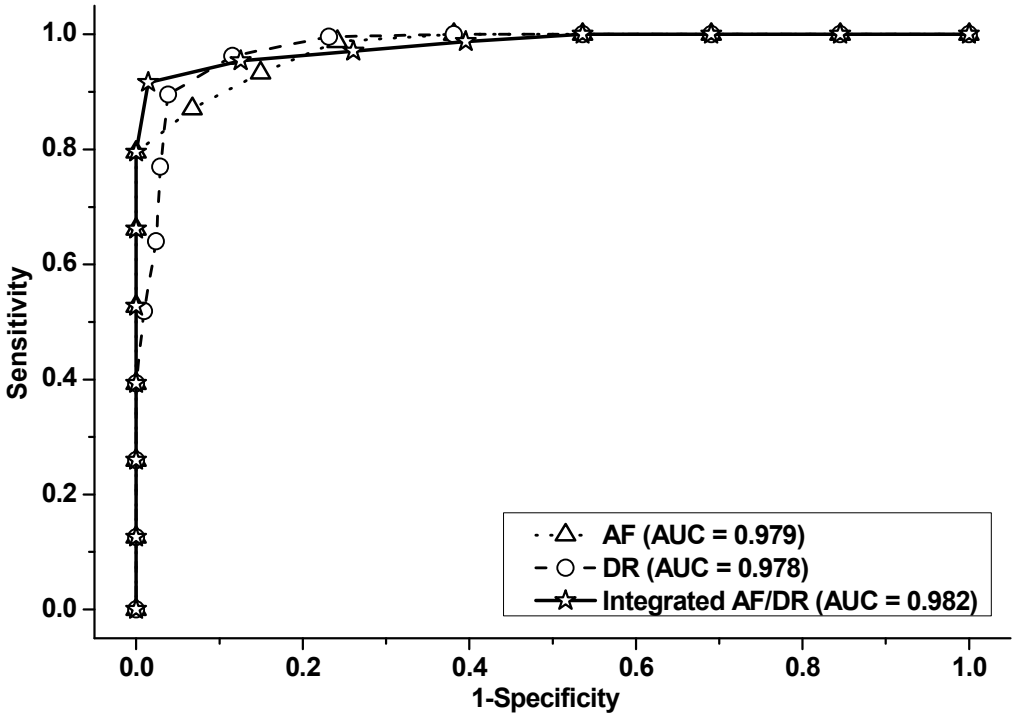

Fig. 3.10 Receiver operating characteristic (ROC) curves of discrimination results for AF, DR and combined AF/DR spectra, respectively, for cancer tissue classification through the use of point-wise AF/DR spectroscopy and PCA-LDA diagnostic algorithms. The integrated area under curves (AUC) are 0.979, 0.978 and 0.982 for the AF, DR and combined AF/DR spectra, respectively, illustrating the best performance of integrated point-wise AF/DR spectroscopy for laryngeal cancer diagnosis.

The results in this study are shown that our developed point-wise AF/DR spectroscopy has great potential as a powerful clinical tool for *in vivo* laryngeal cancer diagnosis. In AF spectroscopy, the lower intensity of tumor tissues in

comparison to normal tissues is similar to the results from early literature [113, 190, 191]. The flavins (e.g., riboflavin, flavin mononucleotide (FMN), flavin adenine dinucleotide (FAD)) are the major fluorophore in the laryngeal cancer diagnosis, the decrease in concentration of flavin in tumor tissues is the major contributor to this observation of lower intensity. As is well-known, the emission peak of flavins occurs at the region of 480-540 nm under the excitation of ultra violet (UV) or blue light [192, 193]. In addition to the decrease in flavins concentration, the flavins may be present in its reduced form which has less fluorescence than oxidized flavin in healthy tissues [190]. The presence of a disease may alter the scattering and absorption properties of the tissue, due to changes in blood concentration, nuclear size distribution, epithelial thickness and collagen content in the tissues. Mucosal thickening or replacement of the sub-mucosa by tumor cells may also lead to a decrease in the fluorescence emission of the sub-mucosa flavins and other fluorophores such as collagen. Tumor tissues have higher emission after 560 nm which may be contributed to flavins whose emission peak occurs at 560 nm. This finding of red-shift (Fig. 3.7b and 3.7f) for tumor samples relative to that of normal tissues when a UV/blue light is used as excitation source is consistent with results from Gillenwater et al who was able to differentiate between normal and cancerous mucosa of the oral cavity by using a diagnostic algorithm based on spectra at 337 nm, yielding a sensitivity of 88% and a specificity of 100% [104]. In our work, considering the complexity of biological tissue, we applied PCA-LDA classification algorithms for differentiation between normal and tumor instead of using prominent peak shift, yielding better diagnostic result with accuracy of 94.8% (sensitivity of 91.6%, specificity of 98.6%), further verifying that PCA-LDA combined AF/DR spectra data for analysis is more robust and rigorous to differentiate spectra of either

normal or cancer tissues.

Currently, we are conducting an *in vivo* clinical measurement on a large size of head and neck patients to further evaluate the clinical merits of the integrated AF/DR spectroscopy techniques for improving early head and neck cancer detection at endoscopy.

3.4 Conclusion

In conclusion, we have developed an integrated autofluorescence endoscopic imaging and point-wise spectroscopy system and evaluated the performance of *in vivo* measurement in the head and neck. The simultaneous acquisition of endoscopic AF image and AF/DR spectrum from a specific area of imaged tissue *in vivo* can be realized within 0.1 s, which may facilitate the rapid, non-invasive, *in vivo* tissue diagnosis and characterization in clinical settings. We have also assessed the diagnostic capability of integrated AF endoscopic imaging system and point-wise AF/DR spectroscopy together with PCA-LDA modeling for normal and cancer *in vitro* tissue classification in the head and neck with good diagnostic accuracy, which is superior to either the AF or DR spectroscopy alone. The unique AF image-guided point-wise spectroscopy technique developed in this work also can be readily adapted to study other internal organs *in vivo* by using different flexible medical endoscopes (e.g., bronchoscope, colonoscope, gastroscope, etc.).

Chapter 4 Endoscope-based Fiber-optic Raman Spectroscopy for Characterizing Raman Properties of Human Tissue in the Head and Neck

In this chapter, we report for the first time an integrated Raman spectroscopy and trimodal (white-light reflectance, autofluorescence and narrow band) imaging technique developed for real-time *in vivo* tissue Raman measurements at endoscopy. A special miniaturized Raman probe (diameter < 2mm) with filtering modules is developed permitting effective elimination of interference of fluorescence background and silica Raman in fibers while maximizing Raman collections from the tissue. High quality *in vivo* Raman spectra of oral cavity can be acquired within 1s under immediate guidance of different wide-field imaging modalities, greatly facilitating the adoption of Raman spectroscopy into clinical research and practice during routine endoscopic inspections.

Afterwards, we have implemented this transnasal image-guided Raman endoscopy to assess Raman spectral properties of nasopharyngeal and laryngeal tissue *in vivo* during clinical endoscopic examinations, realizing rapid, real-time and *in vivo* Raman measurements of different anatomical locations in the head and neck. A total of 874 high-quality *in vivo* Raman spectra were successfully acquired from different anatomic locations of the nasopharynx and larynx (i.e., posterior nasopharynx (PN) (n=521), the fossa of Rosenmüller (FOR) (n=157) and true laryngeal vocal chords (LVC) (n=196)) in 23 normal subjects at transnasal endoscopy. Difference spectra and principal component analysis (PCA) were employed for tissue characterization, enlightening the tissue variability at the biomolecular level. The PCA-linear discriminant analysis (LDA) provides sensitivity of 77.0% and specificity of 89.2%

for differentiation between PN vs. FOR, and sensitivity of 67.3% and specificity of 76.0% for distinguishing LVC vs. PN using the leave-one subject-out cross validation.

This work demonstrates for the first time that transnasal image-guided Raman endoscopy can be used to acquire *in vivo* Raman spectra from the nasopharynx and larynx in real-time. Significant Raman spectral differences ($p<0.05$) identified reflecting the distinct composition and morphology in the nasopharynx and larynx should be considered as an important parameter in the interpretation and rendering of diagnostic decision algorithms for *in vivo* tissue diagnosis and characterization in the head and neck.

4.1 Introduction

In the past decade, autofluorescence imaging (AFI) technique which is able to detect the changes of endogenous fluorophores and morphologic architectures of tissue has been developed to significantly improve the detection sensitivity of early neoplastic lesions in the epithelium at endoscopy [173]. Very recently, narrow band imaging (NBI) technique which is able to enhance visualization of the mucosal glandular and vascular pattern changes beneath the tissue surface has shown great promise for improving *in vivo* histologic diagnosis of intraepithelial neoplastic lesions [194-198]. Although AF and NBI imaging techniques provide high detection sensitivities, these wide-field endoscopic imaging modalities suffer from moderate diagnostic specificities owing to their lack of ability revealing biomolecular information about the tissue. Raman spectroscopy is a unique vibrational probe that is capable of providing specific fingerprints of biochemical and biomolecular structures and compositions of tissue, and has been excelled in the early detection of precancer and cancer with high diagnostic specificity [199-202]. Hence, it is highly desirable to incorporate Raman point measurements into endoscopic imaging system for direct

biochemical and biomolecular assessments of suspicious spots in real-time. However, Raman clinical endoscopic applications have been limited not only by the difficulty in capturing inherently weak tissue Raman signals [199, 201], but also by the relatively slow speed of spectral acquisition [201]. The miniaturization of flexible Raman probes that can fit into the instrument channel of conventional endoscopes for effective collections of tissue Raman scattering renders another challenge in clinical settings [201, 203-205].

4.2 Integrated Raman Spectroscopy at Endoscopy

In this section, an integrated rapid Raman spectroscopy and trimodal imaging (WLR/AFI/NBI) techniques was developed for realizing real-time *in vivo* tissue Raman measurements at endoscopy. Successful incorporation of the endoscopic Raman spectroscopy for probing biomolecular fingerprints into the endoscopic trimodal imaging for providing tissue morphology structures and vascular patterns will increase the diagnostic value and ultimately improve the effectiveness of surveillance of histopathological status of internal organs.

4.2.1 Integrated Raman spectroscopy and endoscopic imaging system

Figure 4.1 shows the schematic of the integrated Raman spectroscopy and trimodal wide-field imaging system developed for *in vivo* tissue measurements at endoscopy. The Raman spectroscopy system consists of a spectrum stabilized 785 nm diode laser (maximum output: 300 mW, B&W TEK Inc., Newark, DE), a transmissive imaging spectrograph (Holospec f/1.8, Kaiser Optical Systems), a liquid nitrogen-cooled, near-infrared (NIR)-optimized, back-illuminated and deep depletion CCD camera (1340×400 pixels at 20×20 μm per pixel; Spec-10: 400BR/LN, Princeton

Instruments), and a specially designed Raman endoscopic probe for both laser light delivery and *in vivo* tissue Raman signals collection.

We have also developed a Matlab-based software for Raman data acquisition and analysis (including liquid nitrogen-cooled CCD dark-noise subtraction, laser On/Off control, wavelength calibration, system spectral response calibration, signal saturation detection, cosmic ray rejection, tissue autofluorescence background subtraction (5th-order polynomial fit), Raman curve adjacent averaging smoothing, etc.), as well as real-time display of *in vivo* tissue Raman spectra during clinical endoscopic measurements. The trimodal endoscopy imaging system primarily comprises a 300 W short-arc xenon light source, a videoscope (GIF-FQ260Z, Olympus), and a video system processor (CV-260SL, Olympus). The dedicated xenon light source coupled with different sets of filters (WLR (red-green-blue (RGB) filters: red filter: 585-655 nm, green filter: 500-575 nm, and blue filer: 390-495 nm); AFI (blue filter of 390-470 nm and green filter of 540-560 nm for reflectance image normalization), and NBI (narrowband filters: green filter of 530-550 nm and blue filter of 390-445 nm) provides different illumination light for trimodal endoscopic imaging (WLR/AFI/NBI). The light reflected or fluorescence emitted from tissue are detected by two monochrome CCD chips mounted behind the two objective lens placed next to each other at the distal tip of the videoscope: one CCD for WLR/NBI and the other one for AFI. The video system processor will then convert the signal received from the CCD in the endoscope into RGB video image for display on a video monitor.

Hence, trimodal wide-field endoscopic images (WLR/AFI/NBI) and the corresponding real-time *in vivo* processed Raman spectra of the tissue imaged can be simultaneously displayed and recorded in the video system processor and the personal

computer (PC), respectively.

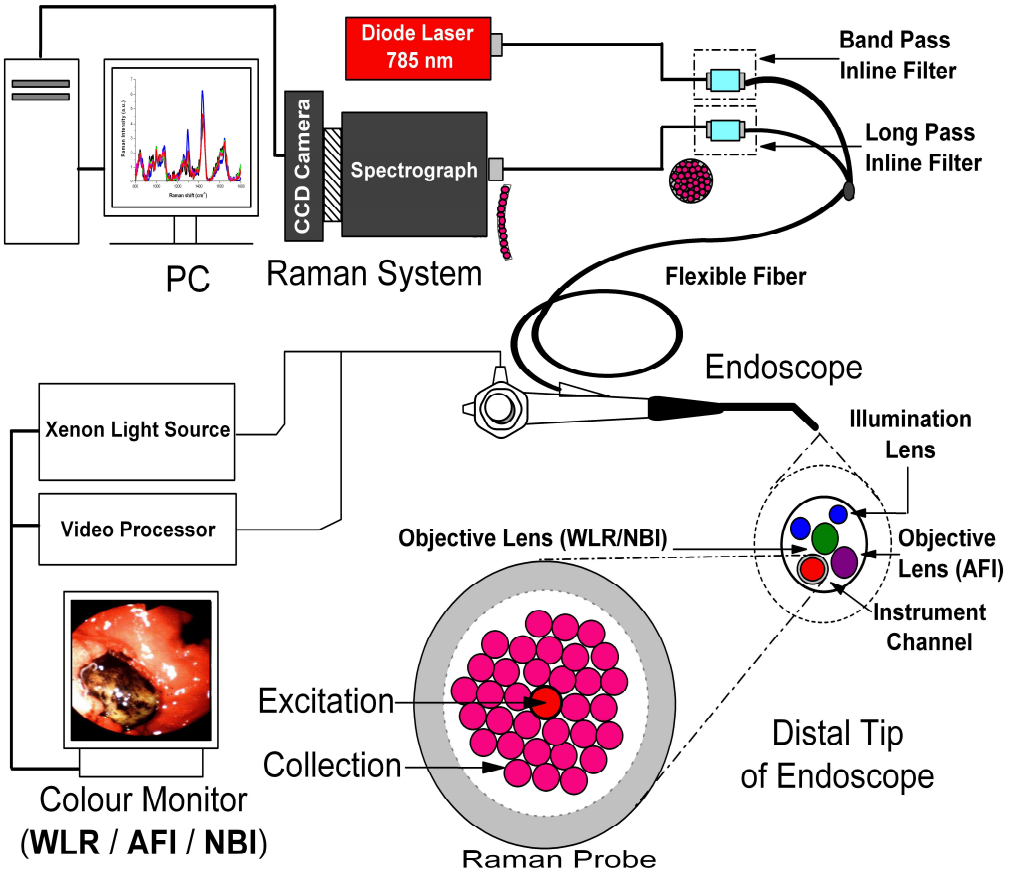

Fig. 4.1 Schematic of the integrated Raman spectroscopy and trimodal endoscopic imaging system for *in vivo* tissue Raman measurements at endoscopy. WLR, white light reflectance imaging; AFI, autofluorescence imaging; NBI, narrow band imaging.

4.2.2 Endoscope-based fiber optics Raman probe

For clinical Raman endoscopic applications, we have developed a bifurcated fiber-optic Raman probe with a 1.8 mm outer diameter tip and 2.5 m in length, consisting of 33 ultralow OH fibers: a 200 μm central fiber for laser delivery and 32 200 μm surrounding fibers for Raman collections (Fig. 4.1). A hypo tubing (diameter of 0.46 mm) is used to separate the excitation fiber from the surrounding collection fibers to avoid photon cross-talk. The novel micro-coating technique is applied to the distal end of the Raman probe by coating a narrow band pass filter (centered at 785 nm, transmission of >90%, FWHM= ± 2.5 nm) onto the central excitation fiber

whereas the edge long pass filters (cut off at 800 nm, transmission of over 90% in 800-1200 nm) are coated onto the collection fibers. The band pass filter reduces most of the fuse-silica noise generated in the excitation fiber of the Raman probe before the excitation beam hits the tissue, and the edge long pass filters of the collection fibers reinforce the reflected excitation light to be blocked yet allowing the scattered tissue Raman signal to pass back to the detector. At the proximal ends of the Raman probe, the excitation and emission fibers were separated and coupled into two in-line filter modules: one integrated with a narrow band pass filter (LL01-785, Semrock Inc.,) for suppressing laser noise, fluorescence, and Raman emissions from a 200 μm core diameter fiber that connects the 785 nm laser excitation power of ~1.5 W/cm^2 to the in-line filter end for tissue excitation; one integrated with an edge long pass filter (LP02-785RU, Semrock Inc.,) for further reducing the scattered laser light while permitting the scattered Raman signals to pass through towards the Raman spectrograph.

Moreover, to maximize Raman signal detection while correcting the image aberration of the spectrograph for improving the spectral resolution of the endoscopic Raman system, we have also designed a special round-to-parabolic fiber bundle to relay the collected tissue Raman emission onto the spectrometer [204]. This bundle comprises 64 100 μm core diameter fibers packed in a round geometry at the collection in-line filtering module end, but spread out into a parabolic linear array at the spectrometer entrance end that is aligned in an orientation opposite to the image aberration of the transmissive spectrograph. This unique design effectively corrects spectrograph image aberrations (images not shown), thereby enabling the hardware binning of the entire CCD chip to be implemented by increasing the signal-to-noise ratio (SNR) up to 20-fold (400/√400) compared with complete software binning [204].

The spectral resolution of our Raman system is approximately 9 cm^{-1} (a 100 μm core diameter fiber covers 6 pixels with a 1.25 magnification of the spectrograph; each pixel covers 1.5 cm^{-1}). Despite having a 5 mm long rigid tip, our Raman probe with a 1.8 mm outer diameter tip passes easily through the instrument channel of most conventional medical endoscopes.

As a result, the image-aberration corrected, high SNR Raman spectrometer system coupled with the endoscopic Raman probe with minimization of the fluorescence background and silica Raman signals in the fibers permits reliable *in vivo* tissue Raman measurements during clinical endoscopy. To ensure that tissue Raman endoscopic measurements can be performed in real-time under the guidance of trimodal wide-field endoscopic imaging modalities, an additional customized long pass filter (cut off at 800 nm with OD>6 for 400-500 nm) is also incorporated into the in-line filter coupled with the 785 nm edge long pass filter to effectively eliminate the second order spectra interference generated from the blue excitation light (390-490 nm) of the trimodal wide-field imaging.

4.2.3 Evaluation of *in vivo* tissue Raman measurement in the oral cavity

Figure 4.2 shows *in vivo* Raman spectra of buccal mucosa acquired from a healthy volunteer using acquisition times of 0.1, 0.5 and 1.0 s, respectively. The prominent vibrational features of buccal mucosa, such as the ν(C=O) amide I band at 1655 cm^{-1}, the $\delta(CH_3)$ and δ (CH_2) scissoring modes at 1445 cm^{-1}, the CH_2 deformation at 1302 cm^{-1}, the ν(CN) and δ(NH) amide III bands at 1265 cm^{-1}, the ν(CC) or ν(CO) of phospholipids at 1078 cm^{-1}, the *ν*(C-C) ring breathing of phenylalanine at 1004 cm^{-1}, and the ν (CC) of prolines at 855 cm^{-1} [4-7], can be

clearly discerned in all Raman spectra. Some weak tissue Raman peaks (e.g., ν(C=O) of phospholipids at 1745 cm^{-1}) can also be clearly identified even using the exposure time of 0.1 s. Obviously, the signal-to-noise ratio (SNR) of *in vivo* Raman spectra increases with integration times (e.g., SNR of the Raman band at 1445 cm^{-1} are approximately 10 and 32 at 0.1 s and 1.0 s, respectively).

We also measure and characterize the effects of the probe-tissue angles and pressures during *in vivo* Raman measurements on buccal mucosa, no Raman spectral artifacts have been observed due to these variations (data not shown). Hence, high quality and reproducible Raman spectra can be acquired from *in vivo* buccal mucosa within 1.0 s or even sub-seconds using the rapid NIR Raman spectroscopy system coupled with the endoscopic Raman probe, confirming the utility of our Raman endoscopic system on *in vivo* tissue Raman measurements within clinically relevant times.

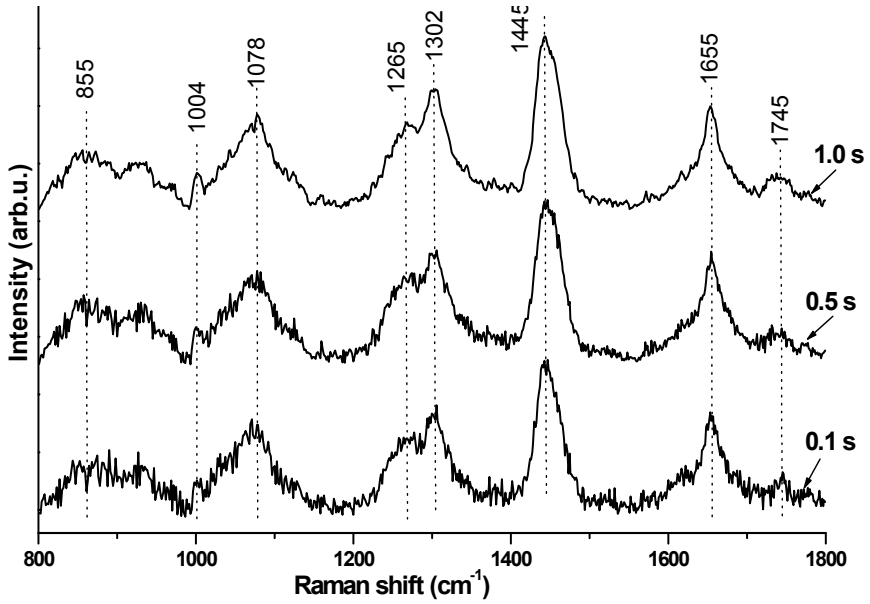

Fig. 4.2 Comparison of *in vivo* Raman spectra of buccal mucosa acquired from a healthy volunteer under different Raman acquisition times (t = 0.1, 0.5 and 1.0 s). Each spectrum is normalized to its own acquisition time.

We also evaluate the viability of *in vivo* tissue Raman spectra measurements conducted simultaneously under different wide-field imaging illumination conditions

(Fig. 4.3). Similar to the Raman spectra obtained without imaging light illumination (Fig. 4.2), high quality *in vivo* Raman spectra of buccal mucosa can also be acquired and the major Raman peaks can be consistently observed. Clearly, the prominent Raman features from *in vivo* tissues are not affected by the concurrently illumination light (i.e., white light for WLR, blue light for AFI and narrow band illumination for NBI) under different endoscopic imaging modalities. This result demonstrates the robustness of our Raman endoscopy system that is able to work simultaneously with different wide-field imaging modalities during routine endoscopic examinations.

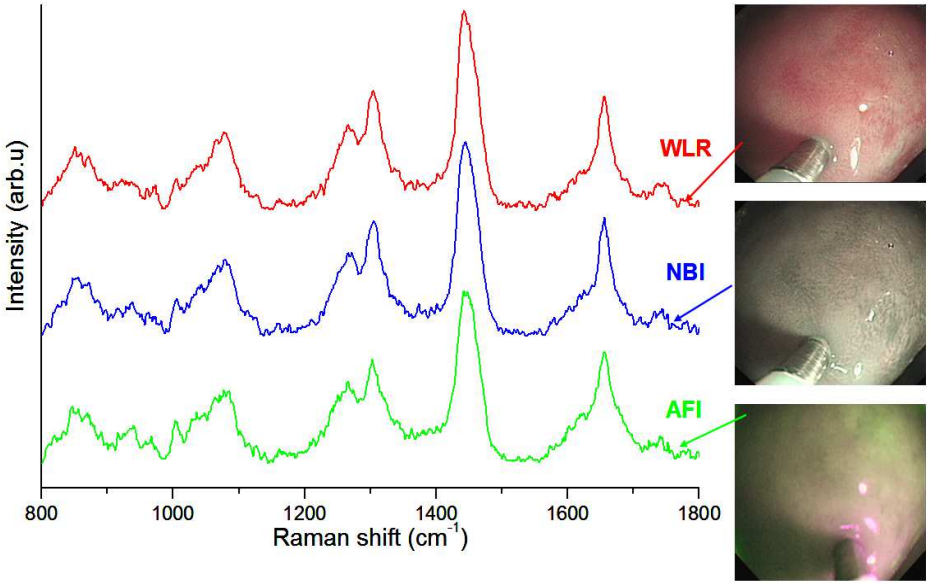

Fig. 4.3 Comparison of *in vivo* Raman spectra of buccal mucosa acquired from a healthy volunteer under three different wide-field imaging (i.e., WLR, NBI, and AFI) illumination conditions. All spectra are normalized to Raman acquisition times of 1.0 s.

4.3 Characterization of Raman Spectral Properties in the Nasopharynx and Larynx *in vivo*

In the previous section, we have elaborate the successful development of a Raman fiber probe (diameter < 2mm) which can pass down the instrument channel of most medical endoscopes, which facilitates us to be able to evaluate the clinical merit of transnasal Raman endoscopy technique for *in vivo* tissue characterization in the

head and neck. Since the compositional and morphological profiles of different organs (i.e., larynx and nasopharynx) in the head and neck are highly functional specialized and exhibit significant variations in anatomical and morphological properties (e.g., lymphoid tissues, vascularity, secretion, cartilage, etc.), there is a fundamental ambiquity to which extent one may account for inter-anatomical variabililty in developing efficient algorithms for *in vivo* nasopharyngeal and laryngeal tissue Raman diagnostics. Therefore, we applied this transnasal image (i.e., WLR and narrowband imaging (NBI))-guided Raman endoscopy to directly evaluate and characterize distinctive Raman spectral properties of nasopharyngeal and laryngeal tissue *in vivo*. Raman spectral differences reflecting the distinct composition and morphology among the nasopharynx and larynx are further evaluated using multivariate techniques (i.e., principal components analysis (PCA) and linear discriminant analysis (LDA)).

4.3.1 Patients and procedure

A total of 23 normal healthy male subjects of different races (twenty-two Asian and one Caucasian) were recruited for *in vivo* tissue Raman measurements at transnasal endoscopy. In these subjects recruited, no suspicious lesions were identified under the WLR and NB imaging endoscopic examination. A total of three primary measurement sites of assumed normal (or benign) tissues were predefined for *in vivo* Raman acquisitions, including the true laryngeal vocal cords (LVC), the posterior nasopharynx (PN), and also the pharyngeal recess (i.e., fossa of Rosenmüller (FOR)) where NPC typically initiates. The fiber-optic Raman probe was performed by the assistant of the endoscopist and carefully placed in gentle contact with internal tissues interrogating with the endogenous biomolecular compositions of tissue in real-time. The accurate positioning against the biopsied tissue sites was verified on the

WLR/NBI monitor by the endoscopist in-charge.

The probe allowed Raman spectra to be collected from a small area (~200 μm in diameter) with probing volume of approximately 1 mm^3 and penetration depth of ~800 μm. Each spectrum was acquired within 0.5 s using the 785 nm laser light with the power of ~50 mW on the tissue surface [206, 207]. The Raman spectra were displayed in real-time on the PC monitor and were immediately stored for post-procedural inspection. This rapid Raman endoscopic technology is non-destructive, and can now routinely be used under endoscopic transnasal examinations for clinical evaluation. To assess the intra-tissue site variance, several Raman spectra (~18) were also acquired from each tissue site. As a result, a total of 874 *in vivo* Raman spectra from 47 sites were measured at transnasal endoscopy and used for spectral analysis [PN (n=521), FOR (n=157) and LVC (n=196)] from the 23 subjects.

4.3.2 Multivariate statistical analysis

Before the discriminant data-analysis, the raw Raman spectra were firstly smoothed using a linear Savitzky Golay filter, and tissue autofluorescence background was then subtracted from the smoothed spectra using a 5^{th} order polynomial fit. The background-subtracted Raman spectra were then normalized to the integrated areas under the curves to minimize the effect of Raman probe handling variations on clinical Raman measurements with respect to different subjects and tissue sites. All processed Raman spectra were assembled into a matrix, and the mean centering of the entire Raman dataset was then performed. To reduce the dimension of the spectral data, principal component analysis (PCA) was employed to extract a set of orthogonal principal components (PCs) that account for the maximum variance in the Raman spectral dataset for tissue characterization [208, 209]. Accordingly, loadings on the PCs represent orthogonal basis spectra of the most prominent spectral variation in the

dataset accounting for progressively decreasing variance, whereas the scores on the PCs represent the projection value of the tissue Raman spectra on the corresponding loading. Thus, PCA can efficiently be used to resolve spectral variations while reducing the dimension of the dataset to a minimum [209]. The number of retained PCs was chosen based on the analysis of variance (ANOVA) and Student's t-test at 0.05 levels. We employed *post-hoc* Fisher's least squares differences (LSD) test to assess differences in means [124]. Multivariate statistical analysis was performed using the PLS toolbox (Eigenvector Research, Wenatchee, WA) in the Matlab (Mathworks Inc., Natick, MA) programming environment.

4.3.3 Results and discussion

High quality *in vivo* Raman spectra can routinely be acquired in the nasopharynx and larynx in real-time during transnasal image-guided (i.e., WLR and NBI) endoscopic inspections. Figure 4.4 shows an example of *in vivo* raw Raman spectrum (weak Raman signal superimposed on large tissue autofluorescence background) acquired from the posterior nasopharynx with an acquisition time of 0.1 s at endoscopy.

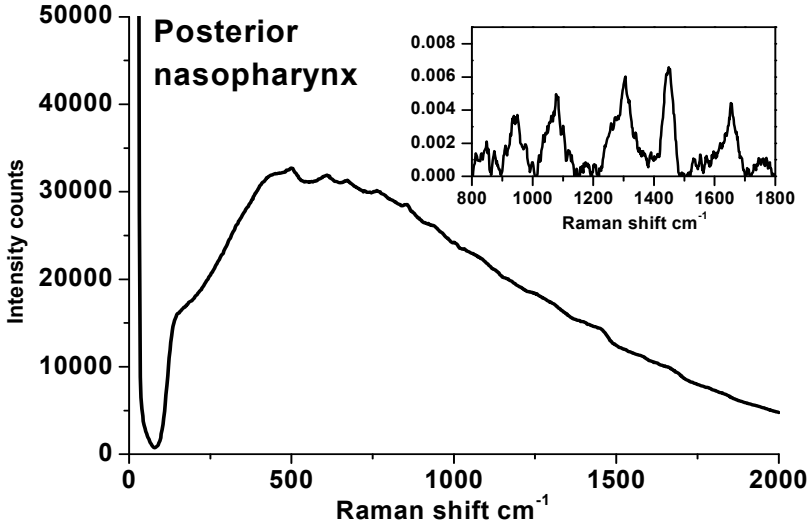

Fig. 4.4 Representative *in vivo* raw Raman spectrum acquired from the Fossa of Rosenmüller with 0.1 s during clinical endoscopic examination. Inset of Fig.4.4 is the processed tissue Raman spectrum after removing the intense autofluorescence background.

The background-subtracted tissue Raman spectrum with a signal-to-noise ratio (SNR) of >10 (Inset of Fig. 4.4) can be obtained and displayed on-line during clinical endoscopic measurements. Fig. 4.5 depicts the inter-subject in vivo mean Raman spectra ± 1 standard deviations (SD) of normal nasopharyngeal (i.e., PN (n=521) and FOR (n=157)) and laryngeal tissues (i.e., LVC (n=196)) when the Raman probe is gently contacted with the tissue under WLR/NB imaging guidance. Also shown is WLR images (Fig. 4.5) obtained from the corresponding anatomical locations.

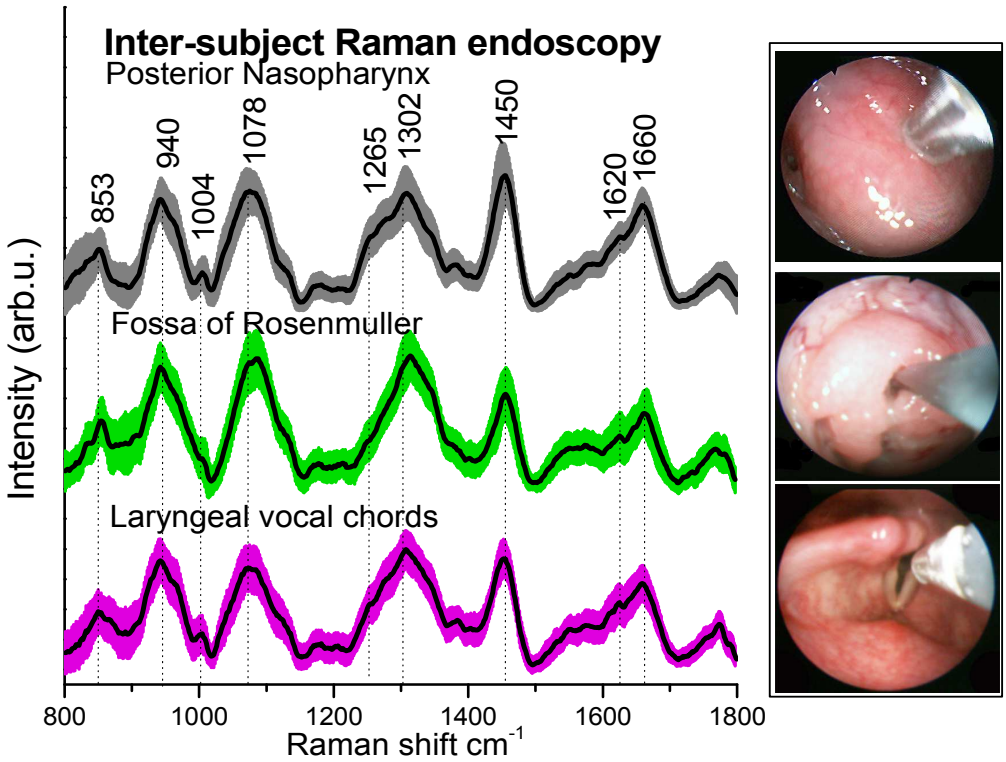

Fig. 4.5 *In vivo* (inter-subject) mean Raman spectra ± 1 standard deviations (SD) of posterior nasopharynx (PN) (n=521), fossa of Rosenmüller (FOR) (n=157) and laryngeal vocal chords (LVC) (n=196). Note that the mean Raman spectra are vertically displaced for better visualization. *In vivo* fiber-optic Raman endoscopic acquisitions from posterior nasopharynx (upper) fossa of Rosenmüller (mid) and laryngeal vocal chords (lower) under white light reflectance (WLR) and narrowband (NB) imaging guidance are also shown.

Prominent Raman bands associated with proteins and lipids are identified as tabulated in Table 4.1 with tentative biomolecular assignments [124, 125, 202, 208, 210].

Table 4.1 Tentative assignments of molecule vibrations and biochemicals involved in Raman scattering of nasopharyngeal and laryngeal tissue [124, 125, 202, 208, 210].

Raman peaks (cm^{-1})	Vibrations	Biochemicals
853	ν(C-C)	proteins
940	ν(C-C)	proteins
1004	νs(C-C) breathing	proteins
1078	ν(C-C)	lipids
1265	Amide III ν(C-N) δ(N-H)	proteins
1302	CH2 twisting and wagging	lipids/proteins
1450	δ(CH2)	lipids/proteins
1660	Amide I ν(C=O)	proteins

Note: ν, stretching mode; νs, symmetric stretching mode; δ, bending mode;

Figure 4.6 shows the intra-subject mean spectra ± 1 SD of a randomly chosen subject. The in vivo tissue Raman spectra were found to be reproducible with diminutive inter- and intra- subject variances (<10%) in the nasopharynx and larynx. Further Raman endoscopic testings indicate that the variability between different tissue sites within the posterior nasopharynx is subtle (< 5%) (data not shown).

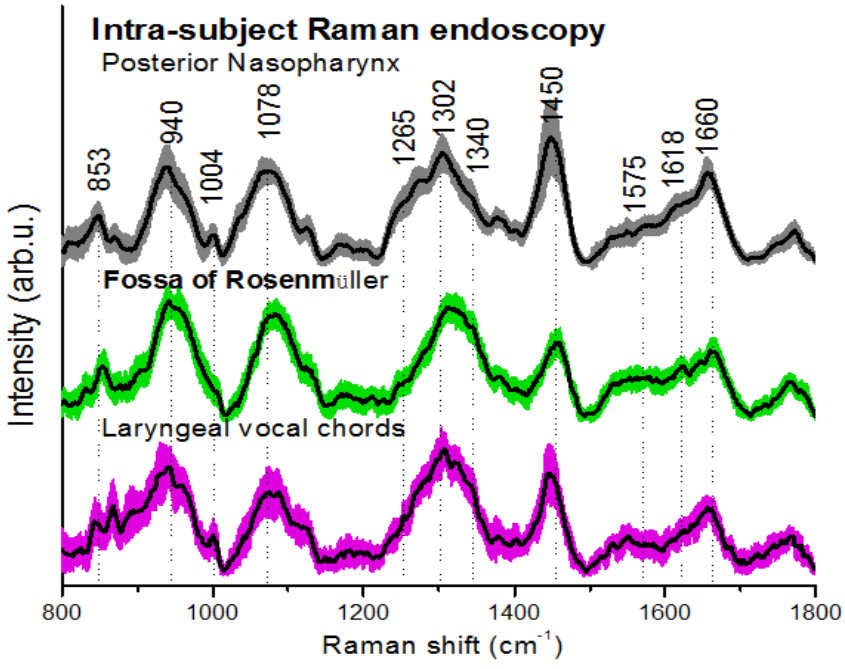

Fig. 4.6 *In vivo* (intra-subject) mean Raman spectra ± 1 SD of PN (n=18), FOR (n=18) and LVC (n=17). Note that the mean Raman spectra are vertically displaced for better visualization.

We also calculated difference spectra ± 1 SD between different tissue types (i.e., PN-LVC, LV-FOR and PN-FOR) as shown in Fig. 4.7, resolving the distinctive compositional and morphological profiles of different anatomical tissue sites at the biomolecular level. ANOVA revealed twelve prominent and broad Raman spectral sub-regions that showed significant variability ($p<0.0001$) between the three anatomical tissue sites centered at: 812, 875, 948, 986, 1026, 1112, 1254, 1340, 1450, 1558, 1655 and 1745 cm^{-1}, reconfirming the importance of characterizing the Raman spectral properties of nasopharynx and larynx toward accurate *in vivo* tissue diagnostics.

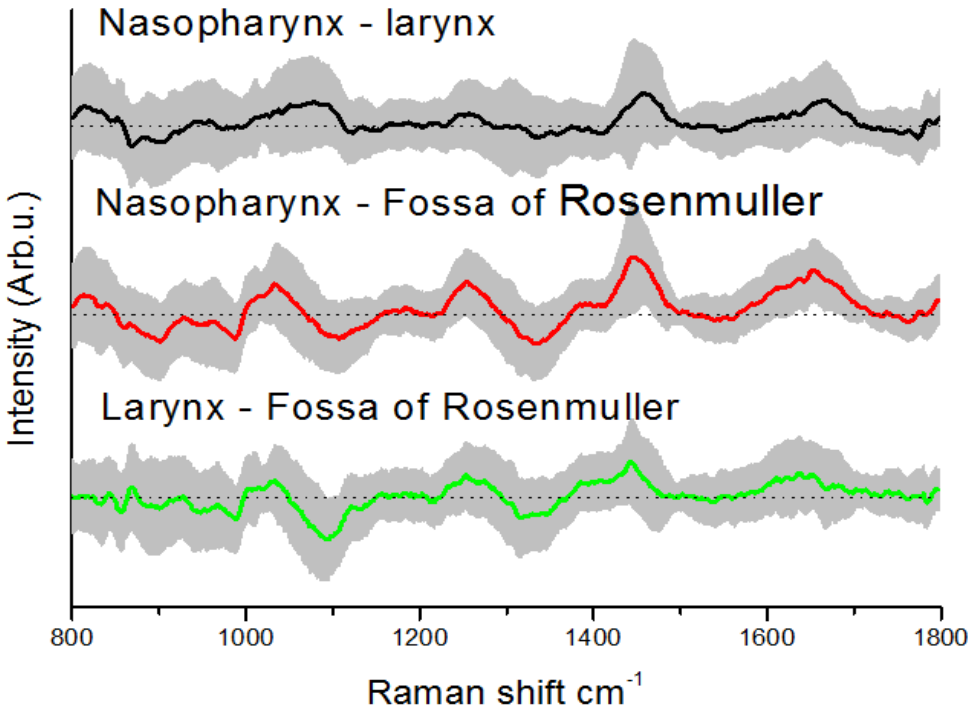

Fig. 4.7 Comparison of difference spectra ± 1 SD of different anatomical tissue types (inter-subject): [posterior nasopharynx (PN) – laryngeal vocal chords (LVC)]; [posterior nasopharynx (PN) – fossa of Rosenmüller (FOR)] and [laryngeal vocal chords (LVC) – fossa of Rosenmüller (FOR)].

To investigate the significance of potential confounding factors during transnasal endoscopy, we also measured *in vitro* Raman spectra of blood, saliva and nasal mucus obtained from healthy volunteers which were shown in Figure 4.8. The

most prominent Raman bands in saliva and nasal mucus are at 1638 cm^{-1} (v2 bending mode of water), whereas blood exhibits porphyrin Raman bands nearby 1560 and 1620 cm^{-1} [199].

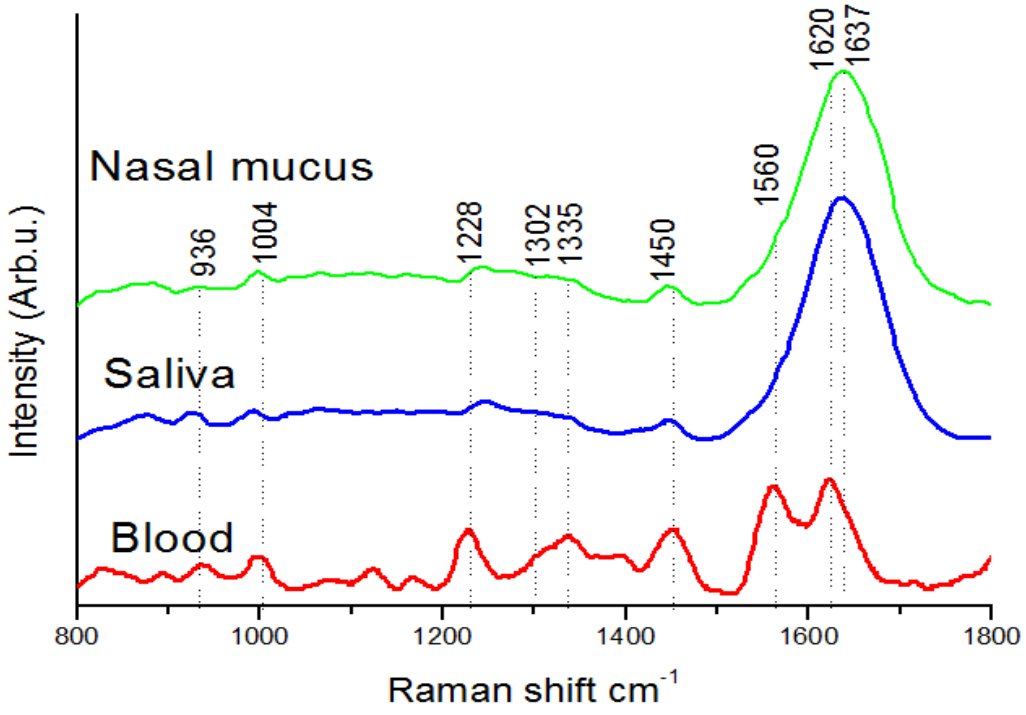

Fig. 4.8 *In vitro* Raman spectra of possible confounding factors from human body fluids (nasal mucus, saliva and blood).

To further assess the spectral differences among different tissues in the head and neck, a five-component PCA model based on ANOVA and student's t-test ($p<0.05$) accounting for 57.41% of the total variance (PC1: 22.86%; PC2: 16.16%; PC3: 8.13%; PC4 6.22% PC5: 4.04%) was developed to resolve the significant peak variations of different anatomical locations. Figure 4.9 shows the PC loadings revealing the resolve Raman bands associated with proteins (i.e., 853, 940, 1004, 1265, 1450 and 1660 cm^{-1}) and lipids (i.e., 1078, 1302 1440, 1655 and 1745 cm^{-1}).

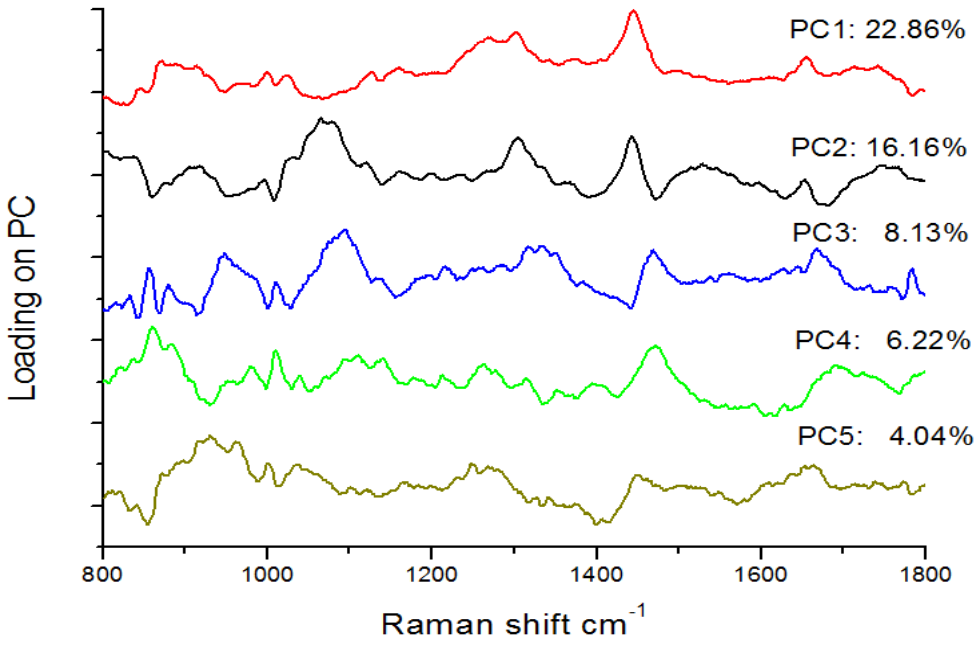

Fig. 4.9 PC loadings resolving the biomolecular variations among different tissues in the head and neck, representing a total of 57.41% (PC1: 22.86%; PC2: 16.16%; PC3: 8.13%; PC4 6.22% PC5: 4.04%) of the spectral variance.

Figure 4.10(A-E) displays box charts of PCA scores for the different tissue types (i.e., PN, FOR and LVC). The line within each notch box represents the median, and the lower and upper boundaries of the box indicate first (25.0% percentile) and third (75.0% percentile) quartiles, respectively. Error bars (whiskers) represent the 1.5-fold interquartile range. The p-values are also represented among different tissue types. Dichotomous PCA algorithms integrated with linear discriminant analysis (LDA) provided the sensitivities of 77.0% (401/521), 67.3% (132/192) and specificities of 89.2% (140/157) and 76.0% (396/521) for differentiation between PN vs. FOR, and LVC vs. PN, respectively using leave-one subject-out, cross validation.

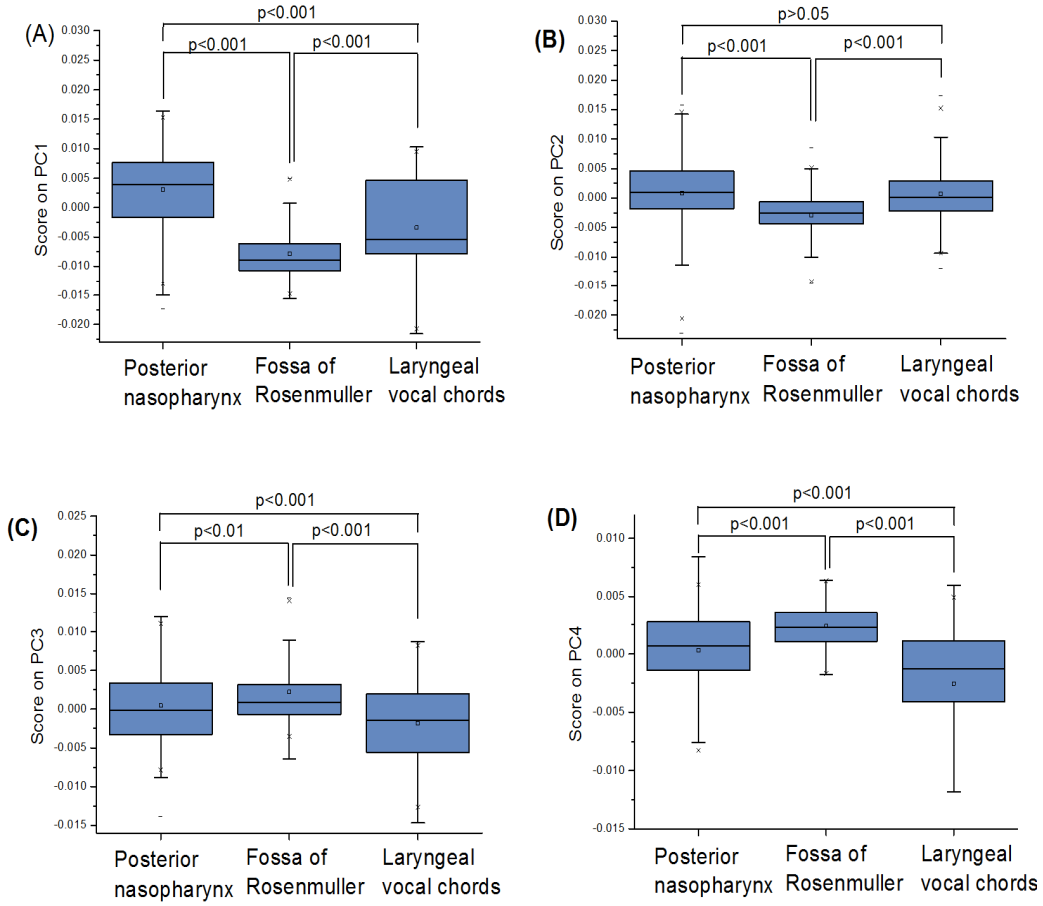

Fig. 4.10 Box charts of the 5 PCA scores for the different tissue types (i.e., PN, FOR and LVC). The line within each notch box represents the median, but the lower and upper boundaries of the box indicate first (25.0% percentile) and third (75.0% percentile) quartiles, respectively. Error bars (whiskers) represent the 1.5-fold interquartile range. The p-values are also given among different tissue types.

Overall, these results demonstrate that Raman spectra of nasopharynx and larynx in the head and neck can be measured *in vivo* at transnasal endoscopy, and the diagnostic algorithms development should be tissue site specific to ensure minimum algorithm complexity. Minimally invasive technologies such as Raman spectroscopy can greatly benefit in transnasal inspections of the larynx and nasopharynx at clinical endoscopy. *In vitro* studies have thoroughly demonstrated that NIR Raman spectroscopy is sensitive to carcinogenesis (i.e., precancer and cancer) in the head and neck including nasopharynx and larynx [130, 132, 211, 212]. Direct translation of this technology into clinic however remains very challenging, as efficient fiber probes,

short measurement times as well as online data processing and diagnosis are needed [144]. This study demonstrates for the first time the feasibility of Raman spectroscopy in transnasal endoscopic applications, providing the foundation for large-scale clinical studies in the head and neck. Our unique image-guided Raman endoscopy platform integrated with a miniaturized fiber Raman probe developed provides a rapid and minimally invasive assessment of endogenous tissue constituents of the head and neck at the molecular level during clinical endoscopic examination. This greatly facilitates clinicians to obtain detailed biomolecular fingerprints of tissue in the head and neck, reflecting the genuine compositional and morphological signatures without introducing the artifacts caused by vascular puncturing or tissue dehydration, morphological and anatomical effects, etc.

Distinct Raman bands nearby 936 (ν(C-C) proteins), 1004 (νs(C-C) ring breathing of phenylalanine), 1078 (ν(C-C) of lipids), 1265 (amide III ν(C-N) and δ(N-H) of proteins), 1302 (CH3CH2 twisting and wagging of proteins), 1445 (δ(CH2) deformation of proteins and lipids), 1618 (ν(C=C) of porphyrins), and 1660 cm^{-1} (amide I ν(C=O) of proteins) are consistently observed in different anatomical sites of the nasopharynx and larynx (Figs. 4.4 - 4.6). The difference spectra ±1 SD (Fig. 4.7) reveal that the Raman-active tissue constituents are comparable among different anatomical sites, but the subtle while highly molecular specific inter-anatomical variations were observed such as relative tissue Raman differences (spectral shape, bandwidth, peak position and intensity). With the 785 nm laser light penetration depth in the vicinity of ~800 μm in epithelial tissue [125], it is plausible that Raman spectra of nasopharyngeal tissues reflect the lymphoid-rich mucosa and epithelia type (i.e., mostly stratified squamous epithelium).

On the other hand, the distinct morphology in the fossa of Rosenmüller (i.e.,

cartilage) likely explains the spectral appearance associated with the pharyngeal recess. To further investigate the properties of inter-anatomical variability in the head and neck, PCA was employed to resolve the spectral variability. ANOVA and noise level was used to select the PCs in the model. The PCA modeling captured a total variation of 57.41% after mean-centering of the dataset (PC1: 22.86%; PC2: 16.16%; PC3: 8.13%; PC4 6.22% PC5: 4.05%) that were found to have significant different means (Fig. 4.10A-E). Indeed, this indicates that the majority of the spectral variation is related to inter-anatomical variability. We anticipate that the remaining variance not accounted for is due to probe handling variations associated with *in vivo* Raman endoscopic trials. The loadings on PC1 and PC2 (Fig. 4.9) are generally associated with lipid signals (i.e., 1302 cm^{-1} (CH2 twisting and wagging), 1440 cm^{-1} (δ(CH2)), 1655 cm^{-1} (ν(C=C)) and 1745 cm^{-1} (ν(C=O))) suggesting that FOR exhibit less signals from lipids (Fig. 4.10). Both PC1 and PC2 components largely reflect variations in lipids, indicating that distinct lipid types might be associated with the FOR tissues. In contrast, PC3, PC4 and PC5 represent complex signals related to proteins (i.e., 853 cm-1 (ν(C-C)), 936 cm^{-1} (ν(C-C)) 1004 cm-1 (ν(C-C)) 1450 cm^{-1} (δ(CH2)) and 1660 cm^{-1} (Amide I ν(C=O))), signifying that distinct anatomical locations are present with a highly specific compositional and morphological signature (Figs. 4.9 and 4.10). The two binary PCA-LDA classification algorithms with the leave-one subject- out, cross validation provide the sensitivities of 77.0%, 67.3% and specificities of 89.2% and 76.0% for differentiation among PN vs. FOR, and LVC vs. PN, respectively, reconfirming that the larynx and nasopharynx are unique organs. Therefore, the distinct Raman active biomolecules as well as morphology (e.g., mucosa thickness, cartilage, blood vessels, etc.) and optical properties together contribute to the complex spectral differences observed between

different tissue sites in the nasopharynx and larynx. Overall, the subtle spectral differences of distinct anatomical sites observed would inevitably induce additional model complexity in developing efficient Raman diagnostic algorithms (e.g., PCA-LDA, PLS-DA, classification and regression trees (CART), etc.) for precancer and cancer diagnosis in the head and neck [129, 130, 132, 208, 212].

To further investigate the influence of potential confounding factors at in vivo transnasal applications, the Raman spectra of body fluids (e.g., blood, saliva and nasal mucus) in the head and neck were also measured *in vitro* (Fig. 4.8). Saliva and nasal mucus are mostly associated with broad Raman peak at 1638 cm^{-1} (v2 bending mode of water), whereas the blood exhibits signals of porphyrins near 1560 and 1620 cm^{-1}. Comparisons with the nasopharyngeal and laryngeal tissue Raman spectra acquired (Fig. 4.5), we could find that those biochemical in the body fluids do not contribute significantly to the *in vivo* tissue Raman spectra at transnasal endoscopy. The *in vivo* nasopharyngeal and laryngeal tissue Raman results presented in this work is of great importance as it transfers the Raman technology from laboratory into *in vivo* real-time transnasal Raman endoscopy, paving the way for realizing early cancer and precancer diagnosis and detection in the head and neck as well as post therapeutic surveillance of head and neck cancer during clinical examination [129, 130, 132, 212]. One notes that the pharyngeal recess (FOR) could be too deep to be visually evaluated under conventional wide-field imaging modalities (Fig. 4.5), resulting in blind/random biopsies with poor diagnostic accuracy [10]. Our *in vivo* fiber-optic Raman endoscopy technique developed can be used for multiple but instant biochemical assessments of the tissue in situ (Fig. 4.5) that may potentially increase the diagnostic yield and ultimately improve the effectiveness of surveillance of epithelial lesions in the head and neck. In short, the *in vivo* Raman spectra of the head and neck tissue are very

similar but with subtle spectral differences. This observation correlates well with our previous study defining the Raman spectral properties of the upper gastrointestinal tract (i.e., esophagus and gastric) [124]. We have also established the Raman spectral profiles of dysplastic and neoplastic tissue in the lung, esophagus, gastric and colon, which in fact exhibit comparable difference spectra (e.g., cancer tissue shows upregulated DNA and protein but a relative reduction in lipid content) among different organs associated with neoplastic tissue transformation [124, 125, 202, 213, 214]. We anticipate that similar spectral difference profiles could be found in different pathologic tissues of the head and neck, but a large Raman dataset is needed to evaluate the specific impact of cancerous transformation within the distinct anatomical sites in the nasopharynx and larynx. As such, *in vivo* transnasal Raman endoscopic measurements on a larger number of patients are currently in progress to assess the specific biochemical foundations of the Raman spectral differences between different pathologic types of nasopharynx and larynx for developing robust Raman diagnostic algorithms for in vivo tissue diagnostics and characterization in the head and neck [215].

4.4 Conclusion

We demonstrate for the first time that transnasal image-guided Raman endoscopy can be used to acquire *in vivo* Raman spectra from nasopharyngeal and laryngeal tissue in real-time. Significant Raman spectral differences identified reflecting the distinct compositions and morphology in the nasopharynx and larynx should be considered as an important parameter in the interpretation and rendering of diagnostic decision algorithms for *in vivo* tissue diagnosis and characterization in the head and neck. Hence, the real-time ability of our rapid Raman endoscopy system under the guidance of different wide-field endoscopic imaging modalities for

acquiring high quality Raman spectra within 1 s or subseconds illustrates that such a rapid image-directed Raman endoscopy technique will greatly facilitate the adoption of Raman spectroscopy into clinical research and practice during routine endoscopic inspections.

Chapter 5 High Wavenumber Raman Spectroscopy for Laryngeal Cancer Diagnosis

In this chapter, we present our work on the implementation of the transnasal image-guided high wavenumber (HW) Raman spectroscopy to differentiate tumor from normal laryngeal tissue at endoscopy. A rapid-acquisition Raman spectroscopy system coupled with a miniaturized fiber-optic Raman probe was utilized to realize real-time HW Raman (2800 to 3020 cm^{-1}) measurements in the larynx. A total of 94 HW Raman spectra (22 normal sites, 72 tumor sites) were acquired from 39 patients who underwent laryngoscopic screening. Significant differences in Raman intensities of prominent Raman bands at 2845, 2880 and 2920 cm^{-1} (CH_2 stretching of lipids), and 2940 cm^{-1} (CH_3 stretching of proteins) were observed between normal and cancer laryngeal tissue. The diagnostic algorithms based on principal components analysis (PCA) and linear discriminant analysis (LDA) together with the leave-one subject-out, cross-validation method on HW Raman spectra yielded a diagnostic sensitivity of 90.3% (65/72) and specificity of 90.9% (20/22) for laryngeal cancer identification. This study demonstrates that HW Raman spectroscopy has the potential for the non-invasive, real-time diagnosis and detection of laryngeal cancer at the molecular level.

5.1 Introduction

Laryngeal cancer is one of the most common malignancies in humans worldwide due to its high incidence rate and mortality [216]. For instance, in Southeast Asia, the rates of incidence and mortality of laryngeal cancer are significantly higher than other areas of the world [9, 217]. Early cancer diagnosis in the larynx with effective treatment (e.g., surgery, radiotherapy or chemotherapy alone

or in combination) is crucial to improving the 5-year survival rate [216, 218]. Positive endoscopic biopsy currently is the gold standard for cancer diagnosis, but it is invasive and impractical for screening high risk patients, which might affect the quality of the voice due to multiple biopsies [218]. Fiber-optic laryngoscopy is the primary physical examination tool options for now [216], which rely on white-light illumination while require highly experienced skills of recognization and locating pathologic tissues [219]. Raman spectroscopy is a unique vibrational technique capable of probing biomolecular changes in tissue, which has shown great promise for early diagnosis and detection of precancer and cancer diagnosis in a variety of organs (e.g., skin, cervix, lung, esophagus, stomach, colon, kidney, bladder, breast, nasopharynx and the larynx) [114, 129, 130, 171, 200, 202, 206, 209, 212, 220-231]. Current Raman research in diagnosing laryngeal cancer is mostly only focused on the so-called fingerprint region (i.e., 800 to 1800 cm^{-1}) that contains rich biochemical information about the tissue [129, 130, 210, 212, 228]. However, the strong fluorescence background and Raman signals attributed to the silica fiber severely interfere with the detection of the inherently weak tissue Raman signal, leading to a complex fiber probe filtering design as well as signal analysis in the fingerprint region. On the other hand, the high wavenumber (HW) (2800-3800 cm^{-1}) Raman spectroscopy can also provide complementary biochemical information for tissue diagnosis and characterization with much stronger tissue Raman signals but reduced tissue/fiber fluorescence background, as compared to the fingerprint Raman spectroscopy [209, 232, 233]. To date, HW Raman spectroscopy for laryngeal tissue diagnosis and characterization has yet been reported in literature.

In this chapter, we proposed the implementation of the transnasal image-guided HW Raman spectroscopy developed to differentiate tumor from normal

laryngeal tissue. A rapid-acquisition Raman spectroscopy system coupled with a miniaturized fiber-optic Raman probe was utilized to realize real-time HW Raman (2800 to 3020 cm^{-1}) measurements in the larynx. Multivariate statistical techniques, including principal components analysis (PCA) and linear discriminant analysis (LDA), are utilized to develop diagnostic algorithms for differentiation between normal and cancerous laryngeal tissue. The receiver operating characteristic (ROC) curve is also conducted to further evaluate the performance of PCA-LDA algorithms on HW Raman spectroscopy for laryngeal cancer diagnosis.

5.2 HW Raman Spectroscopy for Cancer Diagnosis

5.2.1 Raman endoscopic instrument

The novel image-guided Raman endoscopy platform developed for in vivo tissue measurements and characterization has been described in Figure 5.1. Briefly, the Raman spectroscopy system consists of a spectrum stabilized 785 nm diode laser (maximum output: 300 mW, B&W TEK Inc., Newark, DE), a transmissive imaging spectrograph (Holospec f/1.8, Kaiser Optical Systems) equipped with a liquid nitrogen cooled (-120^{o}C), NIR-optimized, back-illuminated and deep depletion charge-coupled device (CCD) camera (1340×400 pixels at 20×20 μm per pixel; Spec-10: 400BR/LN, Princeton Instruments). We have constructed a 1.8 mm fiber-optic Raman endoscopic probe with dual coatings on the fiber tip for optimizing both the tissue excitation and Raman collections [144]. The 785 nm laser is coupled into the central delivery fiber (200 μm, NA=0.22) of the Raman probe for tissue excitation, while the backscattered tissue Raman photons from the laryngeal tissue are collected by the surrounding fibers (32x200 μm, NA=0.22). The Raman fiber probe fits into the instrument channel of laryngoscope and can be safely targeted to different locations in

the larynx under the multimodal wide-field imaging (i.e., white-light reflectance (WLR) and narrow-band imaging (NBI)) guidance.

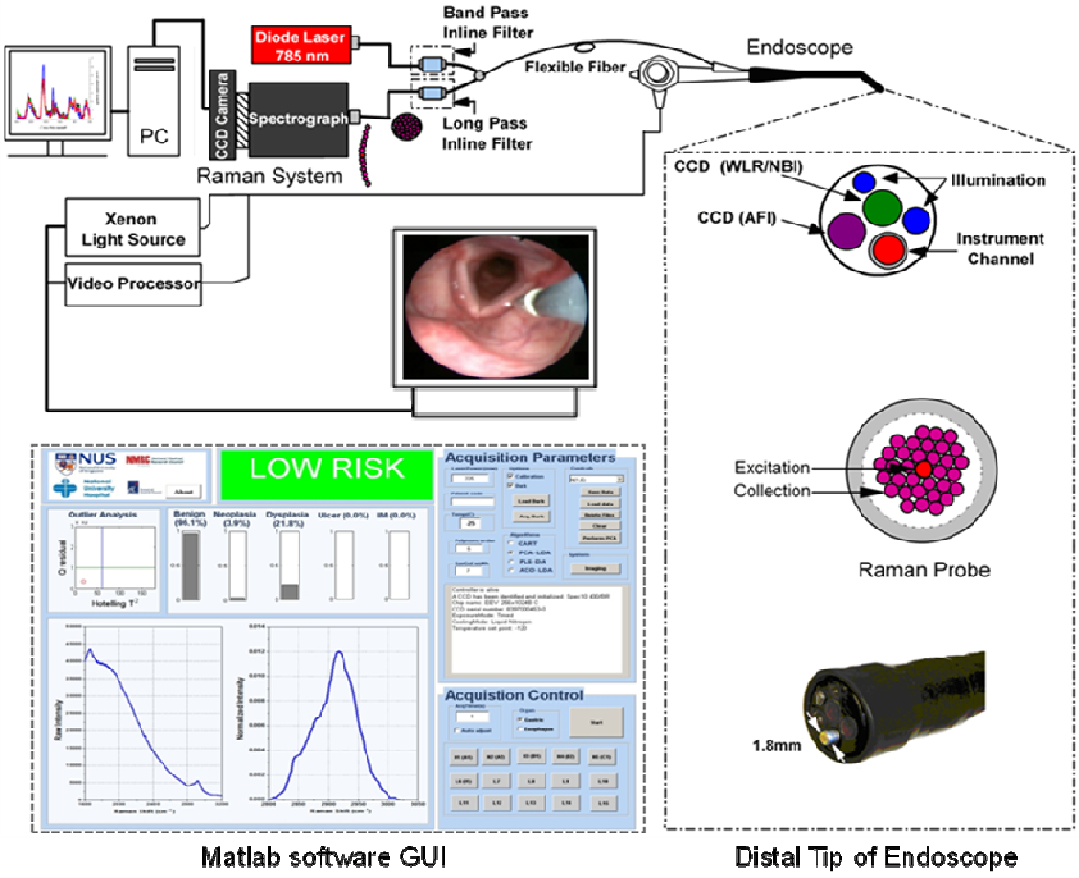

Fig. 5.1 Schematic of the integrated Raman spectroscopy and trimodal endoscopic imaging system with software GUI (lower left) developed for *in vivo* tissue Raman measurements in larynx.

By tuning the grating position, the Raman system acquires HW Raman spectra over the HW range of 2800-3020 cm^{-1}, and each raw spectrum is acquired within 1 s with light irradiance of 1.5 W/cm^2. The spectral resolution of the system is about 9 cm^{-1}, and all wavelength-calibrated HW Raman spectra are also corrected for the wavelength-dependence of the system using a standard lamp (RS-10, EG&G Gamma Scientific, San Diego, CA). HW Raman spectra are then extracted from the raw tissue spectra using established preprocessing methods including smoothing, baseline subtraction, etc [206]. All the spectral pre-processing is completed on-line, and the Raman spectra (raw data (1510-3200 cm^{-1}) and normalized data (HW range)) and the

outcome of decision algorithms can be displayed in real-time in a comprehensible graphical user interface (GUI) shown in Figure 5.1(lower left) during clinical transnasal Raman endoscopy.

5.2.2 Subjects and procedures

This study was approved by the SingHealth Centralized Institutional Review Board (IRB), Singapore. A total of 39 different patients with a mean age of 60 who underwent surgical resection due to laryngeal malignancies were recruited for this study. All patients preoperatively signed an informed consent permitting Raman measurements on laryngeal tissue. HW Raman spectra were directly acquired from the suspicious lesion sites for each patient through gently placing the fiber-optic Raman probe on the tissue with signal acquisition time of <1 s. HW Raman spectra were also measured from the surrounding normal sites that appear completely normal in the laryngoscopist's opinion (i.e., normal tissue does not exhibit colored patterned changes that only accompany precursor lesions) [191], but no biopsies were taken from normal appearing tissue. Only highly abnormal sites measured were biopsied and then submitted for histopathologic examination. A total of 94 Raman spectra (22 normal, 72 tumor as confirmed by histopathology) from different tissue sites were collected. For the assessment of diagnostic sensitivity and specificity of Raman endoscopy for tissue classification, histopathological results served as the gold standard.

All raw spectral data were processed on-line with software developed in the Matlab environment (The MathWorks, Inc., Natick, MA) [206]. Raw spectra are first pre-processed by a first-order Savitsky-Golay filter to reduce background noise [234]. A first-order polynomial was used to fit tissue autofluorescence background and then subtracted from the raw spectra to obtain the pure HW Raman spectra. The HW

Raman spectra are then normalized over the integrated area under the curve from 2800 to 3020 cm^{-1} to allow a better comparison of the spectral shapes and relative Raman band intensities among different subjects/tissue sites [202]. Principal components analysis (PCA) was used to reduce dimensionality of the Raman data (each Raman spectrum ranging from 2800 to 3020 cm^{-1} with set of 255 intensities), retaining the most diagnostically significant information for effective tissue classification. The spectra were first standardized to ensure that mean of the spectra was zero and the standard deviation (SD) was one, eliminating the influence of inter- and/or intra-subject spectral variability on PCA. Mean centering ensures that the principal components (PCs) form an orthogonal basis [188, 189]. Thus, PCA were employed to extract a set of orthogonal PCs comprising loadings and scores that accounted for most of the total variance in original spectra. Each loading vector is related to the original spectrum by a variable called the PC score, which represents the weight of that particular component against the basis spectrum. The most diagnostically significant PCs ($p<0.05$) were determined by Student's *t-test* and then selected as input for the development of linear discriminant analysis algorithms for classification [189]. LDA determines the discriminant function that maximizes the variances in the dataset between groups while minimizing the variances between members of the same group. The performance of the diagnostic algorithms rendered by the PCA-LDA models for correctly predicting the tissue groups (e.g. normal *vs.* cancer) was estimated in an unbiased manner using the leave-one subject-out, cross-validation method [188, 235] on all model spectra. In this method, the spectra from each same patient were held out from the data set and the PCA-LDA modeling was redeveloped using the remaining HW Raman spectra. The redeveloped PCA-LDA diagnostic algorithm was then used to classify the withheld spectra. This process was

repeated until all withheld spectra were classified. Receiver operating characteristic (ROC) curves were generated by successively changing the thresholds to determine correct and incorrect classifications for all tissues. Multivariate statistical analysis were performed online using in-house written scripts in the Matlab (Mathworks Inc., Natick, MA) programming environment [206].

5.3 Results

5.3.1 Tissue Raman spectra

Figure 5.2A shows the comparison of mean HW Raman spectra ±1 SD of normal (n=22) and cancer (n=72) laryngeal tissue.

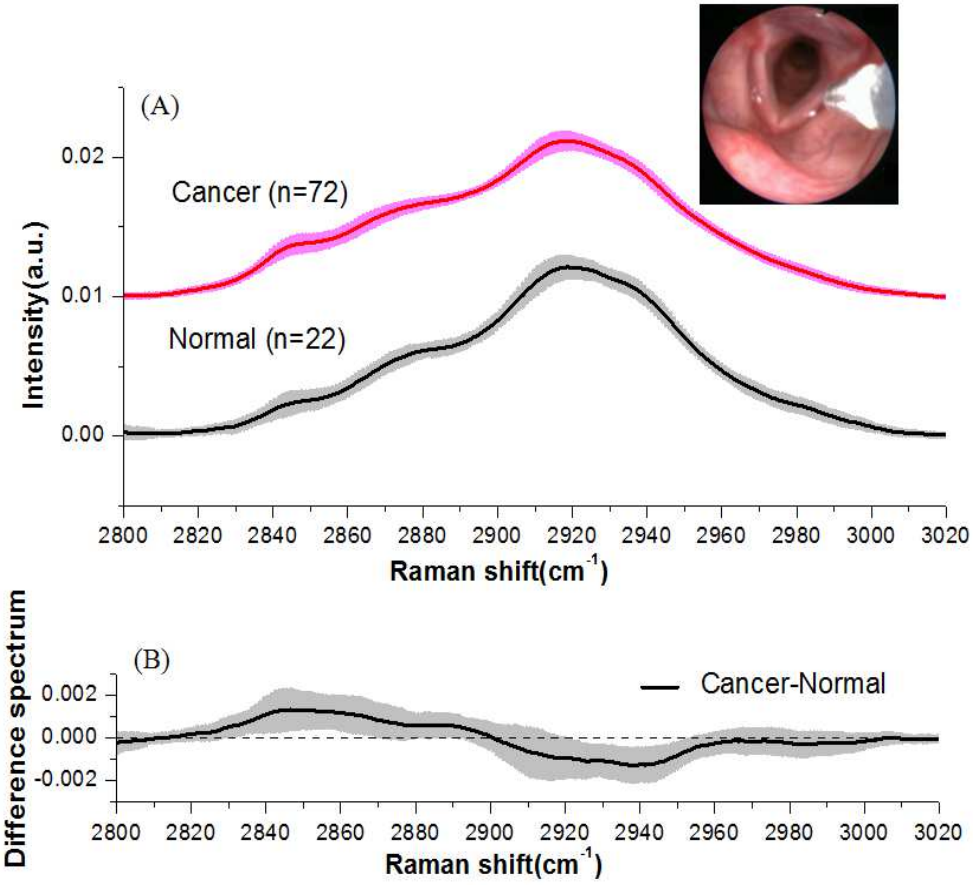

Fig. 5.2 (**A**) comparison of the mean HW Raman spectra ±1 standard deviations (SD) of normal (n=22) and cancer (n=72) laryngeal tissue. **(B)** Difference spectrum ±1 SD between cancer (n=72) and normal laryngeal tissue (n=22). Note that the mean normalized HW Raman spectrum of normal tissue was shifted vertically for better visualization (panel A); the shaded areas indicate the respective standard deviations. The picture shown is the Raman acquisitions from the larynx using endoscopic fiber-optic Raman probe.

Prominent Raman bands such as 2845, 2880, and 2920 cm^{-1} (CH_2 stretching of lipids), and 2940 cm^{-1} (CH_3 stretching of proteins) are found in both normal and tumor laryngeal tissues [209, 236, 237]. As shown in the difference spectrum (Figure 5.2B), the intensities of Raman band between 2812 to 2900 cm^{-1} in cancer tissue is obviously greater than normal tissue, while the Raman band between 2900 to 3020 cm^{-1} the normal is higher. This suggests that there is an increase or decrease in particular types of biomolecules relative to the total Raman-active biomolecules in cancer tissue as compared to normal tissue, demonstrating the potential role of HW Raman spectroscopy for cancer diagnosis in the larynx.

5.3.2 Cancer diagnosis by using PCA-LDA

To determine the most significant Raman features for tissue analysis and classification, the multivariate statistical technique (e.g., PCA-LDA) coupled with Student's t-test are performed by incorporating the entire HW Raman spectra. Figure 5.3 shows the first five dominant principal components (PCs) accounting for about 99.2% (PC1: 89.1%; PC2: 7.41%; PC3: 1.52%; PC4: 1.08%; PC5: 0.07%) of the total variance calculated from HW Raman spectra of laryngeal tissues. Overall, the PC features among different PCs are different, but some PC features roughly correspond to HW Raman spectra, with peaks and troughs at positions (e.g., (CH2 stretch band (lipids) near 2845 cm^{-1}, 2880 cm^{-1}, 2920 cm^{-1} and CH3 stretch band (proteins) near 2940 cm^{-1}) similar to those of tissue HW Raman spectra. The first PC accounts for the largest variance within the spectral data sets (i.e., 89.1%), whereas successive PCs describe features that contribute progressively smaller variances. Unpaired two-sided Student's t-tests on the first five PCs show that only three PCs (PC1, PC2 and PC3, $p<0.05$) are diagnostically significant.

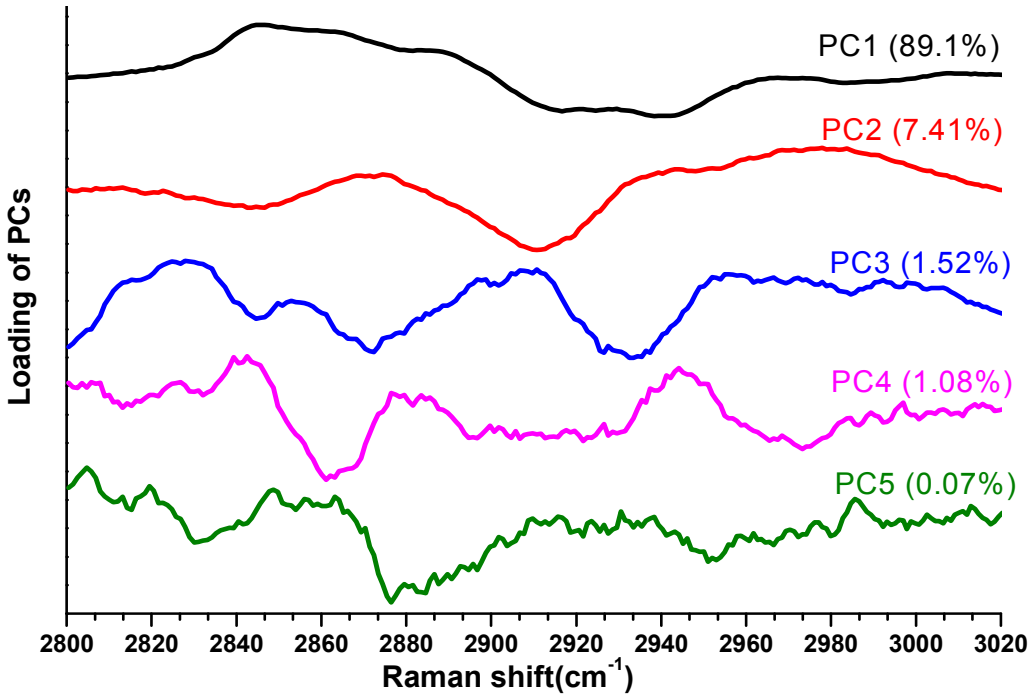

Fig. 5.3 The first five principal components (PCs) accounting for about 99.2% of the total variance calculated from HW Raman spectra of laryngeal tissue (PC1=89.1%; PC2=7.41%; PC3=1.52%; PC4=1.08%; PC5=0.07%).

To develop effective diagnostic algorithms for tissue classification, the three diagnostically significant PCs are fed into the LDA model together with leave-one subject-out, cross-validation technique for tissue classification. PCA-LDA algorithms on the HW tissue Raman data provide the diagnostic sensitivity of 90.3% (65/72) and specificity of 90.9% (20/22) for laryngeal cancer identification which is shown below in Figure 5.4.

In addition, Figure 5.5 shows the ROC curve which was also generated from the posterior probability plot in Figure 5.4 at different threshold levels, displaying the performance of PCA-LDA-based diagnostic algorithms derived for laryngeal cancer detection. The integration area under the ROC curve is 0.97 which further confirms that HW Raman technique coupled with PCA-LDA-based diagnostic algorithms is robust for laryngeal cancer diagnosis.

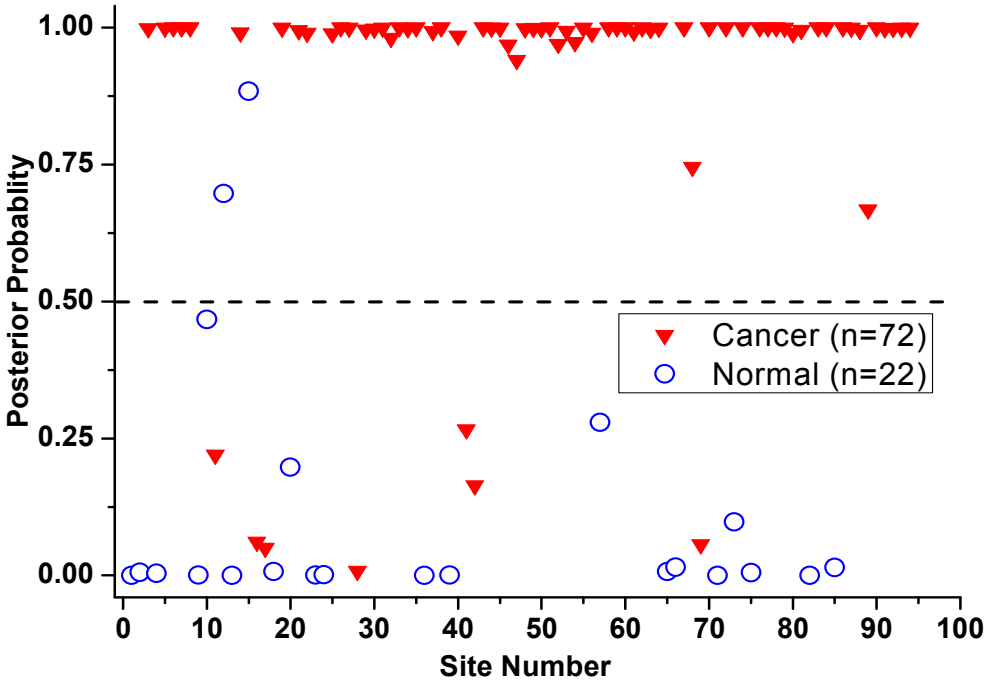

Fig. 5.4 Scatter plot of the linear discriminant scores for the normal and cancer categories using the PCA-LDA method together with leave-one subject-out, cross-validation method. The algorithm yields a diagnostic sensitivity of 90.3% and specificity of 90.9% for differentiation between normal and tumor tissues.

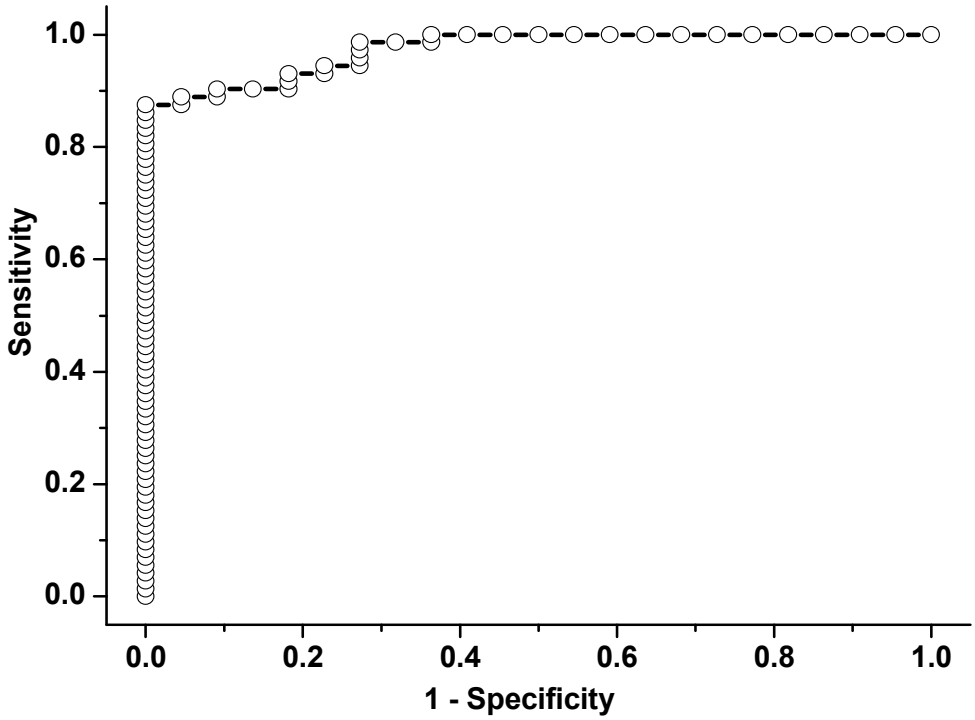

Fig. 5.5 ROC curve of discrimination results for Raman spectra utilizing the PCA-LDA-based spectral classification with leave-one subject-out, cross validation. The integration area under the ROC curves is 0.97 for PCA-LDA-based diagnostic algorithm.

5.4 Discussion

Raman spectroscopy holds a great promise for clinical application, as it can be used as a non-invasive technique for tissue Raman signal detection of biomolecular changes associated with tissue pathology. Our study demonstrates that HW Raman technique is capable to generate spectral differences between normal and cancer tissue in the larynx as shown in Figure 5.2 above. The empirical analysis based on the intensity ratio measurements which relate to the changes in protein-to-lipid contents has already been reported in literature [202, 214]. Student's t-test ($p<0.0001$) is used to test the significant difference of Raman intensity ratios of normal and cancer tissues. Intensity at 2920 cm^{-1} and 2940 cm^{-1} is higher in normal tissues, while at 2845 and 2890 cm^{-1} are higher in cancer tissues. The three significant Raman peak intensity ratios of I_{2940}/I_{2845}, I_{2940}/I_{2890} and I_{2940}/I_{2920} correlated with their histopathologic findings were also evaluated, and the decision lines (i.e., diagnostic algorithms) separated cancer from normal tissues with a sensitivity of 72.2% (52/72), 45.8% (33/72) and 44.4% (32/72), while a specificity of 81.8% (18/22), 72.7% (16/22) and 63.6% (14/22), respectively, for laryngeal cancer identification. These indicate that different ratios of Raman band intensities only give a certain levels of accuracy for tissue classification. The Raman intensity ratios of I_{2940}/I_{2845} and I_{2940}/I_{2890} are both lower for cancer tissue, this may due to the decrease in content of collagen. In cancer progression, from genetic mutation to invasive cancer in the laryngeal site, the epithelium turns thicker and thus obstructs the collagen Raman emission from deep collagen basal membrane, thereby decreases the overall ratio of I_{2940}/I_{2845} in laryngeal cancer tissue [200].

Besides, the contribution of collagen in cancer tissue should be reduced due to proliferation of cancerous cells and express as a class of metalloportease which in turn

decrease the content of collagen level. Raman band at 2845 cm^{-1} is tentatively ascribed to CH2 lipids and it seems to correspond to Raman peak at 1450 cm^{-1} in the fingerprint region, which is assigned to CH2 protein/lipids. CH2 protein/lipids are found to be higher in cancer than in normal laryngeal tissues, which can be explained by the increase of mitotic activity in the nucleus [200, 209, 212, 224, 228]. The distinctive differences in HW Raman spectra between normal and cancer laryngeal tissues reinforce that HW Raman spectroscopy can be used to reveal molecular changes associated with carcinogenesis progression. Considering the complexity of biological tissue, multivariate statistical analysis (PCA-LDA) which incorporates the entire Raman spectra data for analysis is more robust and rigorous to differentiate spectra that represent either normal or cancer tissue. Compared with intensity ratio approach, there is a great improvement in diagnostic sensitivity (~25%) and specificity (~11%) of PCA-LDA algorithms (Fig.5.4). The ROC curve (Fig.5.5) of PCA-LDA modeling (AUC=0.97) further verifies a better diagnostic efficacy of HW Raman spectroscopy integrated with PCA-LDA algorithm as compared to the intensity ratio diagnostic algorithms. One notes that PCA is primarily for data reduction rather than identification of biochemical or biomolecular components of tissue, it is difficult to interpret the physical meanings from the component spectra. This could be tackled by using more powerful diagnostic algorithms such as genetic algorithms [238], the distinctive spectral regions that are optimal for tissue differentiation may be indentified and related to particular biochemical and biomolecular changes (e.g., proteins, lipids and nucleic acid) associated with neoplastic changes.

It is also crucial to further understanding the relationship between the neoplastic-related morphologic/biochemical changes and tissue HW Raman spectra

for laryngeal precancer/cancer diagnosis [200, 206, 212]. We are currently working on this direction by recruiting more patients for developing more powerful HW Raman genetic diagnostic algorithms for real-time laryngeal tissue diagnosis and characterization.

5.5 Conclusion

In summary, this work demonstrates that transnasal image-guided real-time HW Raman spectroscopic technique integrated with an endoscope-based fiber-optic Raman probe can be used to acquire HW Raman spectra from laryngeal tissue in the range 2800-3020 cm^{-1} during clinical endoscopic examination. The significant differences in HW Raman spectra are observed in normal and cancer laryngeal tissues. The PCA-LDA modeling on HW Raman spectra provides good tissue classification, illustrating the potential of HW Raman spectroscopy for real-time laryngeal cancer detection during clinical endoscopic examination.

Chapter 6 Conclusions and Future Directions

6.1 Conclusions

In this dissertation, the motivation for our research is to investigate the feasibility of combining different optical spectroscopic and imaging techniques developed to improve the diagnosis of cancer in the head and neck compared to the diagnosis by individual spectroscopic method alone. First of all, we have evaluated feasibility of applying the developed endoscope-based AF/DR spectroscopy and AF/WLR imaging system for clinical evaluation of human tissues, and to characterize the properties of internal and external organ tissues (i.e., oral and skin). The AF/WLR images and point-wise AF/DR spectra can be simultaneously acquired from the same tissue site imaged without introducing an optical fiber catheter into the instrument channel of an endoscope as compared to conventional endoscopic spectral measurements which prolong the endoscopic operation procedures. The results demonstrate that the point-wise DR/AF spectra from different anatomical tissue locations also vary, revealing the differences in concentrations of endogenous fluorophores among different tissue locations. A total of 446 *in vitro* AF/DR spectra (207 normal, 239 tumor) from different tissue sites were collected by using the integrated AF/DR spectroscopic and imaging system. The composite AF and DR spectra were further analyzed using principal component analysis (PCA) and linear discriminant (LDA), yielding a diagnostic accuracy of 94.8% (sensitivity of 91.6% and specificity of 98.6%) for normal and cancer classification, which shows a significantly improved diagnostic accuracy compared to the AF or DR spectra alone.

Secondly, an integrated Raman spectroscopy and endoscopy based trimodal (white-light reflectance, autofluorescence and narrow band) imaging technique for

real-time *in vivo* tissue Raman measurements was developed. A customized endoscopic Raman probe (diameter < 2mm) with filtering modules is developed to maximize Raman collections from the tissue by eliminating the interference of fluorescence background and silica Raman from fibers. High quality *in vivo* Raman spectra can be acquired within 1s under the guidance of different wide-field imaging modalities. After that, a total of 874 *in vivo* Raman spectra were successfully acquired from different sites of the nasopharynx and larynx (PN (n=521), FOR (n=157) and true LVC (n=196)) from 23 normal volunteers during endoscopy examinations. Multivariate statistical techniques, including principal components analysis (PCA) and linear discriminate analysis (LDA) together with the leave-one tissue site-out, cross validation, were further applied to develop diagnostic algorithms for classification. The PCA-LDA modeling on *in vivo* Raman spectroscopy yielded a sensitivity of 77.0% and specificity of 89.2% for differentiation between PN vs. FOR, and sensitivity of 67.3% and specificity of 76.0% for distinguishing LVC vs. PN, demonstrating the potential of transnasal image-guided Raman spectroscopy for *in vivo*, rapid and non-invasive identification of nasopharynx and larynx in real-time.

We have also explored the utility of transnasal image-guided high wavenumber (HW) Raman spectroscopy to differentiate tumor from normal laryngeal tissues at endoscopy, and the fiber-optic Raman system acquires HW Raman spectra over the range of 2800-3020 cm^{-1} within 1 s at clinical endoscopy. We have applied the HW Raman spectroscopy to acquire a total of 94 all wavelength-calibrated HW Raman spectra (22 normal sites, 72 tumor sites) with spectral resolution of 9 cm^{-1} from 39 patients who underwent laryngoscopic screening. Significant differences in Raman intensities of prominent Raman bands at 2845, 2880 and 2920 cm^{-1} (CH2 stretching of lipids), and 2940 cm^{-1} (CH3 stretching of proteins) were observed

between normal and cancer laryngeal tissues. PCA-LDA modeling on HW Raman spectra yields a diagnostic sensitivity of 90.3% and specificity of 90.9% for laryngeal cancer identification.

In summary, we have developed and assessed the potential of the novel multimodal optical spectroscopy and imaging technique developed for the sensitive and specific detection of cancer in the head and neck (e.g., nasopharynx and larynx). The three spectroscopic techniques (diffused reflectance, autofluorescence and Raman scattering) are able to be integrated with different endoscopic imaging modalities (i.e., WLR, NBI and AFI) simultaneously and provide comprehensive information about tissue biochemistry and morphology which are altered with cancer development. The work in this thesis demonstrates that the integrated multimodal spectroscopy and imaging technique developed has the potential to be a clinically powerful tool for improving cancer diagnosis and detection in the head and neck during clinical endoscopic examinations.

6.2 Future Directions

The work presented in the thesis mainly focuses on the development of multimodal spectroscopy and imaging system for tissue diagnosis, but it still suffer from some limitations, such as lack of depth-resolved ability, and optical section ability for three-dimensional (3D) tissue imaging, etc. To address these issues, Some directions for further research are proposed as follows:

1) Development of fiber-optic confocal Raman probe for enhancing epithelial tissue Raman measurements at endoscopy

NIR Raman spectroscopy is a unique vibrational technique capable of probing biomolecular structures and compositions of tissue, and has excelled in the early

detection of precancer and cancer in internal organs [125, 126, 137, 144, 203, 239]. Very recently, the volume-typed fiber-optic Raman endoscopic probe coupled with high throughput Raman system has been developed for rapid tissue Raman acquisitions and cancer diagnostics in internal organs [137, 144, 203, 239]. As carcinogenic onset (e.g., dysplasia) initially evolves in the epithelial tissue layer, it is highly desirable to develop a depth-resolved Raman probe to selectively target the epithelium during clinical endoscopy. Furthermore, certain internal organs and anatomical tissue sites (e.g., lung, esophageal junction, gastric body region and tongue) emit relatively strong tissue AF background under the NIR laser excitation (e.g., 785 nm, 830 nm), which may obscure the inherently weak tissue Raman signal while rapidly saturates the charge-coupled device (CCD) in clinical settings. To reduce the tissue NIR AF interference and ensure sensitive detection of the shallower layer tissue structures, we are working on developing a compact confocal Raman endoscopic probe coupled with a small ball lens for enhancing *in vivo* epithelial tissue Raman measurements at endoscopy. The basic prototype of confocal Raman probe design for *in vivo* tissue Raman measurements at endoscopy is shown in Fig. 6.1a. Monte Carlo (MC) simulation method was employed to evaluate the performance of the ball-lens Raman probe designs under different optical configurations (Fig. 6.1b). Both the MC simulations and measurements show that the collection efficiency of the confocal Raman probe has a decreasing trend with the increased fiber-ball lens gaps. Our further MC simulations indicate that when the ball lens-fiber gap distance is close to 800-1000 μm, confinement to the shallow epithelium can be improved up to ~6% and approximately 75% of tissue Raman photons collected could largely originate from shallow epithelial tissue (within 150 μm) (blue curve in Fig. 6.1b). The cumulative Raman photons collected as a function of tissue depth under the beveled fiber

confocal Raman probe with a ball-lens (Fig. 6.1c) indicates that a maximum of tissue Raman signal can be acquired at the tissue depth of ~72 μm in the epithelium; and almost 90% of the total Raman signal collected originates from the epithelium (within 150 μm) with negligible contributions from the stromal layer (less than 5%). We have also characterized the confocal ability of the beveled-fiber confocal Raman probe developed using a polished silicon chip (Raman peak at 520 cm^{-1}); the full width of half maximum (FWHM) for the depth of focus acquired is about 93 μm, which is similar to the simulation result of ~100 μm (Fig. 6.1c).

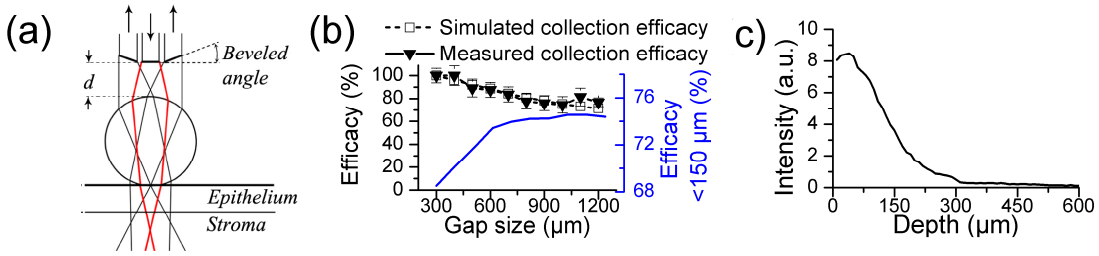

Fig. 6.1 (a) Schematic of the beveled fiber-optic confocal Raman probe coupled with a ball lens for *in vivo* tissue Raman measurements at endoscopy; (b) Comparison of the calculated and measured Raman collection efficiencies (normalized to maximum) as a function of the gap distance d between the fiber tip to the ball lens (left y-axis). The blue colored curve in Fig 1b is the calculated Raman collection efficiency from the shallow epithelium (within 150 μm) with respective to the total Raman emission in two-layered buccal tissue (right y-axis); (c) The depth-resolved distribution of Raman photons collected in two-layered tissue model.

We also compared the performance of the confocal Raman probe with a volume-typed Raman probe at endoscopy. The 785 nm laser intensities on the tips of the confocal probe and volume-typed probe are regulated to obtain comparable laser irradiances on the tissue surface. *In vivo* Raman spectra were obtained from the same gastric tissue site using both the confocal probe and volume-typed probe with 0.5 s integration time. Fig. 6.2a shows the mean *in vivo* raw spectra as well as the ratio spectrum (confocal spectrum divided by volume spectrum) of the gastric tissue acquired from a patient undergoing the endoscopic examination with histopathological confirmed normal mucosa. The *in vivo* gastric tissue Raman spectra

acquired by using both the confocal and volume-typed Raman probes are shown in Fig. 6.2b. Obviously, the stronger and better signal-to-noise ratio (SNR) *in vivo* Raman spectra can be acquired from gastric tissue using the confocal probe with a much reduced tissue AF (reduced by ~30% as shown in ratio spectrum in Fig. 6.2a), suggesting that NIR AF primarily originating from the deeper tissue layers can be significantly suppressed using the confocal Raman probe. From Fig. 6.2b, it is also evident that the *in vivo* Raman spectra acquired using the confocal probe are spectrally remarkable distinct compared to the volume-typed probe (e.g., particularly at around 1302, 1445 and 1655 cm^{-1}), indicating that the information content interrogated is exceedingly distinct between these two Raman probes.

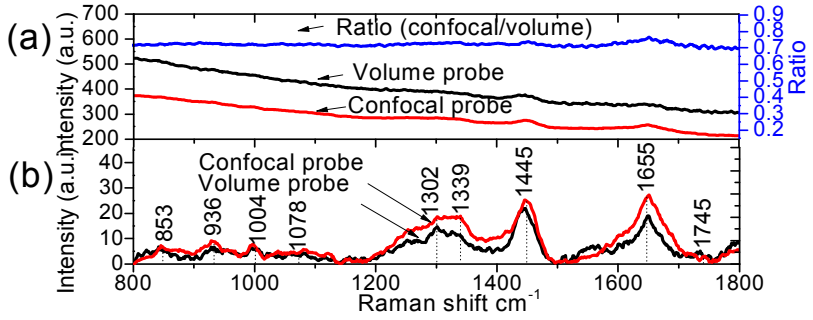

Fig. 6.2 (a) Comparison of mean *in vivo* raw spectra (Raman superimposed on AF) acquired from the distal esophagus using the confocal Raman probe (n=7) and volume-typed Raman probe (n=7) with 0.5 s integration time. The blue colored curve is the ratio spectrum (i.e., the confocal Raman spectrum divided by the Raman spectrum acquired by volume-typed Raman probe). (b) Comparison of AF background-subtracted tissue Raman spectra acquired by confocal and volume-typed Raman probes.

We have also compared the performance of confocal endoscopic probe and volume-typed Raman probe for improving tissue Raman to AF background ratios among different organs and anatomical sites (e.g., buccal, ventral tongue, distal esophagus and gastric) which show intense tissue AF under 785 nm laser excitation. Fig. 6.3 shows the bar diagrams of ±1 standard deviations (SD) of the tissue Raman to AF intensity ratios. The tissue Raman to AF ratios acquired using the confocal Raman probe are significantly higher ($p<0.05$) than those using the volume-typed Raman

probe among different organ sites. This confirms that NIR AF interference predominantly associates with deeper layered tissue can be effectively removed using the confocal Raman probe.

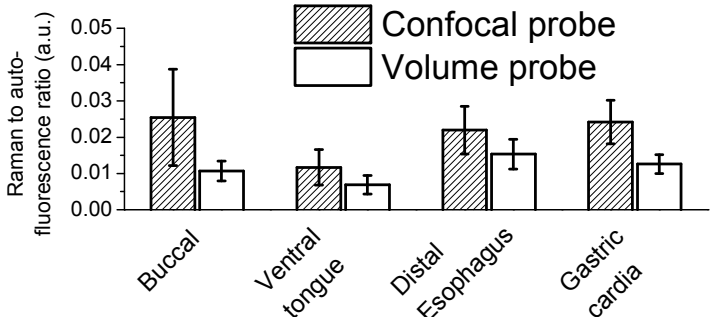

Fig. 6.3 Bar diagrams ±1 standard deviations (SD) showing the Raman to AF ratios of different internal organs and anatomical tissue sites (i.e., buccal, ventral tongue, distal esophagus and gastric) using confocal and volume-typed Raman probes.

In summary, these preliminary results from *in vivo* measurements in two-layer model tissue (e.g., buccal, gastric) have revealed that fiber-optic confocal Raman endoscopic probe coupled with a ball-lens may be of great potential for implementing as an effective diagnostic tool at endoscopy for enhancing epithelial tissue Raman measurements, which may ultimately further improve early diagnosis and detection of precancer and early cancer in internal organs at clinical endoscopy.

2) Development of on-line biomedical spectral diagnostic framework and optimizing the diagnostic model by employing other multivariate statistic techniques

We have implemented the multimodal spectroscopy for real-time tissue measurements but most of the current spectroscopic analyses have been limited to off-line post processing for classification of spectra with cross-validation procedures, which render practical limitations including the setting of exposure times, post-verification of spectrum quality, lack of automatic feedback mechanisms to clinicians for implementation of straightforward probabilistic diagnostics in clinical settings.

Hence, fully automated tissue spectral quality verification and real-time tissue cancer diagnostics are vital to translating the Raman spectroscopic diagnostic technique into practical clinical endoscopic routine. As such, we aim to develop an on-line biomedical spectral diagnostic framework integrated with image-guided endoscopy for real-time probabilistic detection of cancer in the head and neck. We also aim to validate the efficacy of this on-line framework developed for prospective prediction of patients with malignancies at clinical endoscopy.

Furthermore, in our study, PCA-LDA was mainly applied for developing diagnostic algorithms for disease identification. However, there exist other multivariate statistic techniques which have been used for developing classification functions, such as support vector machine (SVM), adaptive boosting (Ada Boost), artificial neural network (ANN), partial least-square discriminate analysis (PLS-DA) and genetic algorithm (GA) [240-253]. Therefore, choose one or several of these multivariate statistic techniques for specific organs/tissues as an appropriate algorithm to optimize the diagnosis may be another meaningful research. For now, we have planned to integrate more algorithms such as cluster analysis, ant colony optimization (ACO), adaptive boosting (Ada Boost) and genetic algorithm (GA) into current programs for optimizing analytical model for *in vivo* cancer diagnosis.

3) Develop the integrated wide-field imaging (NBI/AF/WLR) and point spectroscopy coupled with nonlinear optical (NLO) imaging techniques for improving tissue diagnosis and characterization at endoscopy

Nonlinear optical (NLO) imaging is a powerful optical technique that has found increasing use in the field of biomedical diagnostics. In NLO imaging, ultrafast laser excitation is used to exploit several nonlinear optical effects that can provide high-contrast imaging of biological samples. Commonly, NLO imaging modalities

include two- and three-photon fluorescence (2P & 3P), second and third-harmonic generation (SHG & THG), and coherent anti-stokes Raman scattering (CARS) or stimulated Raman scattering (SRS), which provide label-free, high spatial resolution and three-dimensional (3D) optical sectioning with high image contrast at the molecular level. Another advantage is the fact that the excitation wavelengths used for NLO imaging are preferred in the NIR ranges, which have much better penetration depths into biomedical tissue with no mutagenic effect/damage to tissue. Therefore, it will be of great clinical benefit to developing a hybrid NLO imaging technique (narrow-field imaging) with our developed endoscopic-based multimodal spectroscopy (AF/DR/Raman) and wide-field imaging as which can provide detailed information about tissue (morphology, vascularity, endogenous fluorophores (flavin, NADH, collagen, elastin) distributions, vibrational modes of biochemical and biomolecules, etc.) for further improving early disease diagnosis and characterization at the molecular, cellular and tissue levels.

List of Publications

Peer-Reviewed Journal Articles

1. **K. Lin**, D. L. P. Cheng, and Z. Huang, "Optical diagnosis of laryngeal cancer using high wavenumber Raman spectroscopy," Biosens. Bioelectron. 35, 213-217 (2012).
2. M. S. Bergholt, **K. Lin**, W. Zheng, D. P. C. Lau, and Z. Huang, "In vivo, real-time, transnasal, image-guided Raman endoscopy: defining spectral properties in the nasopharynx and larynx," J. Biomed. Opt. 17, 077002-077007 (2012).
3. M. S. Bergholt, W. Zheng, **K. Lin**, K. Y. Ho, M. Teh, K. G. Yeoh, J. B. So, and Z. Huang, "Combining near-infrared-excited autofluorescence and Raman spectroscopy improves in vivo diagnosis of gastric cancer," Biosens. Bioelectron. **26**, 4104-4110 (2011).
4. M. S. Bergholt, W. Zheng, **K. Lin**, K. Y. Ho, M. Teh, K. G. Yeoh, J. B. So, and Z. Huang, "In vivo diagnosis of esophageal cancer using image-guided Raman endoscopy and biomolecular modeling," Technology in cancer research & treatment **10**, 103-112 (2011).
5. M. S. Bergholt, W. Zheng, **K. Lin**, K. Y. Ho, M. Teh, K. G. Yeoh, J. B. Y. So, and Z. Huang, "Characterizing variability in in vivo Raman spectra of different anatomical locations in the upper gastrointestinal tract toward cancer detection," J. Biomed. Opt. **16**, 037003-037010 (2011).
6. M. S. Bergholt, W. Zheng, **K. Lin**, K. Y. Ho, M. Teh, K. G. Yeoh, J. B. Yan So, and Z. Huang, "In vivo diagnosis of gastric cancer using Raman endoscopy and ant colony optimization techniques," Int. J. Cancer **128**, 2673-2680 (2011).
7. M. S. Bergholt, W. Zheng, **K. Lin**, K. Y. Ho, M. Teh, K. G. Yeoh, J. B. Yan So, and Z. Huang, "Raman endoscopy for in vivo differentiation between benign and malignant ulcers in the stomach," Analyst **135**, 3162-3168 (2010).
8. Z. Huang, S. K. Teh, W. Zheng, **K. Lin**, K. Y. Ho, M. Teh, and K. G. Yeoh, "In vivo detection of epithelial neoplasia in the stomach using image-guided Raman endoscopy," Biosens. Bioelectron. **26**, 383-389 (2010).
9. **K. Lin**, W. Zheng, and Z. Huang, "Integrated autofluorescence endoscopic imaging and point-wise spectroscopy for real-time in vivo tissue measurements," J. Biomed. Opt. **15**, 040507-040503 (2010).
10. Z. Huang, M. S. Bergholt, W. Zheng, **K. Lin**, K. Y. Ho, M. Teh, and K. G. Yeoh, "In vivo early diagnosis of gastric dysplasia using narrow-band image-guided Raman endoscopy," J. Biomed. Opt. **15**, 037017-037015 (2010).
11. Z. Huang, S. K. Teh, W. Zheng, J. Mo, **K. Lin**, X. Shao, K. Y. Ho, M. Teh, and K. G. Yeoh, "Integrated Raman spectroscopy and trimodal wide-field imaging techniques for real-time in vivo tissue Raman measurements at endoscopy," Opt. Lett. **34**, 758-760 (2009).
12. **K. Lin**, D. L. P. Cheng, and Z. Huang, "Point-wise autofluorescence spectroscopy combined with diffuse reflectance spectroscopy for improving laryngeal cancer diagnosis," in preparation.

Conference Presentations

1. **K. Lin**, W. Zheng, S. Teh, D. Cheng and Z. Huang, “Endoscope-based autofluorescence imaging and spectroscopy system for cancer detection in head and neck,” in *Optics Within Life Science-10*, (Singapore, 2010).
2. **K. Lin**, W. Zheng, and Z. Huang, "Autofluorescence spectroscopy and imaging for cancer detection in the larynx," in *Communications and Photonics Conference and Exhibition (ACP), 2009 Asia*(2009), pp. 1-6.
3. **K. Lin**, W. Zheng, and Z. Huang, "Autofluorescence spectroscopic imaging for laryngeal cancer detection," T. Vo-Dinh, W. S. Grundfest, D. A. Benaron, and G. E. Cohn, eds. (SPIE, San Jose, CA, USA, 2008), pp. 68480G-68484.

References

1. A. Jemal, R. Siegel, J. Xu, and E. Ward, "Cancer Statistics, 2010," CA. Cancer J. Clin. 60, 277-300 (2010).
2. H. P. Lee, L. Chew, K. Y. Chow, A. Jin, E. Y. Loy, and H. William, "Trends in Cancer Incidence in Singapore, 2006-2010," (2010).
3. A. Forastiere, W. Koch, A. Trotti, and D. Sidransky, "Head and Neck Cancer," N. Engl. J. Med. 345, 1890-1900 (2001).
4. "Head and Neck Cancers," http://training.seer.cancer.gov/head-neck/anatomy/overview.html.
5. ShermannCDJr, "Cancer of the head and neck," in Manualof Clinical Oncology(1990), pp. 141-168.
6. A. J. M. Garcia, E. M. Ward, M. M. Center, Y. Hao, R. L. Siegel and M.J. Thun, "Global Cancer Facts & Figures 2007," Atlanta (GA): American Cancer Society, (2007).
7. A. R. Kreimer, G. M. Clifford, P. Boyle, and S. Franceschi, "Human Papillomavirus Types in Head and Neck Squamous Cell Carcinomas Worldwide: A Systematic Review," Cancer Epidemiology Biomarkers & Prevention 14, 467-475 (2005).
8. A. Jemal, F. Bray, M. M. Center, J. Ferlay, E. Ward, and D. Forman, "Global cancer statistics," CA. Cancer J. Clin. 61, 69-90 (2011).
9. L. Döbróssy, "Epidemiology of head and neck cancer: Magnitude of the problem," Cancer Metastasis Rev. 24, 9-17 (2005).
10. L. E. Loh, T. S. Chee, and A. B. John, "The anatomy of the Fossa of Rosenmuller--its possible influence on the detection of occult nasopharyngeal carcinoma," Singapore Med. J. 32, 154-155 (1991).
11. T. H. Gabor, Fundamentals of computerized tomography: Image reconstruction from projection, 2nd edition (Springer, 2009).
12. G. N. Hounsfield, "Computerized transverse axial scanning (tomography). 1. Description of system," Br. J. Radiol. 46, 1016-1022 (1973).
13. H. Schöder, H. W. D. Yeung, M. Gonen, D. Kraus, and S. M. Larson, "Head and Neck Cancer: Clinical Usefulness and Accuracy of PET/CT Image Fusion1," Radiology 231, 65-72 (2004).
14. H. D. Curtin, H. Ishwaran, A. A. Mancuso, R. W. Dalley, D. J. Caudry, and B. J. McNeil, "Comparison of CT and MR imaging in staging of neck metastases," Radiology 207, 123-130 (1998).
15. D. J. Brenner, and E. J. Hall, "Computed Tomography — An Increasing Source of Radiation Exposure," N. Engl. J. Med. 357, 2277-2284 (2007).
16. S. I. Ziegler, "Positron Emission Tomography: Principles, Technology, and Recent Developments," Nucl. Phys. A 752, 679-687 (2005).
17. L. K. Griffeth, "Use of PET/CT scanning in cancer patients: technical and practical considerations," Proceedings (Baylor University. Medical Center) 18, 321-330 (2005).
18. G. L. Brownell, C. A. Burnham, H. Jr, and D. E. Bohning, "Quantitative dynamic studies using short-lived radioisotopes and positron detection," in in Proceedings of the Symposium on Dynamic Studies with Radioisotopes in Medicine(1970), pp. 161-172.
19. J. S. Robertson, R. B. Marr, M. Rosenblum, V. Radeka, and Y. L. Yamamoto,

"32-CRYSTAL POSITRON TRANSVERSE SECTION DETECTOR," in Other Information: From Symposium on radionuclide tomography; New York, NY (15 Sep 1972). UNCL. Orig. Receipt Date: 30-JUN-73(1972), p. Medium: ED; Size: Pages: 24.

20. Z. H. CHO, ERIKSSON L., and CHAN J.K., "A circular ring transverse axial positron camera," in Reconstruction Tomography in Diagnostic Radiology and Nuclear Medicine, Ed. Ter-Pogossian MM., ed. (University Park Press: Baltimore, 1975).
21. "PET Scan: PET/CT History," http://www.petscaninfo.com/zportal/portals/phys/petct/history.
22. "Magnetic resonance imaging," http://en.wikipedia.org/wiki/Magnetic_resonance_imaging.
23. R. Acharya U, W. Yun, E. Ng, W. Yu, and J. Suri, "Imaging Systems of Human Eye: A Review," J. Med. Syst. 32, 301-315 (2008).
24. Y. Anzai, W. R. Carroll, D. J. Quint, C. R. Bradford, S. Minoshima, G. T. Wolf, and R. L. Wahl, "Recurrence of head and neck cancer after surgery or irradiation: prospective comparison of 2-deoxy-2-[F-18]fluoro-D-glucose PET and MR imaging diagnoses," Radiology 200, 135-141 (1996).
25. D. W. Tshering Vogel, P. Zbaeren, and H. C. Thoeny, "Cancer of the oral cavity and oropharynx," Cancer imaging : the official publication of the International Cancer Imaging Society 10, 62-72 (2010).
26. R. Shukla, W. M. Abidi, R. Richards-Kortum, and S. Anandasabapathy, "Endoscopic imaging: How far are we from real-time histology?," World journal of gastrointestinal endoscopy 3, 183-194 (2011).
27. G. Mastrangelo, E. Fadda, L. Cegolon, M. C. Montesco, I. Ray-Coquard, A. Buja, U. Fedeli, A. Frasson, P. Spolaore, and C. R. Rossi, "A European project on incidence, treatment, and outcome of sarcoma," BMC public health 10, 188 (2010).
28. T. Vo-Dinh, Biomedical photonics handbook (CRC Press, Boca Raton, Fla., 2003).
29. B. R. Haxel, M. Goetz, R. Kiesslich, and J. Gosepath, "Confocal endomicroscopy: a novel application for imaging of oral and oropharyngeal mucosa in human," Eur. Arch. Otorhinolaryngol. 267, 443-448 (2010).
30. W. C. Lin, A. Mahadevan-Jansen, M. D. Johnson, R. J. Weil, and S. A. Toms, "In vivo optical spectroscopy detects radiation damage in brain tissue," Neurosurgery 57, 518-525; discussion 518-525 (2005).
31. M. F. Parker, "Emerging technology in cervical cancer screening: spectroscopy," Clin. Obstet. Gynecol. 48, 209-217 (2005).
32. B. J. Tromberg, A. Cerussi, N. Shah, M. Compton, A. Durkin, D. Hsiang, J. Butler, and R. Mehta, "Imaging in breast cancer: diffuse optics in breast cancer: detecting tumors in pre-menopausal women and monitoring neoadjuvant chemotherapy," Breast cancer research : BCR 7, 279-285 (2005).
33. K. M. Blackmore, J. A. Knight, R. Jong, and L. Lilge, "Assessing breast tissue density by transillumination breast spectroscopy (TIBS): an intermediate indicator of cancer risk," Br. J. Radiol. 80, 545-556 (2007).
34. C. W. Kan, B. C. Jiang, L. T. Nieman, K. Sokolov, and M. K. Markey, "Comparison of linear and non-linear classifiers for oral cancer screening by optical spectroscopy," AMIA ... Annual Symposium proceedings / AMIA Symposium. AMIA Symposium, 1003 (2007).
35. S. G. El-Tawil, R. Adnan, Z. N. Muhamed, and N. H. Othman, "Comparative

study between Pap smear cytology and FTIR spectroscopy: a new tool for screening for cervical cancer," Pathology (Phila). 40, 600-603 (2008).
36. B. J. Tromberg, B. W. Pogue, K. D. Paulsen, A. G. Yodh, D. A. Boas, and A. E. Cerussi, "Assessing the future of diffuse optical imaging technologies for breast cancer management," Med. Phys. 35, 2443-2451 (2008).
37. W. Y. Cho, J. Y. Jang, and D. H. Lee, "Recent Advances in Image-enhanced Endoscopy," Clinical endoscopy 44, 65-75 (2011).
38. B. Kulapaditharom, and V. Boonkitticharoen, "Laser-induced fluorescence imaging in localization of head and neck cancers," Ann. Otol. Rhinol. Laryngol. 107, 241-246 (1998).
39. M. Zargi, I. Fajdiga, and L. Smid, "Autofluorescence imaging in the diagnosis of laryngeal cancer," Eur. Arch. Otorhinolaryngol. 257, 17-23 (2000).
40. R. Paczona, S. Temam, F. Janot, P. Marandas, and B. Luboinski, "Autofluorescence videoendoscopy for photodiagnosis of head and neck squamous cell carcinoma," Eur. Arch. Otorhinolaryngol. 260, 544-548 (2003).
41. Y. H. Wen, X. L. Zhu, W. B. Lei, Y. H. Zeng, Y. Q. Sun, and W. P. Wen, "Narrow-band imaging: a novel screening tool for early nasopharyngeal carcinoma," Arch. Otolaryngol. Head Neck Surg. 138, 183-188 (2012).
42. K. Gono, T. Obi, M. Yamaguchi, N. Ohyama, H. Machida, Y. Sano, S. Yoshida, Y. Hamamoto, and T. Endo, "Appearance of enhanced tissue features in narrow-band endoscopic imaging," J Biomed Opt 9, 568-577 (2004).
43. A. Watanabe, M. Taniguchi, H. Tsujie, M. Hosokawa, M. Fujita, and S. Sasaki, "The value of narrow band imaging endoscope for early head and neck cancers," Otolaryngol. Head Neck Surg. 138, 446-451 (2008).
44. C. Katada, M. Nakayama, S. Tanabe, A. Naruke, W. Koizumi, T. Masaki, M. Okamoto, and K. Saigenji, "Narrow band imaging for detecting superficial oral squamous cell carcinoma: a report of two cases," Laryngoscope 117, 1596-1599 (2007).
45. Y. C. Lin, and W. H. Wang, "Narrow-band imaging for detecting early recurrent nasopharyngeal carcinoma," Head Neck 33, 591-594 (2011).
46. A. Watanabe, M. Taniguchi, H. Tsujie, M. Hosokawa, M. Fujita, and S. Sasaki, "The value of narrow band imaging for early detection of laryngeal cancer," Eur. Arch. Otorhinolaryngol. 266, 1017-1023 (2009).
47. M. Muto, M. Nakane, C. Katada, Y. Sano, A. Ohtsu, H. Esumi, S. Ebihara, and S. Yoshida, "Squamous cell carcinoma in situ at oropharyngeal and hypopharyngeal mucosal sites," Cancer 101, 1375-1381 (2004).
48. A. Watanabe, H. Tsujie, M. Taniguchi, M. Hosokawa, M. Fujita, and S. Sasaki, "Laryngoscopic detection of pharyngeal carcinoma in situ with narrowband imaging," Laryngoscope 116, 650-654 (2006).
49. D. Huang, E. A. Swanson, C. P. Lin, J. S. Schuman, W. G. Stinson, W. Chang, M. R. Hee, T. Flotte, K. Gregory, C. A. Puliafito, and et al., "Optical coherence tomography," Science 254, 1178-1181 (1991).
50. J. G. Fujimoto, M. E. Brezinski, G. J. Tearney, S. A. Boppart, B. Bouma, M. R. Hee, J. F. Southern, and E. A. Swanson, "Optical biopsy and imaging using optical coherence tomography," Nat. Med. 1, 970-972 (1995).
51. M. Rubinstein, P. Schalch, M. Di Silvio, M. A. Betancourt, and B. J. Wong, "[Optical coherence tomography applications in otolaryngology]," Acta Otorrinolaringol. Esp. 60, 357-363 (2009).
52. A. Sergeev, V. Gelikonov, G. Gelikonov, F. Feldchtein, R. Kuranov, N. Gladkova, N. Shakhova, L. Snopova, A. Shakhov, I. Kuznetzova, A.

Denisenko, V. Pochinko, Y. Chumakov, and O. Streltzova, "In vivo endoscopic OCT imaging of precancerand cancer states of human mucosa," Opt. Express 1, 432-440 (1997).
53. O. R. Hughes, N. Stone, M. Kraft, C. Arens, and M. A. Birchall, "Optical and molecular techniques to identify tumor margins within the larynx," Head Neck 32, 1544-1553 (2010).
54. S. F. Chen, C. W. Lu, M. T. Tsai, Y. M. Wang, C. Yang, and C. P. Chiang, "Oral cancer diagnosis with optical coherence tomography," Conference proceedings : ... Annual International Conference of the IEEE Engineering in Medicine and Biology Society. IEEE Engineering in Medicine and Biology Society. Conference 7, 7227-7229 (2005).
55. M. T. Tsai, H. C. Lee, C. K. Lee, C. H. Yu, H. M. Chen, C. P. Chiang, C. C. Chang, Y. M. Wang, and C. C. Yang, "Effective indicators for diagnosis of oral cancer using optical coherence tomography," Opt Express 16, 15847-15862 (2008).
56. J. M. Ridgway, W. B. Armstrong, S. Guo, U. Mahmood, J. Su, R. P. Jackson, T. Shibuya, R. L. Crumley, M. Gu, Z. Chen, and B. J. Wong, "In vivo optical coherence tomography of the human oral cavity and oropharynx," Arch. Otolaryngol. Head Neck Surg. 132, 1074-1081 (2006).
57. H. Kawakami-Wong, S. Gu, M. J. Hammer-Wilson, J. B. Epstein, Z. Chen, and P. Wilder-Smith, "In vivo optical coherence tomography-based scoring of oral mucositis in human subjects: a pilot study," J Biomed Opt 12, 051702 (2007).
58. A. L. Polglase, W. J. McLaren, S. A. Skinner, R. Kiesslich, M. F. Neurath, and P. M. Delaney, "A fluorescence confocal endomicroscope for in vivo microscopy of the upper- and the lower-GI tract," Gastrointest. Endosc. 62, 686-695 (2005).
59. R. Kiesslich, M. Goetz, and M. F. Neurath, "Confocal laser endomicroscopy for gastrointestinal diseases," Gastrointest. Endosc. Clin. N. Am. 18, 451-466, viii (2008).
60. M. Goetz, A. Watson, and R. Kiesslich, "Confocal laser endomicroscopy in gastrointestinal diseases," J Biophotonics 4, 498-508 (2011).
61. F. Koenig, S. Gonzalez, W. M. White, M. Lein, and M. Rajadhyaksha, "Near-infrared confocal laser scanning microscopy of bladder tissue in vivo," Urology 53, 853-857 (1999).
62. A. O. Gerstner, "Early detection in head and neck cancer - current state and future perspectives," GMS current topics in otorhinolaryngology, head and neck surgery 7, Doc06 (2008).
63. R. Kiesslich, J. Burg, M. Vieth, J. Gnaendiger, M. Enders, P. Delaney, A. Polglase, W. McLaren, D. Janell, S. Thomas, B. Nafe, P. R. Galle, and M. F. Neurath, "Confocal laser endoscopy for diagnosing intraepithelial neoplasias and colorectal cancer in vivo," Gastroenterology 127, 706-713 (2004).
64. R. Kiesslich, M. Goetz, J. Burg, M. Stolte, E. Siegel, M. J. Maeurer, S. Thomas, D. Strand, P. R. Galle, and M. F. Neurath, "Diagnosing Helicobacter pylori in vivo by confocal laser endoscopy," Gastroenterology 128, 2119-2123 (2005).
65. M. Goetz, A. Hoffman, P. R. Galle, M. F. Neurath, and R. Kiesslich, "Confocal laser endoscopy: new approach to the early diagnosis of tumors of the esophagus and stomach," Future Oncol 2, 469-476 (2006).
66. R. Kiesslich, A. Hoffman, M. Goetz, S. Biesterfeld, M. Vieth, P. R. Galle, and

M. F. Neurath, "In vivo diagnosis of collagenous colitis by confocal endomicroscopy," Gut 55, 591-592 (2006).
67. K. Deinert, R. Kiesslich, M. Vieth, M. F. Neurath, and H. Neuhaus, "In-vivo microvascular imaging of early squamous-cell cancer of the esophagus by confocal laser endomicroscopy," Endoscopy 39, 366-368 (2007).
68. O. Pech, T. Rabenstein, H. Manner, M. C. Petrone, J. Pohl, M. Vieth, M. Stolte, and C. Ell, "Confocal laser endomicroscopy for in vivo diagnosis of early squamous cell carcinoma in the esophagus," Clinical gastroenterology and hepatology : the official clinical practice journal of the American Gastroenterological Association 6, 89-94 (2008).
69. T. Just, J. Stave, C. Boltze, A. Wree, B. Kramp, R. F. Guthoff, and H. W. Pau, "Laser scanning microscopy of the human larynx mucosa: a preliminary, ex vivo study," Laryngoscope 116, 1136-1141 (2006).
70. P. S.-P. Thong, M. Olivo, K.-W. Kho, W. Zheng, K. Mancer, M. Harris, and K.-C. Soo, "Laser confocal endomicroscopy as a novel technique for fluorescence diagnostic imaging of the oral cavity," J. Biomed. Opt. 12, 014007-014008 (2007).
71. E. B. Hanlon, R. Manoharan, T. W. Koo, K. E. Shafer, J. T. Motz, M. Fitzmaurice, J. R. Kramer, I. Itzkan, R. R. Dasari, and M. S. Feld, "Prospects for in vivo Raman spectroscopy," Phys. Med. Biol. 45, R1-R59 (2000).
72. "Diffuse reflection," http://en.wikipedia.org/wiki/Diffuse_reflection.
73. P. Diagaradjane, P. Mohindra, and S. Krishnan, "Theranostic Applications of Gold Nanoparticles in Cancer," in Nanoplatform-Based Molecular Imaging(John Wiley & Sons, Inc., 2011), pp. 639-657.
74. M. Cope, D. T. Delpy, E. O. Reynolds, S. Wray, J. Wyatt, and P. van der Zee, "Methods of quantitating cerebral near infrared spectroscopy data," Adv. Exp. Med. Biol. 222, 183-189 (1988).
75. E. N. Marieb, Human anatomy and physiology / Elaine N. Marieb (Benjamin/Cummings, 1995).
76. G. M. Hale, and M. R. Querry, "Optical Constants of Water in the 200-nm to 200-microm Wavelength Region," Appl Opt 12, 555-563 (1973).
77. T. Valery, "Light-Tissue Interactions," in Biomedical Photonics Handbook(CRC Press, 2003).
78. Lakowicz, and J. R, eds. Principles of Fluorescence Spectroscopy (2006).
79. P. K. Sharma, R. Nass, and H. Schmidt, "Effect of solvent, host precursor, dopant concentration and crystallite size on the fluorescence properties of Eu(III) doped yttria," Optical Materials 10, 161-169 (1998).
80. R. Richards-Kortum, and E. Sevick-Muraca, "Quantitative optical spectroscopy for tissue diagnosis," Annu. Rev. Phys. Chem. 47, 555-606 (1996).
81. M.-A. Mycek, and B. W. Pogue, Handbook of biomedical fluorescence (Marcel Dekker, New York, 2003).
82. "Fluorescence," http://en.wikipedia.org/wiki/Fluorescence.
83. M. Monici, "Cell and tissue autofluorescence research and diagnostic applications," in Biotechnol. Annu. Rev., M. R. El-Gewely, ed. (Elsevier, 2005), pp. 227-256.
84. G. A. Wagnieres, W. M. Star, and B. C. Wilson, "In vivo fluorescence spectroscopy and imaging for oncological applications," Photochem. Photobiol. 68, 603-632 (1998).
85. S. V. Patwardhan, W. J. Akers, and S. Bloch, "Fluorescence Molecular

Imaging: Microscopic to Macroscopic," in Principles And Advanced Methods In Medical Imaging And Image Analysis, pp. 311-336.
86. Y. Wu, P. Xi, J. Qu, T.-H. Cheung, and M.-Y. Yu, "Depth-resolved fluorescence spectroscopy reveals layered structure of tissue," Opt. Express 12, 3218-3223 (2004).
87. H. Puchtler, F. S. Waldrop, and L. S. Valentine, "Fluorescence microscopic distinction between elastin and collagen," Histochemistry and Cell Biology 35, 17-30 (1973).
88. R. S. Sohal, "Assay of lipofuscin/ceroid pigment in vivo during aging," Methods Enzymol. 105, 484-487 (1984).
89. W. R. Dillon, and M. Goldstein, Multivariate analysis: methods and applications (John Wiley and Sons: New York, 1984).
90. R. L. McCreery, Raman spectroscopy for chemical analysis (John Wiley & Sons, New York, 2000).
91. B. C. W. Ralph S. DaCosta, Norman E. Marcon,, "Photodiagnostic techniques for the endoscopic detection of premalignant gastrointestinal lesions," Digestive Endoscopy 15, 153-173 (2003).
92. K. Vishwanath, K. Chang, D. Klein, Y. F. Deng, V. Chang, J. E. Phelps, and N. Ramanujam, "Portable, Fiber-Based, Diffuse Reflection Spectroscopy (DRS) Systems for Estimating Tissue Optical Properties," Appl Spectrosc 62, 206-215 (2011).
93. A. Amelink, O. P. Kaspers, H. J. C. M. Sterenborg, J. E. van der Wal, J. L. N. Roodenburg, and M. J. H. Witjes, "Non-invasive measurement of the morphology and physiology of oral mucosa by use of optical spectroscopy," Oral Oncol. 44, 65-71 (2008).
94. R. Mallia, S. S. Thomas, A. Mathews, R. Kumar, P. Sebastian, J. Madhavan, and N. Subhash, "Oxygenated hemoglobin diffuse reflectance ratio for in vivo detection of oral pre-cancer," J Biomed Opt 13, 041306 (2008).
95. D. C. de Veld, M. Skurichina, M. J. Witjes, R. P. Duin, H. J. Sterenborg, and J. L. Roodenburg, "Autofluorescence and diffuse reflectance spectroscopy for oral oncology," Lasers Surg. Med. 36, 356-364 (2005).
96. F. W. Leung, "Endoscopic reflectance spectrophotometry and visible light spectroscopy in clinical gastrointestinal studies," Dig. Dis. Sci. 53, 1669-1677 (2008).
97. M. D. Keller, S. K. Majumder, M. C. Kelley, I. M. Meszoely, F. I. Boulos, G. M. Olivares, and A. Mahadevan-Jansen, "Autofluorescence and diffuse reflectance spectroscopy and spectral imaging for breast surgical margin analysis," Lasers Surg. Med. 42, 15-23 (2010).
98. N. Lue, J. W. Kang, C. C. Yu, I. Barman, N. C. Dingari, M. S. Feld, R. R. Dasari, and M. Fitzmaurice, "Portable optical fiber probe-based spectroscopic scanner for rapid cancer diagnosis: a new tool for intraoperative margin assessment," PloS one 7, e30887 (2012).
99. K. Yan, Y. Yu, E. Tinney, R. Baraldi, and L. Liao, "Clinical study of a non-invasive multimodal sono-contrast induced spectroscopy system for breast cancer diagnosis," Med. Phys. 39, 1571-1578 (2012).
100. M. A. Suhr, C. Hopper, L. Jones, J. G. George, S. G. Bown, and A. J. MacRobert, "Optical biopsy systems for the diagnosis and monitoring of superficial cancer and precancer," Int. J. Oral Maxillofac. Surg. 29, 453-457 (2000).
101. R. J. Nordstrom, L. Burke, J. M. Niloff, and J. F. Myrtle, "Identification of

cervical intraepithelial neoplasia (CIN) using UV-excited fluorescence and diffuse-reflectance tissue spectroscopy," Lasers Surg. Med. 29, 118-127 (2001).
102. V. T. Chang, P. S. Cartwright, S. M. Bean, G. M. Palmer, R. C. Bentley, and N. Ramanujam, "Quantitative physiology of the precancerous cervix in vivo through optical spectroscopy," Neoplasia (New York, N.Y.) 11, 325-332 (2009).
103. R. Alfano, D. Tata, J. Cordero, P. Tomashefsky, F. Longo, and M. Alfano, "Laser induced fluorescence spectroscopy from native cancerous and normal tissue," Quantum Electronics, IEEE Journal of 20, 1507-1511 (1984).
104. A. Gillenwater, R. Jacob, R. Ganeshappa, B. Kemp, A. K. El-Naggar, J. L. Palmer, G. Clayman, M. F. Mitchell, and R. Richards-Kortum, "Non-invasive diagnosis of oral neoplasia based on fluorescence spectroscopy and native tissue autofluorescence," Arch. Otolaryngol. Head Neck Surg. 124, 1251-1258 (1998).
105. D. R. Ingrams, J. K. Dhingra, K. Roy, D. F. Perrault, I. D. Bottrill, S. Kabani, E. E. Rebeiz, M. M. Pankratov, S. M. Shapshay, R. Manoharan, I. Itzkan, and M. S. Feld, "Autofluorescence characteristics of oral mucosa," Head Neck 19, 27-32 (1997).
106. C. S. Betz, M. Mehlmann, K. Rick, H. Stepp, G. Grevers, R. Baumgartner, and A. Leunig, "Autofluorescence imaging and spectroscopy of normal and malignant mucosa in patients with head and neck cancer," Lasers Surg. Med. 25, 323-334 (1999).
107. S. K. Majumder, S. K. Mohanty, N. Ghosh, P. K. Gupta, D. K. Jain, and F. Khan, "A pilot study on the use of autofluorescence spectroscopy for diagnosis of the cancer of human oral cavity," Curr. Sci. 79, 1089-1094 (2000).
108. S. K. Majumder, N. Ghosh, S. Kataria, and P. K. Gupta, "Nonlinear pattern recognition for laser-induced fluorescence diagnosis of cancer," Lasers Surg. Med. 33, 48-56 (2003).
109. D. C. G. d. Veld, M. Skurichina, M. J. H. Witjes, R. P. W. Duin, D. J. C. M. Sterenborg, W. M. Star, and J. L. N. Roodenburg, "Autofluorescence characteristics of healthy oral mucosa at different anatomical sites," Lasers Surg. Med. 32, 367-376 (2003).
110. M. G. Muller, T. A. Valdez, I. Georgakoudi, V. Backman, C. Fuentes, S. Kabani, N. Laver, Z. Wang, C. W. Boone, R. R. Dasari, S. M. Shapshay, and M. S. Feld, "Spectroscopic detection and evaluation of morphologic and biochemical changes in early human oral carcinoma," Cancer 97, 1681-1692 (2003).
111. J. Y. Qu, P. Wing, Z. Huang, D. Kwong, J. Sham, S. L. Lee, W. K. Ho, and W. I. Wei, "Preliminary study of in vivo autofluorescence of nasopharyngeal carcinoma and normal tissue," Lasers Surg. Med. 26, 432-440 (2000).
112. H. Chang, J. Y. Qu, P. Yuen, J. Sham, D. Kwong, and W. I. Wei, "Light-Induced Autofluorescence Spectroscopy for Detection of Nasopharyngeal Carcinoma in Vivo," Appl. Spectrosc. 56, 1361-1367 (2002).
113. C. Eker, R. Rydell, K. Svanberg, and S. Andersson-Engels, "Multivariate analysis of laryngeal fluorescence spectra recorded in vivo," Lasers Surg. Med. 28, 259-266 (2001).
114. C. Arens, D. Reußner, H. Neubacher, J. Woenckhaus, and H. Glanz, "Spectrometric measurement in laryngeal cancer," Eur. Arch. Otorhinolaryngol. 263, 1001-1007 (2006).
115. M. J. D. P. J. Farwell D, and et al., "Time-resolved fluorescence spectroscopy

as a diagnostic technique of oral carcinoma: Validation in the hamster buccal pouch model," Archives of Otolaryngology—Head & Neck Surgery 136, 126-133 (2010).
116. J. D. Meier, H. Xie, Y. Sun, Y. Sun, N. Hatami, B. Poirier, L. Marcu, and D. G. Farwell, "Time-resolved laser-induced fluorescence spectroscopy as a diagnostic instrument in head and neck carcinoma," Otolaryngology -- Head and Neck Surgery 142, 838-844 (2010).
117. M. G. Shim, L. M. Song, N. E. Marcon, and B. C. Wilson, "In vivo near-infrared Raman spectroscopy: demonstration of feasibility during clinical gastrointestinal endoscopy," Photochem. Photobiol. 72, 146-150 (2000).
118. N. Stone, C. Kendall, J. Smith, P. Crow, and H. Barr, "Raman spectroscopy for identification of epithelial cancers," Faraday Discuss. 126, 141-157; discussion 169-183 (2004).
119. L. M. Almond, J. Hutchings, N. Shepherd, H. Barr, N. Stone, and C. Kendall, "Raman spectroscopy: a potential tool for early objective diagnosis of neoplasia in the oesophagus," J Biophotonics 4, 685-695 (2011).
120. E. Widjaja, W. Zheng, and Z. Huang, "Classification of colonic tissues using near-infrared Raman spectroscopy and support vector machines," Int. J. Oncol. 32, 653-662 (2008).
121. C. Kendall, N. Stone, N. Shepherd, K. Geboes, B. Warren, R. Bennett, and H. Barr, "Raman spectroscopy, a potential tool for the objective identification and classification of neoplasia in Barrett's oesophagus," J. Pathol. 200, 602-609 (2003).
122. L.-M. W. K. Song, A. Molckovsky, K. K. Wang, L. J. Burgart, B. Dolenko, R. L. Somorjai, and B. C. Wilson, "Diagnostic potential of Raman spectroscopy in Barrett's esophagus," T. Vo-Dinh, W. S. Grundfest, D. A. Benaron, and G. E. Cohn, eds. (SPIE, San Jose, CA, USA, 2005), pp. 140-146.
123. I. A. Boere, T. C. Bakker Schut, J. van den Boogert, R. W. F. de Bruin, and G. J. Puppels, "Use of fibre optic probes for detection of Barrett's epithelium in the rat oesophagus by Raman spectroscopy," Vib. Spectrosc 32, 47-55 (2003).
124. M. S. Bergholt, W. Zheng, K. Lin, K. Y. Ho, M. Teh, K. G. Yeoh, J. B. Y. So, and Z. Huang, "Characterizing variability in in vivo Raman spectra of different anatomical locations in the upper gastrointestinal tract toward cancer detection," J. Biomed. Opt. 16, 037003-037010 (2011).
125. M. S. Bergholt, W. Zheng, K. Lin, K. Y. Ho, M. Teh, K. G. Yeoh, J. B. So, and Z. Huang, "In vivo diagnosis of esophageal cancer using image-guided Raman endoscopy and biomolecular modeling," Technology in cancer research & treatment 10, 103-112 (2011).
126. Z. Huang, M. S. Bergholt, W. Zheng, K. Lin, K. Y. Ho, M. Teh, and K. G. Yeoh, "In vivo early diagnosis of gastric dysplasia using narrow-band image-guided Raman endoscopy," J. Biomed. Opt. 15, 037017-037015 (2010).
127. K. Guze, M. Short, S. Sonis, N. Karimbux, J. Chan, and H. Zeng, "Parameters defining the potential applicability of Raman spectroscopy as a diagnostic tool for oral disease," J. Biomed. Opt. 14, 014016-014019 (2009).
128. A. T. Harris, A. Rennie, H. Waqar-Uddin, S. R. Wheatley, S. K. Ghosh, D. P. Martin-Hirsch, S. E. Fisher, A. S. High, J. Kirkham, and T. Upile, "Raman spectroscopy in head and neck cancer," Head Neck Oncol 2, 26 (2010).
129. D. P. Lau, Z. Huang, H. Lui, C. S. Man, K. Berean, M. D. Morrison, and H. Zeng, "Raman spectroscopy for optical diagnosis in normal and cancerous tissue of the nasopharynx—preliminary findings," Lasers Surg. Med. 32, 210-

214 (2003).
130. D. P. Lau, Z. Huang, H. Lui, D. W. Anderson, K. Berean, M. D. Morrison, L. Shen, and H. Zeng, "Raman spectroscopy for optical diagnosis in the larynx: preliminary findings," Lasers Surg. Med. 37, 192-200 (2005).
131. S. K. Teh, W. Zheng, D. P. Lau, and Z. Huang, "Spectroscopic diagnosis of laryngeal carcinoma using near-infrared Raman spectroscopy and random recursive partitioning ensemble techniques," Analyst 134, 1232-1239 (2009).
132. S. K. Teh, W. Zheng, D. P. Lau, and Z. Huang, "Spectroscopic diagnosis of laryngeal carcinoma using near-infrared Raman spectroscopy and random recursive partitioning ensemble techniques," Analyst 134, 1232-1239 (2009).
133. N. Stone, P. Stavroulaki, C. Kendall, M. Birchall, and H. Barr, "Raman spectroscopy for early detection of laryngeal malignancy: preliminary results," Laryngoscope 110, 1756-1763 (2000).
134. Z. Huang, A. McWilliams, H. Lui, D. I. McLean, S. Lam, and H. Zeng, "Near-infrared Raman spectroscopy for optical diagnosis of lung cancer," Int. J. Cancer 107, 1047-1052 (2003).
135. A. Mahadevan-Jansen, M. F. Mitchell, N. Ramanujam, A. Malpica, S. Thomsen, U. Utzinger, and R. Richards-Kortum, "Near-infrared Raman spectroscopy for in vitro detection of cervical precancers," Photochem. Photobiol. 68, 123-132 (1998).
136. J. Mo, W. Zheng, J. J. Low, J. Ng, A. Ilancheran, and Z. Huang, "High wavenumber Raman spectroscopy for in vivo detection of cervical dysplasia," Anal. Chem. 81, 8908-8915 (2009).
137. R. O. Draga, M. C. Grimbergen, P. L. Vijverberg, C. F. van Swol, T. G. Jonges, J. A. Kummer, and J. L. Ruud Bosch, "In vivo bladder cancer diagnosis by high-volume Raman spectroscopy," Anal. Chem. 82, 5993-5999 (2010).
138. M. A. Short, H. Lui, D. McLean, H. Zeng, A. Alajlan, and X. K. Chen, "Changes in nuclei and peritumoral collagen within nodular basal cell carcinomas via confocal micro-Raman spectroscopy," J Biomed Opt 11, 34004 (2006).
139. K. E. Shafer-Peltier, A. S. Haka, M. Fitzmaurice, J. Crowe, J. Myles, R. R. Dasari, and M. S. Feld, "Raman microspectroscopic model of human breast tissue: implications for breast cancer diagnosis in vivo," Journal of Raman Spectroscopy 33, 552-563 (2002).
140. A. S. Haka, Z. Volynskaya, J. A. Gardecki, J. Nazemi, J. Lyons, D. Hicks, M. Fitzmaurice, R. R. Dasari, J. P. Crowe, and M. S. Feld, "In vivo Margin Assessment during Partial Mastectomy Breast Surgery Using Raman Spectroscopy[?Q1: Running head: Raman Margin Assessment at Partial Mastectomy. Short title OK?Q1]," Cancer Res. 66, 3317-3322 (2006).
141. T. Upile, W. Jerjes, H. Sterenborg, A. El-Naggar, A. Sandison, M. Witjes, M. Biel, I. Bigio, B. Wong, A. Gillenwater, A. MacRobert, D. Robinson, C. Betz, H. Stepp, L. Bolotine, G. McKenzie, C. Mosse, H. Barr, Z. Chen, K. Berg, A. D'Cruz, N. Stone, C. Kendall, S. Fisher, A. Leunig, M. Olivo, R. Richards-Kortum, K. Soo, V. Bagnato, and L.-P. Choo-Smith, "Head & neck optical diagnostics: vision of the future of surgery," Head & Neck Oncology 1, 25 (2009).
142. R. Malini, K. Venkatakrishna, J. Kurien, K. M. Pai, L. Rao, V. B. Kartha, and C. M. Krishna, "Discrimination of normal, inflammatory, premalignant, and malignant oral tissue: A Raman spectroscopy study," Biopolymers 81, 179-193 (2006).

143. A. P. Oliveira, R. A. Bitar, L. Silveira, R. A. Zangaro, and A. A. Martin, "Near-infrared Raman spectroscopy for oral carcinoma diagnosis," Photomedicine and laser surgery 24, 348-353 (2006).
144. Z. Huang, S. K. Teh, W. Zheng, J. Mo, K. Lin, X. Shao, K. Y. Ho, M. Teh, and K. G. Yeoh, "Integrated Raman spectroscopy and trimodal wide-field imaging techniques for real-time in vivo tissue Raman measurements at endoscopy," Opt. Lett. 34, 758-760 (2009).
145. A. Harris, A. Lungari, C. Needham, S. Smith, M. Lones, S. Fisher, X. Yang, N. Cooper, J. Kirkham, D. A. Smith, D. Martin-Hirsch, and A. High, "Potential for Raman spectroscopy to provide cancer screening using a peripheral blood sample," Head & Neck Oncology 1, 34 (2009).
146. T. W. Anderson, An introduction to multivariate statistical analysis (Wiley-Interscience, Hoboken, N.J., 2003).
147. X. Shao, W. Zheng, and Z. Huang, "Near-infrared autofluorescence spectroscopy for in vivo identification of hyperplastic and adenomatous polyps in the colon," Biosens. Bioelectron. 30, 118-122 (2011).
148. A. Zwielly, S. Mordechai, I. Sinielnikov, A. Salman, E. Bogomolny, and S. Argov, "Advanced statistical techniques applied to comprehensive FTIR spectra on human colonic tissues," Med. Phys. 37, 1047-1055 (2010).
149. M. C. Grimbergen, C. F. van Swol, R. J. van Moorselaar, J. Uff, A. Mahadevan-Jansen, and N. Stone, "Raman spectroscopy of bladder tissue in the presence of 5-aminolevulinic acid," J. Photochem. Photobiol. B. 95, 170-176 (2009).
150. S. K. Teh, W. Zheng, K. Y. Ho, M. Teh, K. G. Yeoh, and Z. Huang, "Diagnostic potential of near-infrared Raman spectroscopy in the stomach: differentiating dysplasia from normal tissue," Br. J. Cancer 98, 457-465 (2008).
151. Z. Huang, H. Lui, D. I. McLean, M. Korbelik, and H. Zeng, "Raman spectroscopy in combination with background near-infrared autofluorescence enhances the in vivo assessment of malignant tissues," Photochem. Photobiol. 81, 1219-1226 (2005).
152. H. Gu, Z. Pan, B. Xi, V. Asiago, B. Musselman, and D. Raftery, "Principal component directed partial least squares analysis for combining nuclear magnetic resonance and mass spectrometry data in metabolomics: application to the detection of breast cancer," Anal. Chim. Acta 686, 57-63 (2011).
153. Y. Yamakoshi, M. Ogawa, T. Yamakoshi, T. Tamura, and K. Yamakoshi, "Multivariate regression and discreminant calibration models for a novel optical non-invasive blood glucose measurement method named pulse glucometry," Conference proceedings : ... Annual International Conference of the IEEE Engineering in Medicine and Biology Society. IEEE Engineering in Medicine and Biology Society. Conference 2009, 126-129 (2009).
154. C. Y. Wang, T. Tsai, H. M. Chen, C. T. Chen, and C. P. Chiang, "PLS-ANN based classification model for oral submucous fibrosis and oral carcinogenesis," Lasers Surg. Med. 32, 318-326 (2003).
155. A. D. Ghanate, S. Kothiwale, S. P. Singh, D. Bertrand, and C. M. Krishna, "Comparative evaluation of spectroscopic models using different multivariate statistical tools in a multicancer scenario," J Biomed Opt 16, 025003 (2011).
156. T. C. Bakker Schut, M. J. Witjes, H. J. Sterenborg, O. C. Speelman, J. L. Roodenburg, E. T. Marple, H. A. Bruining, and G. J. Puppels, "In vivo detection of dysplastic tissue by Raman spectroscopy," Anal. Chem. 72, 6010-6018 (2000).

157. M. S. Bergholt, W. Zheng, K. Lin, K. Y. Ho, M. Teh, K. G. Yeoh, J. B. So, and Z. Huang, "Combining near-infrared-excited autofluorescence and Raman spectroscopy improves in vivo diagnosis of gastric cancer," Biosens. Bioelectron. 26, 4104-4110 (2011).
158. "Principal component analysis," http://en.wikipedia.org/wiki/Principal_component_analysis.
159. Zwick, and Velicer, "Comparison of five rules for determining the number of components to retain," Psych. Bull. v99, 432-442 (1986).
160. Z. V. Lambert, A. R. Wildt, and R. M. Durand, "Assessing Sampling Variation Relative to Number-of-Factors Criteria," Educational and Psychological Measurement 50, 33-48 (1990).
161. B. Mertens, M. Thompson, and T. Fearn, "Principal component outlier detection and SIMCA: a synthesis," Analyst 119, 2777-2784 (1994).
162. P. J. de Groot, G. J. Postma, W. J. Melssen, L. M. C. Buydens, V. Deckert, and R. Zenobi, "Application of principal component analysis to detect outliers and spectral deviations in near-field surface-enhanced Raman spectra," Anal. Chim. Acta 446, 71-83 (2001).
163. M. Hedegaard, C. Krafft, H. J. Ditzel, L. E. Johansen, S. Hassing, and J. r. Popp, "Discriminating Isogenic Cancer Cells and Identifying Altered Unsaturated Fatty Acid Content as Associated with Metastasis Status, Using K-Means Clustering and Partial Least Squares-Discriminant Analysis of Raman Maps," Anal. Chem. 82, 2797-2802 (2010).
164. J. F. C. De Lucia, J. L. Gottfried, C. A. Munson, and A. W. Miziolek, "Multivariate analysis of standoff laser-induced breakdown spectroscopy spectra for classification of explosive-containing residues," Appl. Opt. 47, G112-G121 (2008).
165. V. Vapnik, Statistical Learning Theory (Wiley-Interscience, New York, 1998).
166. C. Cortes, and V. Vapnik, "Support vector networks," Mach. Learn. 20, 273-297 (1995).
167. C. J. C. Burges, "A Tutorial on Support Vector Machines for Pattern Recognition," Data Mining and Knowledge Discovery 2, 121-167 (1998).
168. M. A. Hearst, S. T. Dumais, E. Osman, J. Platt, and B. Scholkopf, "Support vector machines," Intelligent Systems and their Applications, IEEE 13, 18-28 (1998).
169. E. Osuna, R. Freund, and F. Girosit, "Training support vector machines: an application to face detection," in Computer Vision and Pattern Recognition, 1997. Proceedings., 1997 IEEE Computer Society Conference on(1997), pp. 130-136.
170. M. Bonneville, J. Meunier, Y. Bengio, and J.-P. Soucy, "Support vector machines for improving the classification of brain PET images," Medical Imaging 3338, 264-273 (1998).
171. M. Gniadecka, P. A. Philipsen, S. Sigurdsson, S. Wessel, O. F. Nielsen, D. H. Christensen, J. Hercogova, K. Rossen, H. K. Thomsen, R. Gniadecki, L. K. Hansen, and H. C. Wulf, "Melanoma Diagnosis by Raman Spectroscopy and Neural Networks: Structure Alterations in Proteins and Lipids in Intact Cancer Tissue," J Investig Dermatol 122, 443-449 (2004).
172. E. Di Martino, B. Nowak, H. A. Hassan, R. Hausmann, G. Adam, U. Buell, and M. Westhofen, "Diagnosis and staging of head and neck cancer: a comparison of modern imaging modalities (positron emission tomography, computed tomography, color-coded duplex sonography) with panendoscopic

and histopathologic findings," Arch. Otolaryngol. Head Neck Surg. 126, 1457-1461 (2000).
173. S. L. B. Palcic, J. Hung and C. MacAulay, "Detection and localization of early lung cancer by imaging techniques," Chest 99, 742-743 (1991).
174. C. G. D. C. De Veld, M. J. H. Witjes, H. J. C. M. Sterenborg, and J. L. N. Roodenburg, "The status of in vivo autofluorescence spectroscopy and imaging for oral oncology," Oral Oncol. 41, 117-131 (2005).
175. R. Mallia, S. S. Thomas, A. Mathews, R. Kumar, P. Sebastian, J. Madhavan, and N. Subhash, "Oxygenated hemoglobin diffuse reflectance ratio for in vivo detection of oral pre-cancer," J. Biomed. Opt. 13, 041306-041310 (2008).
176. Y. S. Fawzy, M. Petek, M. Tercelj, and H. Zeng, "In vivo assessment and evaluation of lung tissue morphologic and physiological changes from non-contact endoscopic reflectance spectroscopy for improving lung cancer detection," J. Biomed. Opt. 11, 044003-044012 (2006).
177. M. P. L. Bard, A. Amelink, M. Skurichina, V. Noordhoek Hegt, R. P. W. Duin, H. J. C. M. Sterenborg, H. C. Hoogsteden, and J. G. J. V. Aerts, "Optical Spectroscopy for the Classification of Malignant Lesions of the Bronchial Tree*," Chest 129, 995-1001 (2006).
178. H. Zeng, M. Petek, M. T. Zorman, A. McWilliams, B. Palcic, and S. Lam, "Integrated endoscopy system for simultaneous imaging and spectroscopy for early lung cancer detection," Opt Lett 29, 587-589 (2004).
179. C. M. Lee, C. J. Engelbrecht, T. D. Soper, F. Helmchen, and E. J. Seibel, "Scanning fiber endoscopy with highly flexible, 1 mm catheterscopes for wide-field, full-color imaging," Journal of Biophotonics 3, 385-407 (2010).
180. C. Zhu, G. M. Palmer, T. M. Breslin, J. Harter, and N. Ramanujam, "Diagnosis of breast cancer using fluorescence and diffuse reflectance spectroscopy: a Monte-Carlo-model-based approach," J. Biomed. Opt. 13, 034015-034015 (2008).
181. A. E. Cerussi, J. S. Maier, S. Fantini, M. A. Franceschini, W. W. Mantulin, and E. Gratton, "Experimental verification of a theory for the time-resolved fluorescence spectroscopy of thick tissues," Appl Opt 36, 116-124 (1997).
182. J. C. Finlay, and T. H. Foster, "Recovery of hemoglobin oxygen saturation and intrinsic fluorescence with a forward-adjoint model," Appl Opt 44, 1917-1933 (2005).
183. R. S. Bradley, and M. S. Thorniley, "A review of attenuation correction techniques for tissue fluorescence," Journal of the Royal Society, Interface / the Royal Society 3, 1-13 (2006).
184. G. M. Palmer, and N. Ramanujam, "Monte Carlo-based inverse model for calculating tissue optical properties. Part I: Theory and validation on synthetic phantoms," Appl Opt 45, 1062-1071 (2006).
185. J. Wu, M. S. Feld, and R. P. Rava, "Analytical model for extracting intrinsic fluorescence in turbid media," Appl Opt 32, 3585-3595 (1993).
186. Q. Zhang, M. G. Muller, J. Wu, and M. S. Feld, "Turbidity-free fluorescence spectroscopy of biological tissue," Opt Lett 25, 1451-1453 (2000).
187. M. G. Muller, I. Georgakoudi, Q. Zhang, J. Wu, and M. S. Feld, "Intrinsic fluorescence spectroscopy in turbid media: disentangling effects of scattering and absorption," Appl Opt 40, 4633-4646 (2001).
188. P. A. Lachenbruch, and M. R. Mickey, "Estimation of Error Rates in Discriminant Analysis," Technometrics 10, 1-11 (1968).
189. J. L. Devore, "Probability and Statistics for Engineering and the Sciences," in

Thomson/Brooks/Cole(Belmont, Calif., 2009).
190. M. Zargi, L. Smid, I. Fajdiga, B. Bubnic, J. Lenarcic, and P. Oblak, "Detection and localization of early laryngeal cancer with laser-induced fluorescence: preliminary report," Eur. Arch. Otorhinolaryngol. 254 Suppl 1, S113-116 (1997).
191. C. Arens, T. Dreyer, H. Glanz, and K. Malzahn, "Indirect autofluorescence laryngoscopy in the diagnosis of laryngeal cancer and its precursor lesions," Eur. Arch. Otorhinolaryngol. 261, 71-76 (2004).
192. A. Kotaki, and K. Yagi, "Fluorescence Properties of Flavins in Various Solvents," J. Biochem. 68, 509-& (1970).
193. G. Bottiroli, and A. C. Croce, "Autofluorescence spectroscopy of cells and tissues as a tool for biomedical diagnosis," Photochemical & photobiological sciences : Official journal of the European Photochemistry Association and the European Society for Photobiology 3, 189-210 (2004).
194. A. J. Overhiser, and P. Sharma, "Advances in endoscopic imaging: narrow band imaging.," Rev. Gastroenterol. Disord. 8, 186-193 (2008).
195. Y. C. Lin, W. H. Wang, K. F. Lee, W. C. Tsai, and H. H. Weng, "Value of narrow band imaging endoscopy in early mucosal head and neck cancer," Head Neck, n/a-n/a (2012).
196. Z. X. L. W. Z. Y. S. Y. W. W. Wen Y, "Narrow-band imaging: A novel screening tool for early nasopharyngeal carcinoma," Archives of Otolaryngology—Head & Neck Surgery 138, 183-188 (2012).
197. T. Kawai, Y. Takagi, K. Yamamoto, Y. Hayama, M. Fukuzawa, K. Yagi, M. Fukuzawa, M. Kataoka, K. Kawakami, T. Itoi, F. Moriyasu, J. Matsubayashi, and T. Nagao, "Narrow-band imaging on screening of esophageal lesions using an ultrathin transnasal endoscopy," J. Gastroenterol. Hepatol. 27, 34-39 (2012).
198. A. Ignjatovic, J. E. East, V. Subramanian, N. Suzuki, T. Guenther, N. Palmer, P. Bassett, K. Ragunath, and B. P. Saunders, "Narrow Band Imaging for Detection of Dysplasia in Colitis: A Randomized Controlled Trial," Am. J. Gastroenterol. 107, 885-890 (2012).
199. N. Stone, C. Kendall, N. Shepherd, P. Crow, and H. Barr, "Near-infrared Raman spectroscopy for the classification of epithelial pre-cancers and cancers," Journal of Raman Spectroscopy 33, 564-573 (2002).
200. S. K. Teh, W. Zheng, K. Y. Ho, M. Teh, K. G. Yeoh, and Z. Huang, "Diagnostic potential of near-infrared Raman spectroscopy in the stomach: differentiating dysplasia from normal tissue," Br. J. Cancer 98, 457-465 (2008).
201. A. Mahadevan-Jansen, M. F. Mitchell, N. Ramanujam, U. Utzinger, and R. Richards-Kortum, "Development of a Fiber Optic Probe to Measure NIR Raman Spectra of Cervical Tissue In Vivo," Photochem. Photobiol. 68, 427-431 (1998).
202. Z. Huang, A. McWilliams, H. Lui, D. I. McLean, S. Lam, and H. Zeng, "Near-infrared Raman spectroscopy for optical diagnosis of lung cancer," Int. J. Cancer 107, 1047-1052 (2003).
203. M. A. Short, S. Lam, A. McWilliams, J. Zhao, H. Lui, and H. Zeng, "Development and preliminary results of an endoscopic Raman probe for potential in vivo diagnosis of lung cancers," Opt. Lett. 33, 711-713 (2008).
204. Z. Huang, H. Zeng, I. Hamzavi, D. I. McLean, and H. Lui, "Rapid near-infrared Raman spectroscopy system for real-time in vivo skin measurements," Opt. Lett. 26, 1782-1784 (2001).

205. J. T. Motz, M. Hunter, L. H. Galindo, J. A. Gardecki, J. R. Kramer, R. R. Dasari, and M. S. Feld, "Optical Fiber Probe for Biomedical Raman Spectroscopy," Appl. Opt. 43, 542-554 (2004).
206. M. S. Bergholt, Zheng, W., Lin, K., Ho, K.Y., Teh, M., Yeoh, K.G., So, J.B.Y, Huang, Z, "In Vivo Diagnosis of Esophageal Cancer Using Image-Guided Raman Endoscopy and Biomolecular Modeling," Technol Cancer Res Treat. 10, 103-112 (2011).
207. "American National Standard for the Safe Use of Lasers," ANSI Standard 2136, 1-1986 American National Standards Institute, Washington, D.C., (1986).
208. N. Stone, C. Kendall, J. Smith, P. Crow, and H. Barr, "Raman spectroscopy for identification of epithelial cancers," Faraday Discuss. 126, 141-157; discussion 169-183 (2004).
209. J. Mo, W. Zheng, J. J. H. Low, J. Ng, A. Ilancheran, and Z. Huang, "High Wavenumber Raman Spectroscopy for in Vivo Detection of Cervical Dysplasia," Anal. Chem. 81, 8908-8915 (2009).
210. A. Mahadevan-Jansen, and R. R. Richards-Kortum, "Raman spectroscopy for the detection of cancers and precancers," J. Biomed. Opt. 1, 31-70 (1996).
211. D. P. Lau, Z. Huang, H. Lui, C. S. Man, K. Berean, M. D. Morrison, and H. Zeng, "Raman spectroscopy for optical diagnosis in normal and cancerous tissue of the nasopharynx-preliminary findings," Lasers Surg. Med. 32, 210-214 (2003).
212. N. Stone, P. Stavroulaki, C. Kendall, M. Birchall, and H. Barr, "Raman Spectroscopy for Early Detection of Laryngeal Malignancy: Preliminary Results," The Laryngoscope 110, 1756-1763 (2000).
213. Z. Huang, M. S. Bergholt, W. Zheng, K. Lin, K. Y. Ho, M. Teh, and K. G. Yeoh, "In vivo early diagnosis of gastric dysplasia using narrow-band image-guided Raman endoscopy," J. Biomed. Opt. 15 (2010).
214. K. W. Short, S. Carpenter, J. P. Freyer, and J. R. Mourant, "Raman Spectroscopy Detects Biochemical Changes Due to Proliferation in Mammalian Cell Cultures," Biophys. J. 88, 4274-4288 (2005).
215. K. Lin, D. L. P. Cheng, and Z. Huang, "Optical diagnosis of laryngeal cancer using high wavenumber Raman spectroscopy," Biosens. Bioelectron. 35, 213-217 (2012).
216. E. A. Chu, and Y. J. Kim, "Laryngeal Cancer: Diagnosis and Preoperative Work-up," Otolaryngol. Clin. North Am. 41, 673-695 (2008).
217. W.-f. Cao, L.-y. Zhang, M.-b. Liu, P.-z. Tang, Z.-h. Liu, and B.-c. Sun, "Prognostic significance of stomatin-like protein 2 overexpression in laryngeal squamous cell carcinoma: clinical, histologic, and immunohistochemistry analyses with tissue microarray," Hum. Pathol. 38, 747-752 (2007).
218. L.-A. Lee, A.-J. Cheng, T.-J. Fang, C.-G. Huang, C.-T. Liao, J. T.-C. Chang, and H.-Y. Li, "High Incidence of Malignant Transformation of Laryngeal Papilloma in Taiwan," The Laryngoscope 118, 50-55 (2008).
219. M. Beser, E. Gultekin, M. Yener, M. Zeybek, B. Öner, and V. Topçu, "Detection of laryngeal tumors and tumoral extension by multislice computed tomography-virtual laryngoscopy (MSCT-VL)," Eur. Arch. Otorhinolaryngol. 266, 1953-1958 (2009).
220. A. Nijssen, T. C. Bakker Schut, F. Heule, P. J. Caspers, D. P. Hayes, M. H. A. Neumann, and G. J. Puppels, "Discriminating Basal Cell Carcinoma from its Surrounding Tissue by Raman Spectroscopy," 119, 64-69 (2002).

221. L. M. Almond, J. Hutchings, N. Shepherd, H. Barr, N. Stone, and C. Kendall, "Raman spectroscopy: a potential tool for early objective diagnosis of neoplasia in the oesophagus," Journal of Biophotonics 4, 685-695 (2011).
222. M. S. Bergholt, W. Zheng, K. Lin, K. Y. Ho, M. Teh, K. G. Yeoh, J. B. Yan So, and Z. Huang, "In vivo diagnosis of gastric cancer using Raman endoscopy and ant colony optimization techniques," Int. J. Cancer 128, 2673-2680 (2011).
223. R. O. P. Draga, M. C. M. Grimbergen, P. L. M. Vijverberg, C. F. P. v. Swol, T. G. N. Jonges, J. A. Kummer, and J. L. H. Ruud Bosch, "In Vivo Bladder Cancer Diagnosis by High-Volume Raman Spectroscopy," Anal. Chem. 82, 5993-5999 (2010).
224. A. S. Haka, Z. Volynskaya, J. A. Gardecki, J. Nazemi, J. Lyons, D. Hicks, M. Fitzmaurice, R. R. Dasari, J. P. Crowe, and M. S. Feld, "In vivo Margin Assessment during Partial Mastectomy Breast Surgery Using Raman Spectroscopy," Cancer Res. 66, 3317-3322 (2006).
225. W. Hale, K. Rachel, S. Cory, S. Brian, R. Raja, P. Janet, P. Abhilash, A. Greg, and D. K. Michael, "Diagnosis of Wilms' tumor using near-infrared Raman spectroscopy," J. Pediatr. Surg. 44, 1152-1158 (2009).
226. E. M. Kanter, E. Vargis, S. Majumder, M. D. Keller, E. Woeste, G. G. Rao, and A. Mahadevan-Jansen, "Application of Raman spectroscopy for cervical dysplasia diagnosis," Journal of Biophotonics 2, 81-90 (2009).
227. N. D. Magee, J. S. Villaumie, E. T. Marple, M. Ennis, J. S. Elborn, and J. J. McGarvey, "Ex Vivo Diagnosis of Lung Cancer Using a Raman Miniprobe," The Journal of Physical Chemistry B 113, 8137-8141 (2009).
228. S. K. Teh, W. Zheng, K. Y. Ho, M. Teh, K. G. Yeoh, and Z. Huang, "Near-infrared Raman spectroscopy for gastric precancer diagnosis," Journal of Raman Spectroscopy 40, 908-914 (2009).
229. E. Widjaja, W. Zheng, and Z. Huang, "Classification of colonic tissues using near-infrared Raman spectroscopy and support vector machines," Int. J. Oncol. 32, 653-662 (2008).
230. L.-M. Wong Kee Song, "Diagnostic potential of Raman spectroscopy in Barrett?s esophagus.," SPIE, 140-146 (2005).
231. M. G. Shim, L.-M. Wong Kee Song, N. E. Marcon, and B. C. Wilson, "In vivo Near-infrared Raman Spectroscopy: Demonstration of Feasibility During Clinical Gastrointestinal Endoscopy ¶," Photochem. Photobiol. 72, 146-150 (2000).
232. S. Koljenovic, T. C. B. Schut, R. Wolthuis, B. de Jong, L. Santos, P. J. Caspers, J. M. Kros, and G. J. Puppels, "Tissue characterization using high wave number Raman spectroscopy," J. Biomed. Opt. 10, 031116-031111 (2005).
233. A. Nijssen, K. Maquelin, L. F. Santos, P. J. Caspers, T. C. B. Schut, J. C. den Hollander, M. H. A. Neumann, and G. J. Puppels, "Discriminating basal cell carcinoma from perilesional skin using high wave-number Raman spectroscopy," J. Biomed. Opt. 12, 034004-034007 (2007).
234. A. Savitzky, and M. J. E. Golay, "Smoothing and Differentiation of Data by Simplified Least Squares Procedures," Anal. Chem. 36, 1627-1639 (1964).
235. W. R. Dillon, and M. Goldstein, Multivariate analysis : methods and applications (: Wiley, New York, 1984).
236. N. S. Eikje, Y. Ozaki, K. Aizawa, and S. Arase, "Fiber optic near-infrared Raman spectroscopy for clinical non-invasive determination of water content in diseased skin and assessment of cutaneous edema," J. Biomed. Opt. 10, 014013-014013 (2005).

237. L. F. Santos, R. Wolthuis, S. Koljenović, R. M. Almeida, and G. J. Puppels, "Fiber-Optic Probes for in Vivo Raman Spectroscopy in the High-Wavenumber Region," Anal. Chem. 77, 6747-6752 (2005).
238. C. E. Mountford, R. L. Somorjai, P. Malycha, L. Gluch, C. Lean, P. Russell, B. Barraclough, D. Gillett, U. Himmelreich, B. Dolenko, A. E. Nikulin, and I. C. P. Smith, "Diagnosis and prognosis of breast cancer by magnetic resonance spectroscopy of fine-needle aspirates analysed using a statistical classification strategy," Br. J. Surg. 88, 1234-1240 (2001).
239. M. G. Shim, B. C. Wilson, E. Marple, and M. Wach, "Study of Fiber-Optic Probes for in Vivo Medical Raman Spectroscopy," Appl. Spectrosc. 53, 619-627 (1999).
240. F. Abdat, M. Amouroux, Y. Guermeur, and W. Blondel, "Hybrid feature selection and SVM-based classification for mouse skin precancerous stages diagnosis from bimodal spectroscopy," Opt Express 20, 228-244 (2012).
241. W. Zhai, Y. H. Xiang, Y. M. Dai, J. J. Zhang, and Z. Y. Zhang, "[Early stage diagnosis of endometrial cancer based on near infrared spectroscopy and support vector machine]," Guang pu xue yu guang pu fen xi = Guang pu 31, 932-936 (2011).
242. R. Lopes, A. Ayache, N. Makni, P. Puech, A. Villers, S. Mordon, and N. Betrouni, "Prostate cancer characterization on MR images using fractal features," Med. Phys. 38, 83-95 (2011).
243. L. Wei, Y. Yang, R. M. Nishikawa, and Y. Jiang, "A study on several machine-learning methods for classification of malignant and benign clustered microcalcifications," IEEE Trans. Med. Imaging 24, 371-380 (2005).
244. G. S. Nayak, S. Kamath, K. M. Pai, A. Sarkar, S. Ray, J. Kurien, L. D'Almeida, B. R. Krishnanand, C. Santhosh, V. B. Kartha, and K. K. Mahato, "Principal component analysis and artificial neural network analysis of oral tissue fluorescence spectra: Classification of normal premalignant and malignant pathological conditions," Biopolymers 82, 152-166 (2006).
245. L. C. Kwek, S. Fu, T. C. Chia, C. H. Diong, C. L. Tang, and S. M. Krishnan, "High-sensitivity and specificity of laser-induced autofluorescence spectra for detection of colorectal cancer with an artificial neural network," Appl. Opt. 44, 4004-4008 (2005).
246. S. Sigurdsson, P. A. Philipsen, L. K. Hansen, J. Larsen, M. Gniadecka, and H. C. Wulf, "Detection of skin cancer by classification of Raman spectra," Biomedical Engineering, IEEE Transactions on 51, 1784-1793 (2004).
247. D. C. G. de Veld, M. Skurichina, M. J. H. Witjes, R. P. W. Duin, H. J. C. M. Sterenborg, and J. L. N. Roodenburg, "Clinical study for classification of benign, dysplastic, and malignant oral lesions using autofluorescence spectroscopy," J. Biomed. Opt. 9, 940-950 (2004).
248. D. J. Evers, R. Nachabé, H. M. Klomp, J. W. van Sandick, M. W. Wouters, G. W. Lucassen, B. H. W. Hendriks, J. Wesseling, and J. M. Theo, "Diffuse Reflectance Spectroscopy: A New Guidance Tool for Improvement of Biopsy Procedures in Lung Malignancies," Clinical Lung Cancer (2012).
249. H. Gu, Z. Pan, B. Xi, V. Asiago, B. Musselman, and D. Raftery, "Principal component directed partial least squares analysis for combining nuclear magnetic resonance and mass spectrometry data in metabolomics: Application to the detection of breast cancer," Anal. Chim. Acta 686, 57-63 (2011).
250. H. Lui, J. Zhao, D. McLean, and H. Zeng, "Real-time Raman Spectroscopy for In Vivo Skin Cancer Diagnosis," Cancer Res. 72, 2491-2500 (2012).

251. S. Duraipandian, W. Zheng, J. Ng, J. J. H. Low, A. Ilancheran, and Z. Huang, "In vivo diagnosis of cervical precancer using Raman spectroscopy and genetic algorithm techniques," Analyst 136, 4328-4336 (2011).
252. M. S. Bergholt, W. Zheng, K. Lin, K. Y. Ho, M. Teh, K. G. Yeoh, J. B. Yan So, and Z. Huang, "Raman endoscopy for in vivo differentiation between benign and malignant ulcers in the stomach," Analyst 135, 3162-3168 (2010).
253. X. Shao, W. Zheng, and Z. Huang, "In vivo diagnosis of colonic precancer and cancer using near-infrared autofluorescence spectroscopy and biochemical modeling," J. Biomed. Opt. 16, 067005-067008 (2011).